

**Computational investigation of function of membrane proteins:  
Amt/Rh Ammonium transporters and SecY translocon**

**Inauguraldissertation**

**zur**

**Erlangung der Würde eines Doktors der Philosophie**

**vorgelegt der**

**Philosophisch-Naturwissenschaftlichen Fakultät**

**der Universität Basel**

**von**

**Sefer Baday**

**aus der Türkei**

**Basel, 2014**

Genehmigt von der Philosophisch Naturwissenschaftlichen Fakultät  
auf Antrag von

Faculty representative and  
Dissertation supervisor: Prof. Simon Bernèche

Thesis Co-examiner: Prof. Torsten Schwede

Basel, 26 March 2013

The Dean of the Faculty  
Prof. Dr. Jörg Schibler

## ABSTRACT

In this thesis, we studied the function of the Amt/Rh family of proteins and of the SecY/Sec61 translocons using computational methods. The Amt/Rh proteins mediate transport of ammonium across the lipid bilayer. SecY and Sec61 translocons facilitate the insertion of membrane proteins or translocation of secreted proteins in prokaryotes and eukaryotes, respectively. We investigated on the molecular details of ammonium transport in E.Coli AmtB and human RhCG proteins, and the effect of the hydrophobicity of the SecY translocon pore in membrane protein insertion.

Functional studies have revealed that Amt proteins transport the charged form of ammonium ( $\text{NH}_4^+$ ) while Rh proteins transport neutral ammonia ( $\text{NH}_3$ ). However, permeation mechanisms at a molecular level have not been understood clearly. Here, we present molecular details of ammonium transport in AmtB and RhCG proteins. Our calculations show that ammonium ion binds and deprotonates at the hydrophobic pore of AmtB. Then, ammonia diffuses down the hydrophobic pore while the excess proton is transported with the help of a highly conserved histidine dyad (H168 and H318). Ammonia gets re-protonated when it reaches the bottom of the pore and leaves the channel as ammonium. To recruit a new ammonium substrate the protonation states of the histidine dyad has to be reset. This is achieved through water molecules forming a single-file chain in the pore. Thus, hydration of the pore plays an important role in the transport mechanism in AmtB protein. Our simulations of RhCG protein have revealed that the pore of RhCG protein is not hydrated. Lack of hydration in the pore suggests that the excess proton cannot be transported across the hydrophobic pore as it is proposed for AmtB. We show that ammonium binds and deprotonates at a histidine residue (H185) lining the hydrophobic pore of RhCG. After deprotonation, ammonia diffuses down the pore. Then, the excess proton is circulated back to the extracellular site through a network of hydrogen bonds connecting H185 to D177. In conclusion, our calculations suggest that RhCG protein transports neutral ammonia while AmtB transports charged ammonium.

Experimental findings showed that mutation of the pore-ring residues of Sec61 translocon changed the hydrophobicity threshold for membrane integration. Our

free energy calculations suggested that mutation of the pore-ring residues influences the stability of peptides in the pore, thus affecting the probability of membrane integration. In addition, insertion experiments of oligo alanine peptides, which contain a cluster of three leucines at various positions, revealed an asymmetry in the membrane integration profile. In particular, a significant drop in membrane integration was observed when the three-leucine cluster aligns with the pore-ring residues. We simulated the wild-type SecY and its pore-ring mutants with the oligo-alanine peptides initially placed into the pores. Analysis of these simulations suggested that hydration of the leucine side-chains drops dramatically when the three-leucine cluster is aligned with the pore-ring residues. The reduced hydration of the leucine residues stabilizes the peptide in the translocon pore and favors its translocation.

## ACKNOWLEDGEMENTS

Firstly, I would like to thank my PhD supervisor Prof. Dr. Simon Bernèche for his great guidance and support throughout my graduate study. I am proud of being his student. I thank also Prof. Dr. Torsten Schwede and Prof. Dr. Martin Spiess for their participation in my PhD advisory committee.

I would like to thank all the current and former members of the Bernèche group who made the time enjoyable during my PhD study; Dr. Céline Boiteux, Wojciech Pawel Wojtas-Niziurski, Gregory Starek, Yanyan Xu, Olivier Bignucolo, Florian Heer, Dr. Chung-Wen Liang and Ximena Contreras.

I would like to also thank all my friends who provided their support despite the long distances; Cengiz Ulubas, Osman Yogurtcu, Nurcan Tuncbag, Ozge Engin, Gozde Kar, Besray Unal, Fatih Toy, Emre Guney, Aslıhan Aslan, Bora Karasulu, Bahar Ondul and Yasemin Demir.

Finally, I am grateful to my parents Salatın and Latif; my brother Murat and my sister-in-law Rachel; my sister Meryem and my little brother Fatih for their love, affection and support throughout my life.

## TABLE OF CONTENTS

<b>ABSTRACT .....</b>	<b>iii</b>
<b>ACKNOWLEDGEMENTS .....</b>	<b>v</b>
<b>TABLE OF CONTENTS.....</b>	<b>vi</b>
<b>Chapter 1.....</b>	<b>1</b>
<b>Ammonium transport in Amt/Rh family proteins.....</b>	<b>1</b>
1. 1 Introduction to Ammonium Transport in Amt Family Proteins.....	2
1. 2 Important Structural Features of AmtB .....	3
1. 3 Functional Studies on the Ammonium Transport in Amt Proteins.....	5
1. 4 Permeation Mechanisms in AmtB.....	7
1. 5 Introduction to Ammonium transport in Rh Family Proteins.....	10
1. 6 Important Structural Features of RhCG.....	12
1. 7 Functional Studies on the Ammonium Transport in Rh Proteins.....	14
1. 8 Outline for Chapters 2, 3 and 4.....	16
1. 9 References.....	17
<b>Chapter 2.....</b>	<b>23</b>
<b>Ammonium transporters achieve charge transfer by fragmenting their substrate.....</b>	<b>23</b>
2. 1 Abstract .....	24
2. 1 Introduction.....	25
2. 2 Results and Discussion .....	27
2.2.1 Recruitment of NH <sub>4</sub> <sup>+</sup> in site S1.....	27
2.2.2 Affinity of NH <sub>4</sub> <sup>+</sup> in site S2 .....	29
2.2.3 Mechanism of NH <sub>4</sub> <sup>+</sup> deprotonation in S2 .....	33
2.2.4 NH <sub>3</sub> diffusion along the protonated His168-His318 dyad .....	36
2.2.5 Re-protonation of NH <sub>3</sub> at site S4 .....	37
2.2.6 Coupling between NH <sub>3</sub> and H <sup>+</sup> transport.....	39
2.2.7 Reset of His168 and His318 protonation states .....	40
2. 3 Conclusion .....	43
2. 4 Experimental Details .....	46
2.4.1 Simulation System Preparation .....	46
2.4.2 Molecular Dynamic (MD) Simulations.....	46
2.4.3 Binding Free Energy Calculations.....	46
2.4.4 Quantum Mechanics/Molecular Mechanics (QM/MM) Simulations .....	47
2.4.5 Constrained QM/MM Simulations .....	47

2.4.6 Adaptive biasing force (ABF) simulations.....	47
2. 5 References.....	49
2. 6 Appendix.....	57
2.6.1 Parameterization of polarizable force field.....	57
2.6.2 Potential energy surfaces.....	59
2.6.3 Optimized force field.....	60
2.6.4 AmtB simulation system.....	60
2.6.5 Free energy calculations.....	61
2.6.6 Polarizable mechanics/molecular mechanics (PM/MM) simulations setup .....	62
2.6.7 QM/MM simulations setup.....	63
2.6.8 Tables.....	69
2.6.9 References.....	72
<b>Chapter 3.....</b>	<b>75</b>
<b>Different hydration patterns in the pores of AmtB and RhCG could determine their transport mechanisms.....</b>	<b>75</b>
3. 1 Abstract.....	76
3. 2 Introduction.....	77
3. 3 Results.....	79
3.3.1 Stability of ammonia molecules in the pore of AmtB.....	79
3.3.2 Stability of water molecules in the pore of AmtB.....	81
3.3.3 Relative stabilities of water and ammonia in the pore of AmtB.....	84
3.3.4 Stability of ammonia and water molecules in the pore of RhCG.....	87
3.3.5 Simulation of AmtB and RhCG mutants.....	90
3. 4 Discussion.....	93
3. 5 Methods.....	95
3.5.1 Simulation systems.....	95
3.5.2 Free-Energy Perturbation Calculations.....	96
3. 6 References.....	98
3. 7 Appendix.....	102
3.7.1 Figures.....	102
<b>Chapter 4.....</b>	<b>109</b>
<b>The mechanism of ammonium transport in RhCG protein.....</b>	<b>109</b>
4. 1 Abstract.....	110
4. 2 Introduction.....	111
4. 3 Results and Discussion.....	113
4.3.1 Recruitment of ammonium and proton transfer to His185.....	113

4.3.2 Dynamics of ammonia after deprotonation of ammonium .....	116
4.3.3 H-bond network linking His185 to Asp177 through water molecules and Ser181 .....	119
4.3.4 Proton transfer from His185 to Asp177 .....	120
4.3.5 Release of the proton from D177 .....	123
4. 4 Conclusion .....	124
4. 5 Methods .....	125
4.5.1 Simulation systems .....	125
4.5.2 Classical free energy calculations .....	126
4.5.3 Quantum mechanics/molecular mechanics simulations.....	127
4. 6 References .....	128
4. 7 Appendix .....	132
4.7.1 Tables .....	132
4.7.2 Figures .....	133
<b>Chapter 5.....</b>	<b>136</b>
<b>The effect of hydrophobicity of the SecY Translocon pore in membrane protein insertion.....</b>	<b>136</b>
5. 1 Introduction.....	137
5.1.1 An Overview of Membrane protein insertion.....	137
5.1.2 Structure of the translocon.....	139
5.1.3 Hydrophobicity scales for membrane partitioning of amino acids.....	141
5.1.4 Are translocons just catalyzers in membrane protein insertion or not? ..	143
5.1.5 Outline for the sections 5.2 and 5.3.....	144
5. 2 Investigating the stability of membrane-inserting and non-inserting peptides inside the pore of SecY and its pore-ring mutants.....	145
5. 3 Asymmetry in membrane insertion caused by Sec translocon.....	149
5. 4 Methods.....	154
5. 5 Conclusion .....	156
5. 6 References .....	159
<b>Curriculum Vitae .....</b>	<b>165</b>



**Chapter 1**

**AMMONIUM TRANSPORT IN AMT/RH FAMILY PROTEINS**

## **1. 1 Introduction to Ammonium Transport in Amt Family Proteins**

Ammonium is used as a nitrogen source in the three kingdoms of life (bacteria, yeast and plants) and transported by Amt/Mep family proteins from extracellular site to cytosol at low ammonium concentrations. However, ammonium is a toxic substrate in mammalian cells where Rh family proteins, orthologs of Amt proteins, facilitate ammonium transport in the excretion process of ammonium (1-3).

In this chapter, unless otherwise specified, the word “ammonium” refers to both ammonium and ammonia. In solution, ammonium exists in two molecular forms: neutral  $\text{NH}_3$  and charged  $\text{NH}_4^+$ . The fractions of these forms are determined by the pH of the solution. At physiological pH the majority of ammonium is in  $\text{NH}_4^+$  form (approximately 99%). Neutral  $\text{NH}_3$  can diffuse through lipid bilayer, whereas charged  $\text{NH}_4^+$  cannot. However when the concentration of ammonium is low in the medium, it becomes a limiting factor for the growth. Proteins from Amt family are expressed to enhance ammonium uptake since the diffusion rate of  $\text{NH}_3$  through the membrane doesn't suffice. Javelle et al. reported that E.Coli Ammonium transporter (EcAmtB) are expressed when ammonium concentrations is less than 50  $\mu\text{M}$  (4). Plant Amt's also operate under micro molar concentrations (ranging from 10-100  $\mu\text{M}$ ) (5).

## 1. 2 Important Structural Features of AmtB

Structures of two proteins from Amt family have been revealed: E.Coli AmtB and *A. fulgidus* Amt-1. Here, we will briefly explain important structural features of E.Coli AmtB for the transport of ammonium. Khademi et al. and Zheng et al. obtained the crystal structure of EcAmtB with a resolution of 1.35 Å and 1.8 Å respectively (6-8). AmtB crystallizes as a homotrimer and each monomer is composed of 11 transmembrane helices. Four putative binding sites for ammonium substrate were observed in both X-ray structures (Figure 1.1.c). Khademi et al. concluded that the sites S2, S3 and S4 are binding sites for ammonia. However the other crystal structure, which shows electron density peaks at similar locations, was obtained in the absence of ammonium salt. This suggests that these peaks could belong to water molecules too. In chapter 2 we addressed the question of what species (water or ammonia) most likely occupies the pore in the resting state of AmtB.

The AmtB structure can be divided into four regions: extracellular vestibule, two phenylalanines forming so-called a gate (Phe gate), hydrophobic core with twin-histidines and cytosolic vestibule. In the extracellular vestibule a putative binding site, which is formed by a tryptophan (W148), serine (S219) and two phenylalanines (F103 and F107), for ammonium just above the Phe gate is observed in the crystal structures. A mutagenesis study for this binding site shows the loss of binding affinity when the residues around this site are mutated (9). Recently, our collaborators from Lamoureux group calculated the binding affinity of -14.1 kcal/mol for ammonium at this site using state-of-art hybrid polarizable/molecular mechanics simulations (10). The high binding affinity of ammonium is highly crucial for the recruitment of ammonium and optimal function of AmtB at very low concentrations.

Just below this binding site the residues F107 and F215 occlude the pore and form a gate like structure. This Phe gate is highly conserved among Amt/Rh family proteins. The high conservation of this gate suggests a significant role in the functions of these proteins, however no clear evidence has been obtained to date. Molecular dynamics simulations suggest that small molecules can't pass through this gate (11-13). Functional experiments of the Phe gate mutants show that the alanine mutant of bottom phenylalanine, F215A, abolishes the activity totally whereas F107A mutant has slightly better activity than the wild-type.

However the double mutant F107A/F215A yields inactive AmtB (9). These results suggest that F215 has an important function in the deprotonation and the transfer of ammonium to the site S2 in the pore.

The hydrophobic pore region has two highly conserved histidine residues (H168 and H318). In a functional mutagenesis study, Javelle et al. showed that this histidine dyad is absolutely required for ammonium transport (14). The high conservation of these histidines and the mutagenesis study support the hypothesis that this histidine dyad might play an important role in deprotonation of ammonium. In addition, a tryptophan residue close to S2 (W212) is also highly conserved in Amt/Rh proteins. Functional study of this residue shows that W212A mutant is inactive whereas W212F mutant remains active (9). The mutagenesis study on W212 suggests that having an aromatic ring at the position of W212 contributes to stabilization of ammonium ion at S2 via cation-pi interactions.

Two crystal forms obtained by Zheng et al. showed structural variations at the cytoplasmic vestibule. The most prominent change is the side chain conformation of V314. In one crystal form, the side chain of V314 points towards the pore and makes the pore narrower. The reason for this structural variation is not known. But, it is suspected that binding of the regulatory GlnK protein might cause the conformational change at the cytoplasmic vestibule (6). In addition, the role of the cytoplasmic vestibule in ammonium transport remains unclear.

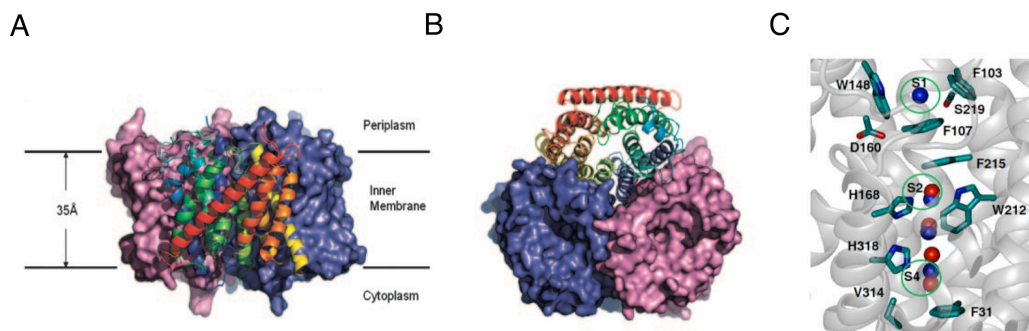


**Figure 1.1** Structure of EcAmtB. a) front view b) top view c) important residues and putative substrate binding sites in the EcAmtB pore, blue and red spheres shows the location of density peaks for the substrates in the X-ray structures from Khademi et al. (PDB Id: 1U7G) and Zheng et al. (PDB Id: 1XQF). (Panels a and b were taken from (6), and panel c was taken from (10))

### 1.3 Functional Studies on the Ammonium Transport in Amt Proteins

The methods for investigating protein mediated ammonium conduction are mostly the measurements of methylammonium (MA) uptake, ammonium induced internal pH changes and ammonium induced currents in voltage-clamped cells. All the techniques have some limitations. Firstly, the disparate pK<sub>a</sub>s of MA and ammonium (10.65 versus 9.25) could give different affinities and transport rates. Secondly, the accuracy of measuring internal pH changes heavily depends on the sensitivity and rapidity of the technique. Thirdly, in the ammonium induced current measurements it is difficult to discriminate the current resulted from the protein of interest, from the current due to endogenous channels and transporters in the cell in which measurements are taken (15). Beside the measurement method, the experimental setups and protocols could also affect the results of functional studies. Typical constructs for functional studies are in vitro assays, in vitro assays with cell-derived vesicles and cellular essays. In vitro assays are formed by purification and reconstitution of desired proteins into liposomes. In this kind of constructs the orientation of proteins could affect the results obtained. The orientation problem is solved by in-vitro assays with cell-derived vesicles due to the fact that in this protocol cellular machinery inserts the protein into the membrane. Despite the aforementioned problem arising from endogenous proteins in cellular essays, a large number of functional studies for ammonium transport in Amt and Rh proteins used cellular assays, particularly oocytes (1).

Functional studies on the ammonium transport mechanisms in Amt proteins suggested both neutral and charged ammonium transport. Earlier studies from the lab of Sidney Kustu suggested that AmtB facilitates neutral and bidirectional NH<sub>3</sub> transport based on the growth experiments of *E.coli* and *S. typhimurium* cells (16,17). However, a recent work of Kustu and coworkers concluded the opposite mechanism: charged ammonium transport (18). Khademi et al. also claimed neutral ammonium transport based on internal pH change measurements in AmtB proteoliposomes. But, Javelle et al. couldn't reproduce the results reported by Khademi et al. (1).

Other functional studies suggested the charged ammonium transport. Ludewig et al. and Mayer et al. expressed Amt proteins from *Lycopersicon esculentum* and *Arabidopsis thaliana* plants in oocytes and performed electrophysiological experiments. Results from these experiments show that these plant Amts have

high affinity for ammonium and charged ammonium is transported either as uniport of  $\text{NH}_4^+$  or cotransport of  $\text{NH}_3$  and  $\text{H}^+$  (1,19-24).

#### 1. 4 Permeation Mechanisms in AmtB

The elucidation of the structure of EcAmtB has helped significantly to understand the permeation mechanism of ammonium by the simple description of the pore and derived insights. The X-ray structure also gave the opportunity to perform molecular dynamics simulations (MD) and mutagenesis experiments for elucidating permeation mechanism at molecular level.

It is widely accepted that  $\text{NH}_4^+$  is recruited and binds to the site S1. MD simulations have shown that  $\text{NH}_4^+$  and other ions can't pass through the hydrophobic pore due to a high-energy barrier (12,13,25-27). Because of the high-energy barrier for ammonium ion, both electrogenic and electroneutral transport mechanisms suggest the deprotonation of  $\text{NH}_4^+$  at some point along the transporter.

Electroneutral transport mechanisms propose that deprotonated ammonia diffuses down the pore and the proton is transported back to the periplasm. Most of the electroneutral mechanisms suggest that highly conserved aspartic acid, D160 (near S1), is involved in the deprotonation of ammonium at site S1 through a network of H-bonds formed by periplasmic water molecules (12,26,28,29). The idea that D160 can play a role in the deprotonation of ammonium emerged from the mutagenesis experiments in which D160A mutant abolished ammonium conduction whereas D160E mutant retained the activity of the wild type significantly (71%) (4,30). It has been also suggested that ammonium can be deprotonated between S1 and S2 (13,27). Bostick et al. proposed that ammonium is coordinated by the backbone carbonyl of A162, a water molecule coming from the periplasm and F215. According to their simulations, ammonium can be easily deprotonated to the water molecule due to the fact that the pKa of ammonium is lowered at this position (27). Nygaard et al. suggested that ammonium transfers its proton to the carbonyl of Ala162. Then the excess proton is exchanged with amino group of G163 via imidic acid mechanism. Finally, the proton is transported back to the periplasmic site through D160, which is interacting with the amino group of G163 (13).

Electroneutral transport mechanisms, however, don't explain why  $\text{NH}_3$  should diffuse down the pore from S1 or between S1-S2 instead of diffusing back to the periplasm. Moreover, these mechanisms can't illuminate the need for the conserved histidine residues, which were shown to be required for the activity of AmtB. Javelle et al. showed that alanine mutant of H168 can't conduct

ammonium whereas the glutamate mutant remained active (14). This finding supported the idea that these twin-histidines are involved in the deprotonation of  $\text{NH}_4^+$  at S2 (31,32). The functional studies on the highly conserved residues around S2 (H168, H318, F215, W212) support the idea of an electrogenic transport mechanisms, particularly the cotransport of  $\text{NH}_3$  and  $\text{H}^+$  since  $\text{NH}_4^+$  cannot diffuse down the hydrophobic pore.

Most of the computational studies presumed electroneutral transport and focused on investigating detailed mechanisms for proton transfer around S1. However, together with our collaborators from the Lamoureux lab, we recently presented a  $\text{NH}_3/\text{H}^+$  cotransport mechanism with molecular details using quantum and molecular mechanical simulations (10). We showed that  $\text{NH}_4^+$  is coordinated by F215, W212 and H318 and has high binding affinity (-13 kcal/mol) at S2. In our simulations we observed a stable water chain in the hydrophobic pore region, which was also reported previously (33). This water chain also contributes to the stabilization of  $\text{NH}_4^+$  at S2. Using hybrid quantum mechanics/molecular mechanics (QM/MM) simulations we illustrated that  $\text{NH}_4^+$  can easily deprotonate to N $\epsilon$  atom of H168 but not to water molecules in the pore. After deprotonation,  $\text{NH}_3$  diffuses down the pore with an almost barrierless free energy profile. We showed that  $\text{NH}_3$  gets its proton back from N $\epsilon$  atom of H318. Protonation of H168 makes the proton transfer from H318 to  $\text{NH}_3$  feasible, because the excess proton on H168 is shared between H168-N $\delta$  and H318-N $\delta$  atoms. Upon the protonation of  $\text{NH}_3$ , the excess proton stays on the N $\delta$  atom of H318. This process changes the protonation states of the histidine dyad. To recruit a new ammonium substrate the protonation states of the histidine dyad should be reset. The potentials of mean force (PMF) obtained by QM/MM simulations for the proton transfer from N $\epsilon$  of H168 to N $\epsilon$  of H318 through the water chain has a free energy barrier of 17 kcal/mol. The reset of the protonation dyad thus seems to be the rate-limiting step of ammonium transport. Consequently, we showed that AmtB binds and splits  $\text{NH}_4^+$  and transports subsequently  $\text{NH}_3$  and  $\text{H}^+$  through the pore. It was also shown that water molecules in the pore of AmtB play an important role in ammonium transport (10).

An important argument against electrogenic ammonium transport is that ammonium cannot pass through the hydrophobic Phe gate and reach S2. The free energy calculations have been performed till now showed that this transition has a



very high-energy barrier, which makes it impossible for ammonium to cross over (12,34). However, all the simulations were done with classical molecular dynamics methods, which underestimate the cation- $\pi$  interactions (35). Our preliminary results from three-dimensional PMF calculations using the state-of-art hybrid polarizable mechanics/molecular mechanics (PM/MM) models, which accurately estimate the cation- $\pi$  interaction, show that the barrier for ammonium crossing the Phe gate is around 6 kcal/mol. This result suggests that the translocation of ammonium from S1 to S2 is feasible.

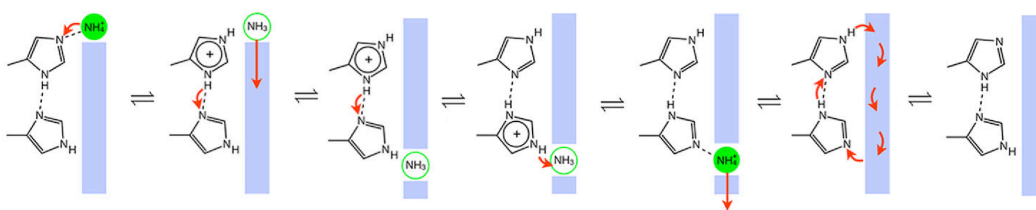


**Figure 1.2** Schematic illustration of the  $\text{NH}_3/\text{H}^+$  cotransport mechanism. Adapted from Wang et al (10).

### **1.5 Introduction to Ammonium transport in Rh Family Proteins**

In mammals ammonia is produced mostly in the brain, kidney and gut. Acid-base homeostasis is highly vital for organs to function normally. The liver and kidney have crucial roles in acid-base homeostasis regarding ammonia. Liver converts ammonia to urea and glutamine, and kidney excretes ammonia to urinary space. An increase of ammonium concentration in blood results in the increase in acid load in brain, which might cause dysfunction of brain such as hepatic encephalopathy. Hepatic encephalopathy causes cognitive, psychiatric and motor disorders, and results from over accumulation of ammonia in blood-brain barrier due to liver failure. Dysfunction of kidney in acid excretion leads to metabolic acidosis, which contributes to many physiological disorders such as osteopenia, osteoporosis, peripheral insulin resistance and lower leptin secretion. (15,36-40).

Ammoniogenesis and transport of ammonia is central to acid-base homeostasis in kidney. Ammonia is produced in the proximal tubule cells from metabolism of glutamine and after several steps, finally excreted into urine along the collecting-duct intercalated cells in nephrons (15,38,39,41-44). Before the discovery of Rh proteins it was assumed that non-ammonia specific transporters achieve the transport of ammonia to the collecting-duct. However, in 2000 Marini et al. showed that the replacement of mammalian Rh proteins (RhAG and RhCG) with methyl ammonium permeases ammonium transporters (Mep) in yeast also promoted ammonium transport (45). Rh family proteins are mammalian orthologs of Amt/Mep family ammonium transporters. Until now, three Rh glycoproteins have been identified: RhAG, RhBG and RhCG (by convention RhAG and Rhag refer to human and non-human rh protein respectively; the same convention also applies to RhBG and RhCG) (46,47). RhBG and RhCG are expressed in the liver and kidney and have significant roles in renal ammonia homeostasis. On the other hand, RhAG proteins are expressed in erythrocytes and so far no indication claiming that RhAG is involved in renal ammonia homeostasis has been found.

In red blood cells (RBC), RhAG forms a complex with other Rhesus proteins (RhD and RhCE) and is needed for membrane expression of these proteins. The absence of RhAG in RBCs causes Rh antigen deprivation in RBC cell surface that leads to the Rh<sub>null</sub> disease, which results in abnormalities in RBCs such as defective cation fluxes, altered phospholipid asymmetry and increased osmotic

fragility (48-50). Several studies suggest that RhAG can mediate ammonium transport (45,51-54). Aside from transporting ammonium it has been also showed that RhAG can transport CO<sub>2</sub> (55).

RhBG and RhCG are highly expressed in the collecting-duct intercalated cells of the kidney where a substantial amount of ammonium excretion takes place. While RhCG is expressed at both apical and basolateral membranes of these cells, RhBG is expressed only in the basolateral membranes (43,56). Like for RhAG, it has been shown that RhBG and RhCG facilitate ammonium transport. Even though the majority of the studies suggest that Rh proteins transport NH<sub>3</sub>, the exact nature of the transported species remains controversial (57-60). A recent study shows that RhCG may have important roles in other biological functions, for example a study reports that deletion of RhCG proteins in mice diminished male fertility (57).

## 1. 6 Important Structural Features of RhCG

Only two crystal structures for Rh proteins have been obtained until now: the human RhCG and bacterial Rh50 (from *Nitrosomonas europaea*) (42,61). Here we will describe the important features of the human RhCG structure. Gruswitz et al. managed to crystalize the human RhCG protein and solve its structure at a resolution of 2.1 Å (PDB Id: 3HD6). RhCG is composed of 12 transmembrane helices and forms a homotrimer complex. The permeation pathway in RhCG can also be divided into extracellular vestibule, pore and intracellular vestibule regions, as in the case of AmtB. The Phe gate and pore histidine dyad observed in AmtB are also present in RhCG. A significant structural difference of RhCG compared to AmtB is that RhCG does not have a binding site for ammonium just above the Phe gate. In addition, phenylalanines forming the Phe gate (F130 and F235) in RhCG are perpendicular to each other whereas the ones in AmtB are parallel to each other.

Zidi-Yahiaoui et al. measured intracellular pH in RhCG expressed HEK293E cells in order to elucidate the importance of residues around the pore. Zidi-Yahiaoui et al. showed that individual mutations of the phenylalanines forming the Phe gate, F130A and F235V, resulted in inactive RhCG whereas F130A/F235V double mutant retained wild type activity considerably (62). They also showed that bottom histidine in the histidine dyad (H344) is absolutely required for the function of RhCG, while RhCG mutants of the upper histidine (H185) could not be expressed in the membrane. The significance of this residue remains unclear. Moreover, an aspartic acid (D177) near the pore was also shown to be crucial for ammonium transport. Mutation of this residue to asparagine caused the loss of ammonium conduction. Similar result was also reported by Marini et al. (63). These studies suggest that D177 might be involved in proton transfer pathway. Our calculations (in chapter 3) provide important evidence showing that D177 plays an important role for the transport of excess proton to the periplasmic site after deprotonation of ammonium in the pore.

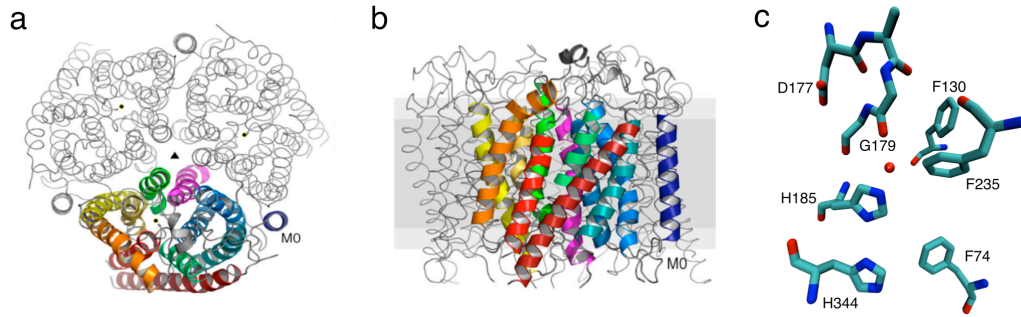


**Figure 1.3** Structure of the human RhCG protein a) Top view, b) Side view, c) Important residues around the pore. Panels a and b were adapted from Gruswitz et al. (42).

### 1. 7 Functional Studies on the Ammonium Transport in Rh Proteins

Here we briefly summarize functional studies performed to elucidate the transport mechanisms in Rh proteins and determine the exact transported species in these proteins.

Westhoff et al. heterologously expressed RhAG protein in *Xenopus* oocytes and showed that the expression of RhAG proteins increased MA uptake by 10 fold compared to the control cells. The MA uptake increased with increasing extracellular pH or decreasing intracellular pH, and was not affected by a change in membrane potential. From these results Westhoff and coworkers concluded that the transport of ammonium is electro-neutral exchange of  $\text{NH}_4^+$  and  $\text{H}^+$  (51). Westhoff et al. also suggested that the RhAG-mediated ammonium transport occurs bidirectionally based on the experiments on the yeast cells, in which RhAG are expressed in the absence of MEP transporters (52). In contrast to these results, Ripoché et al. claimed that RhAG mediates neutral transport of  $\text{NH}_3$  and  $\text{CH}_3\text{NH}_2$  based on the measurements of intracellular pH changes in the control and Rh protein complex deficient red ghost cells (53). In addition, a work of Benjelloun et al. suggested that both  $\text{NH}_3$  and  $\text{NH}_4^+$  could be transported by RhAG protein when expressed in HeLa cells (54).

Bakouh et al. measured currents and pH changes in RhCG expressed *Xenopus* oocytes in the exposure of  $\text{NH}_4\text{Cl}$ . The measurements suggested that RhCG mediates the transport of both  $\text{NH}_3$  and  $\text{NH}_4^+$  (64). Zidi-Yahiaoui et al. transfected RhBG and RhCG into human embryonic kidney cells (HEK-293) and investigated ammonium transport using stopped-flow spectrofluorimetry analysis. RhBG and RhCG expressed cells exhibited rapid alkalinization due to influx of  $\text{NH}_3$  and the  $\text{NH}_3$  transport rate is increased 6 times in comparison to wild-type HEK cells (59). Uwe Ludewig showed that RhBG expressing *Xenopus* oocytes facilitates electroneutral  $\text{NH}_4^+$  and  $\text{H}^+$  exchange using electric current and intracellular pH measurements (60). The electroneutral transport in RhBG and RhCG was also supported by the analysis of MA uptake and voltage clamping of *Xenopus* oocytes from Westhoff lab (58). Biver et al. showed that RhCG deficient mice had abnormal urinary acidification, which suggests electroneutral  $\text{NH}_3$  transport (57). Recent measurements from reconstituted RhCG proteins in liposomes led to the conclusion that RhCG transports neutral  $\text{NH}_3$  and does not require any other protein for this function (42,65). As opposed to electroneutral

transport, using voltage-clamped current measurement technique Nakhoul et al. claimed that the transport of ammonium in RhCG protein is electrogenic (66).

In conclusion, the majority of the experiments carried out to determine the ammonium transport mechanism suggests that Rh proteins mediate neutral  $\text{NH}_3$  transport.

### **1. 8 Outline for Chapters 2, 3 and 4**

In Chapter 2, we show how electrogenic ammonium transport occurs in AmtB using quantum and molecular mechanics simulations. We explain how ammonium is recruited, deprotonated and the excess proton is transferred across the hydrophobic pore via the histidine dyad.

In Chapter 3, we compare the hydration patterns of the pores of AmtB and RhCG proteins. This comparison study suggests that small differences in the pores leads to different transport mechanisms in AmtB and RhCG proteins.

In Chapter 4, we present a novel ammonium permeation mechanism in human RhCG protein using advanced computational techniques. The mechanism we propose is the first detailed mechanism describing ammonium transport in RhCG at molecular level.



## 1. 9 References

1. Javelle A, Lupo D, Li XD, Merrick M, Chami M, Ripoche P, Winkler FK. Structural and mechanistic aspects of Amt/rh proteins. *J Struct Biol* 2007, Jun;158(3):472-81.
2. Marini AM, Vissers S, Urrestarazu A, André B. Cloning and expression of the MEP1 gene encoding an ammonium transporter in *saccharomyces cerevisiae*. *EMBO J* 1994, Aug 1;13(15):3456-63.
3. Ninnemann O, Jauniaux JC, Frommer WB. Identification of a high affinity  $\text{NH}_4^+$  transporter from plants. *EMBO J* 1994, Aug 1;13(15):3464-71.
4. Javelle A, Severi E, Thornton J, Merrick M. Ammonium sensing in *escherichia coli*. Role of the ammonium transporter Amtb and Amtb-glnK complex formation. *J Biol Chem* 2004, Mar 5;279(10):8530-8.
5. Loqué D, Von Wirén N. Regulatory levels for the transport of ammonium in plant roots. *J Exp Bot* 2004;55(401):1293-305.
6. Zheng L, Kostrewa D, Bernèche S, Winkler FK, Li XD. The mechanism of ammonia transport based on the crystal structure of Amtb of *escherichia coli*. *Proc Natl Acad Sci U S A* 2004, Dec 7;101(49):17090-5.
7. Khademi S, O'Connell J, Remis J, Robles-Colmenares Y, Miercke LJ, Stroud RM. Mechanism of ammonia transport by Amt/MEP/rh: Structure of Amtb at 1.35 Å. *Science* 2004, Sep 10;305(5690):1587-94.
8. Andrade SL, Dickmanns A, Ficner R, Einsle O. Crystal structure of the archaeal ammonium transporter Amt-1 from *archaeoglobus fulgidus*. *Proc Natl Acad Sci U S A* 2005, Oct 18;102(42):14994-9.
9. Javelle A, Lupo D, Ripoche P, Fulford T, Merrick M, Winkler FK. Substrate binding, deprotonation, and selectivity at the periplasmic entrance of the *escherichia coli* ammonia channel Amtb. *Proc Natl Acad Sci U S A* 2008, Apr 1;105(13):5040-5.
10. Wang S, Orabi EA, Baday S, Bernèche S, Lamoureux G. Ammonium transporters achieve charge transfer by fragmenting their substrate. *J Am Chem Soc* 2012, Jun 27;134(25):10419-27.
11. Yang H, Xu Y, Zhu W, Chen K, Jiang H. Detailed mechanism for Amtb conducting  $\text{NH}_4^+/\text{NH}_3$ : Molecular dynamics simulations. *Biophys J* 2007, Feb 1;92(3):877-85.

12. Lin Y, Cao Z, Mo Y. Molecular dynamics simulations on the escherichia coli ammonia channel protein Amtb: Mechanism of ammonia/ammonium transport. *J Am Chem Soc* 2006, Aug 23;128(33):10876-84.
13. Nygaard TP, Rovira C, Peters GH, Jensen MØ. Ammonium recruitment and ammonia transport by E. Coli ammonia channel Amtb. *Biophys J* 2006, Dec 15;91(12):4401-12.
14. Javelle A, Lupo D, Zheng L, Li XD, Winkler FK, Merrick M. An unusual twin-his arrangement in the pore of ammonia channels is essential for substrate conductance. *J Biol Chem* 2006, Dec 22;281(51):39492-8.
15. Planelles G. Ammonium homeostasis and human rhesus glycoproteins. *Nephron Physiol* 2007;105(1):p11-7.
16. Soupene E, Lee H, Kustu S. Ammonium/methylammonium transport (Amt) proteins facilitate diffusion of NH<sub>3</sub> bidirectionally. *Proc Natl Acad Sci U S A* 2002, Mar 19;99(6):3926-31.
17. Soupene E, He L, Yan D, Kustu S. Ammonia acquisition in enteric bacteria: Physiological role of the ammonium/methylammonium transport B (Amtb) protein. *Proc Natl Acad Sci U S A* 1998, Jun 9;95(12):7030-4.
18. Fong RN, Kim KS, Yoshihara C, Inwood WB, Kustu S. The W148L substitution in the escherichia coli ammonium channel Amtb increases flux and indicates that the substrate is an ion. *Proc Natl Acad Sci U S A* 2007, Nov 20;104(47):18706-11.
19. Ludewig U, von Wirén N, Frommer WB. Uniport of NH<sub>4</sub><sup>+</sup> by the root hair plasma membrane ammonium transporter leAmt1;1. *J Biol Chem* 2002, Apr 19;277(16):13548-55.
20. Mayer M, Schaaf G, Mouro I, Lopez C, Colin Y, Neumann P, et al. Different transport mechanisms in plant and human Amt/rh-type ammonium transporters. *J Gen Physiol* 2006, Feb;127(2):133-44.
21. Mayer M, Ludewig U. Role of Amt1;1 in NH<sub>4</sub><sup>+</sup> acquisition in arabidopsis thaliana. *Plant Biol (Stuttg)* 2006, Jul;8(4):522-8.
22. Ludewig U, Wilken S, Wu B, Jost W, Obrdlik P, El Bakkoury M, et al. Homo- and hetero-oligomerization of ammonium transporter-1 NH<sub>4</sub> uniporters. *J Biol Chem* 2003, Nov 14;278(46):45603-10.
23. Ludewig U. Ion transport versus gas conduction: Function of Amt/rh-type proteins. *Transfus Clin Biol* 2006;13(1-2):111-6.

24. Mayer M, Dynowski M, Ludewig U. Ammonium ion transport by the Amt/rh homologue leAmt1;1. *Biochem J* 2006, Jun 15;396(3):431-7.
25. Ishikita H, Knapp EW. Protonation states of ammonia/ammonium in the hydrophobic pore of ammonia transporter protein Amtb. *J Am Chem Soc* 2007, Feb 7;129(5):1210-5.
26. Luzhkov VB, Almlöf M, Nervall M, Aqvist J. Computational study of the binding affinity and selectivity of the bacterial ammonium transporter Amtb. *Biochemistry* 2006, Sep 12;45(36):10807-14.
27. Bostick DL, Brooks CL. Deprotonation by dehydration: The origin of ammonium sensing in the Amtb channel. *PLoS Comput Biol* 2007, Feb 9;3(2):e22.
28. Lin Y, Cao Z, Mo Y. Functional role of asp160 and the deprotonation mechanism of ammonium in the escherichia coli ammonia channel protein Amtb. *J Phys Chem B* 2009, Apr 9;113(14):4922-9.
29. Cao Z, Mo Y, Thiel W. Deprotonation mechanism of NH<sub>4</sub><sup>+</sup> in the escherichia coli ammonium transporter Amtb: Insight from QM and QM/MM calculations. *Angew Chem Int Ed Engl* 2007;46(36):6811-5.
30. Thomas GH, Mullins JG, Merrick M. Membrane topology of the mep/Amt family of ammonium transporters. *Mol Microbiol* 2000, Jul;37(2):331-44.
31. Lamoureux G, Javelle A, Baday S, Wang S, Bernèche S. Transport mechanisms in the ammonium transporter family. *Transfus Clin Biol* 2010, Jul 29;17(3):168-75.
32. Boeckstaens M, André B, Marini AM. Distinct transport mechanisms in yeast ammonium transport/sensor proteins of the mep/Amt/rh family and impact on filamentation. *J Biol Chem* 2008, Aug 1;283(31):21362-70.
33. Lamoureux G, Klein ML, Bernèche S. A stable water chain in the hydrophobic pore of the Amtb ammonium transporter. *Biophys J* 2007, May 1;92(9):L82-4.
34. Akgun U, Khademi S. Periplasmic vestibule plays an important role for solute recruitment, selectivity, and gating in the rh/Amt/MEP superfamily. *Proc Natl Acad Sci U S A* 2011, Mar 8;108(10):3970-5.
35. Orabi EA, Lamoureux G. Cation-  $\pi$  and  $\pi$ - $\pi$  interactions in aqueous solution studied using polarizable potential models. *J Chem Theory Comput* 2011;8(1):182-93.

36. Butterworth RF. Hepatic encephalopathy. *Alcohol Res Health* 2003;27(3):240-6.
37. Butterworth RF. Pathophysiology of hepatic encephalopathy: A new look at ammonia. *Metab Brain Dis* 2002;17(4):221-7.
38. Wagner CA, Devuyst O, Belge H, Bourgeois S, Houillier P. The rhesus protein rhcg: A new perspective in ammonium transport and distal urinary acidification. *Kidney Int* 2011, Jan;79(2):154-61.
39. Wagner CA, Devuyst O, Bourgeois S, Mohebbi N. Regulated acid-base transport in the collecting duct. *Pflugers Arch* 2009, May;458(1):137-56.
40. Kraut JA, Madias NE. Metabolic acidosis: Pathophysiology, diagnosis and management. *Nature Reviews Nephrology* 2010;6(5):274-85.
41. Weiner ID, Verlander JW. Role of NH<sub>3</sub> and NH<sub>4</sub><sup>+</sup> transporters in renal acid-base transport. *Am J Physiol Renal Physiol* 2011, Jan;300(1):F11-23.
42. Gruswitz F, Chaudhary S, Ho JD, Schlessinger A, Pezeshki B, Ho CM, et al. Function of human rh based on structure of rhcg at 2.1 Å. *Proc Natl Acad Sci U S A* 2010, May 10;107(21):9638-43.
43. Weiner ID, Hamm LL. Molecular mechanisms of renal ammonia transport. *Annu Rev Physiol* 2007;69:317-40.
44. Weiner ID, Verlander JW. Molecular physiology of the rh ammonia transport proteins. *Curr Opin Nephrol Hypertens* 2010;19(5):471-7.
45. Marini AM, Matassi G, Raynal V, André B, Cartron JP, Chérif-Zahar B. The human rhesus-associated rhag protein and a kidney homologue promote ammonium transport in yeast. *Nat Genet* 2000;26(3):341-4.
46. Liu Z, Chen Y, Mo R, Hui C, Cheng JF, Mohandas N, Huang CH. Characterization of human rhcg and mouse rhcg as novel nonerythroid rh glycoprotein homologues predominantly expressed in kidney and testis. *J Biol Chem* 2000, Aug 18;275(33):25641-51.
47. Liu Z, Peng J, Mo R, Hui C, Huang CH. Rh type B glycoprotein is a new member of the rh superfamily and a putative ammonia transporter in mammals. *J Biol Chem* 2001, Jan 12;276(2):1424-33.
48. Sturgeon P. Hematological observations on the anemia associated with blood type rhnull. *Blood* 1970, Sep;36(3):310-20.
49. Cartron JP. RH blood group system and molecular basis of rh-deficiency. *Baillieres Best Pract Res Clin Haematol* 1999, Dec;12(4):655-89.

50. Avent ND, Reid ME. The rh blood group system: A review. *Blood* 2000, Jan 15;95(2):375-87.
51. Westhoff CM, Ferreri-Jacobia M, Mak DO, Foskett JK. Identification of the erythrocyte rh blood group glycoprotein as a mammalian ammonium transporter. *J Biol Chem* 2002, Apr 12;277(15):12499-502.
52. Westhoff CM, Siegel DL, Burd CG, Foskett JK. Mechanism of genetic complementation of ammonium transport in yeast by human erythrocyte rh-associated glycoprotein. *J Biol Chem* 2004, Apr 23;279(17):17443-8.
53. Ripoche P, Bertrand O, Gane P, Birkenmeier C, Colin Y, Cartron JP. Human rhesus-associated glycoprotein mediates facilitated transport of NH<sub>3</sub> into red blood cells. *Proc Natl Acad Sci U S A* 2004, Dec 7;101(49):17222-7.
54. Benjelloun F, Bakouh N, Fritsch J, Hulin P, Lipecka J, Edelman A, et al. Expression of the human erythroid rh glycoprotein (rhag) enhances both NH<sub>3</sub> and NH<sub>4</sub><sup>+</sup> transport in hela cells. *Pflugers Arch* 2005, Jun;450(3):155-67.
55. Endeward V, Cartron JP, Ripoche P, Gros G. RhAG protein of the rhesus complex is a CO<sub>2</sub> channel in the human red cell membrane. *FASEB J* 2008, Jan;22(1):64-73.
56. Han KH, Croker BP, Clapp WL, Werner D, Sahni M, Kim J, et al. Expression of the ammonia transporter, rh C glycoprotein, in normal and neoplastic human kidney. *Journal of the American Society of Nephrology* 2006;17(10):2670-9.
57. Biver S, Belge H, Bourgeois S, Van Vooren P, Nowik M, Scohy S, et al. A role for rhesus factor rhcg in renal ammonium excretion and male fertility. *Nature* 2008, Nov 20;456(7220):339-43.
58. Mak DO, Dang B, Weiner ID, Foskett JK, Westhoff CM. Characterization of ammonia transport by the kidney rh glycoproteins rhbg and rhcg. *Am J Physiol Renal Physiol* 2006, Feb;290(2):F297-305.
59. Zidi-Yahiaoui N, Mouro-Chanteloup I, D'Ambrosio AM, Lopez C, Gane P, Le van Kim C, et al. Human rhesus B and rhesus C glycoproteins: Properties of facilitated ammonium transport in recombinant kidney cells. *Biochem J* 2005, Oct 1;391(Pt 1):33-40.
60. Ludewig U. Electroneutral ammonium transport by basolateral rhesus B glycoprotein. *J Physiol* 2004, Sep 15;559(Pt 3):751-9.

61. Lupo D, Li XD, Durand A, Tomizaki T, Cherif-Zahar B, Matassi G, et al. The 1.3-Å resolution structure of nitrosomonas europaea rh50 and mechanistic implications for NH<sub>3</sub> transport by rhesus family proteins. *Proc Natl Acad Sci U S A* 2007, Dec 4;104(49):19303-8.

62. Zidi-Yahiaoui N, Callebaut I, Genetet S, Le Van Kim C, Cartron JP, Colin Y, et al. Functional analysis of human rhcg: Comparison with E. Coli ammonium transporter reveals similarities in the pore and differences in the vestibule. *American Journal of Physiology-Cell Physiology* 2009;297(3):C537-47.

63. Marini AM, Boeckstaens M, Benjelloun F, Chérif-Zahar B, André B. Structural involvement in substrate recognition of an essential aspartate residue conserved in mep/Amt and rh-type ammonium transporters. *Curr Genet* 2006, Jun;49(6):364-74.

64. Bakouh N, Benjelloun F, Hulin P, Brouillard F, Edelman A, Chérif-Zahar B, Planelles G. NH<sub>3</sub> is involved in the NH<sub>4</sub><sup>+</sup> transport induced by the functional expression of the human rh C glycoprotein. *J Biol Chem* 2004, Apr 16;279(16):15975-83.

65. Mouro-Chanteloup I, Cochet S, Chami M, Genetet S, Zidi-Yahiaoui N, Engel A, et al. Functional reconstitution into liposomes of purified human rhcg ammonia channel. *PLoS ONE* 2010;5(1):e8921.

66. Nakhoul NL, Schmidt E, Abdounour-Nakhoul SM, Hamm LL. Electrogenic ammonium transport by renal rhbg. *Transfus Clin Biol* 2006;13(1-2):147-53.

## Chapter 2

### AMMONIUM TRANSPORTERS ACHIEVE CHARGE TRANSFER BY FRAGMENTING THEIR SUBSTRATE

This chapter was published in the Journal of the American chemical society (JACS, 2012, 134, 10419-10427) by the following authors: Shihao Wang, Esam A. Orabi, Sefer Baday, Simon Berneche, and Guillaume Lamoureux.

Sefer Baday involved in preparation of the AmtB simulation system, setting up ABF simulation for ammonia diffusing through the pore and PMF calculation for the reset of histidine dyad, and discussions of the results.

## 2.1 Abstract

Proteins of the Amt/MEP family facilitate ammonium transport across the membranes of plants, fungi, and bacteria, and are essential for growth in nitrogen-poor environments. Some are known to facilitate the diffusion of the neutral  $\text{NH}_3$  while others, notably in plants, transport the positively charged  $\text{NH}_4^+$ . Based on the structural data for AmtB from *Escherichia coli*, we illustrate the mechanism by which proteins from the Amt family can sustain electrogenic transport. Free energy calculations show that  $\text{NH}_4^+$  is stable in the AmtB pore, reaching a binding site from which it can spontaneously transfer a proton to a pore-lining histidine residue (His168). The substrate diffuses down the pore in the form of  $\text{NH}_3$  while the excess proton is co-transported through a highly conserved hydrogen-bonded His168-His318 pair. This constitutes a novel permeation mechanism that confers to the histidine dyad an essential mechanistic role that was so far unknown.



## 2.1 Introduction

Ammonium transport proteins have been found in all domains of life, notably in plants (1), bacteria (2), and mammals (3,4). They facilitate the membrane transport of ammonium, which is an important nitrogen source for organisms such as bacteria, fungi, and plants (1,5), but a toxic metabolic waste product for others, such as mammals (4,6). The X-ray structures of bacterial ammonium transporter AmtB (7-12), show a permeation pathway consisting of three regions (Figure 2.1.a): a periplasmic vestibule, at the bottom of which is a binding site (S1) involved in ammonium recruitment; a gate formed of two phenylalanine residues (Phe107 and Phe215), whose function has not been fully established yet; and a narrow and hydrophobic pore lined with two hydrogen-bonded histidine residues (His168 and His318), in which various binding sites have been crystallographically identified (8,10-12). In the present work, we call “S2” the site where a substrate forms a hydrogen bond with His168 and “S4” the site where it forms a hydrogen bond with His318. The region between S2 and S4 is indistinctly called “S3”.

The recruitment of  $\text{NH}_4^+$  in the periplasmic vestibule has been confirmed by structural and functional studies (9,11,12) and by simulations (13-19). Under physiological pH, ammonium exists predominantly in its ionic form ( $\text{NH}_4^+$ ) and the electron density maximum observed in the periplasmic vestibule of the AmtB channel is consistent with an ion forming cation- $\pi$  interactions with aromatic amino acids Phe107 and Trp148, and an H-bond to Ser219. The identity of the transported species and the mechanism of transport have, however, not been confirmed so far. Because  $\text{H}_2\text{O}$ ,  $\text{NH}_3$ , and  $\text{NH}_4^+$  are isoelectronic molecules, they cannot be distinguished in the X-ray structures and their assignment to electron density maxima remains hypothetical. In that regard, computer simulations based on quantum chemistry are an invaluable tool to investigate the affinity of the protein for the different forms of the substrate and the underlying transport mechanisms.

Based on experimental studies of various proteins of the Amt family, three transport mechanisms have been suggested: electroneutral  $\text{NH}_3$  transport (9,11,12,14,16-18,20,21),  $\text{NH}_3/\text{H}^+$  co-transport (9,22,23), and  $\text{NH}_4^+$  transport (1,2,5,24,25). Despite this seemingly contradictory evidence, most theoretical studies (13,15,19,26-28) have focused on electroneutral  $\text{NH}_3$  transport

mechanisms, in which  $\text{NH}_4^+$  deprotonates in the periplasmic vestibule and a neutral  $\text{NH}_3$  permeates through the pore, leaving the charge on the periplasmic side. This mechanism, however, leaves many experimental results unexplained (9,10,25). Electrophysiological studies of plant Amt (25) have confirmed a net charge transport across the membrane, which suggests that the transported substrate is either  $\text{NH}_4^+$  or  $\text{NH}_3/\text{H}^+$ . While the  $\text{NH}_3/\text{H}^+$  co-transport hypothesis has been raised by many authors (22,29), it has not been demonstrated from a mechanistic perspective. Using computational methods based on quantum chemistry and statistical mechanics we elucidate the pathway allowing for the binding of  $\text{NH}_4^+$  and its subsequent splitting into  $\text{NH}_3$  and  $\text{H}^+$ . Our findings notably show that Amt's signature histidines are central for proton transport.

## 2.2 Results and Discussion

### 2.2.1 Recruitment of $\text{NH}_4^+$ in site S1

The stability of  $\text{NH}_4^+$  in S1 was investigated using five independent 2-ns hybrid polarizable mechanics/molecular mechanics (PM/MM) simulations. Residues around site S1 are represented by polarizable models specifically parameterized to reproduce the complexation energies between  $\text{NH}_4^+$  and a series of model compounds that represent protein side chains (see Appendix, Figure 2.8, Figure 2.9, Table 2.2 and Table 2.3).  $\text{NH}_4^+$  remains stable in site S1 along all simulations, at a position in agreement with site Am1 from the crystal structure of Khademi *et al* (11). (Figure 2.1.b), and in line with simulations from other groups (15,23,38).  $\text{NH}_4^+$  forms a cation- $\pi$  interaction with Trp148 most of the time, but it occasionally separates to form a cation- $\pi$  interaction with Phe103 (Figure 2.1.b). The average distances from  $\text{NH}_4^+$  to Ser219, Phe107, Phe103, Trp148, and H-bonding water are 2.8 Å, 3.7 Å, 5.9 Å, 4.2 Å, 2.8 Å, respectively (see Table 2.4). During the simulations, the so-called hydrophobic pore is filled with water molecules, at positions in excellent agreement with the density observed in the 1U7G and 1XQF crystal structures (Figure 2.1.c). This is consistent with our previous findings (30) and suggests that the pore in the crystal structures is occupied by water. While this conclusion appears to be somewhat force-field dependent (13,16,30), there is little doubt that the electronic density observed in the 1XQF structure is due to water, since the protein was crystallized in absence of ammonium salt (12).

Binding affinity of  $\text{NH}_4^+$  for S1 is calculated from the free energy associated with the  $\text{H}_2\text{O} \rightarrow \text{NH}_4^+$  alchemical transformation (31) in the binding site, relative to the free energy associated with the same transformation in liquid water. The free energy difference represents the thermodynamic cost of exchanging an ammonium ion in the periplasm with a water molecule in the binding site. As shown in Table 2.1, the  $\text{NH}_4^+$  binding affinity in S1 is  $-14.1 \pm 1.5$  kcal/mol, corresponding to a dissociation constant of 2.55 nM. By comparison, Luzhkov *et al.* (16), using a conventional (non-polarizable) force field, have calculated  $\Delta\Delta G_{\text{bind}}(\text{H}_2\text{O} \rightarrow \text{NH}_4^+)$  in S1 to be  $-5.8$  kcal/mol, corresponding to a dissociation constant of 3.1 mM. This millimolar affinity is too low to explain the observed activity of Amt proteins, since *E. coli* can grow normally without a functional

AmtB protein down to ammonium concentrations of  $\sim 0.1 \mu\text{M}$  (21), and since AmtB is actually being inactivated for ammonium concentrations greater than  $\sim 5\text{--}50 \mu\text{M}$  (32). The nanomolar affinity of S1 for ammonium ions is consistent with that of known benzene-based, synthetic receptors. For instance, Ahn et al. (32) have synthesized a tripodal oxazoline receptor that binds  $\text{NH}_4^+$  with an affinity of  $40 \text{ nM}$  ( $K_a = 2.5 \times 10^7 \text{ M}^{-1}$ ) and a free energy of  $-12.5 \text{ kcal/mol}$ .

The high binding affinity in S1 is partially due to cation- $\pi$  interactions resulting from the direct coordination of  $\text{NH}_4^+$  with Phe107 and Trp148. A number of computational investigations have shown that, in aqueous solution,  $\text{NH}_4^+$ - $\pi$  interactions are significantly stronger than  $\text{NH}_4^+$ -water interactions (34-36). For instance, Gallivan and Dougherty (35) have estimated the binding free energy of a methylammonium-benzene pair in solution to be  $-5.5 \text{ kcal/mol}$  (compared to  $-2.2 \text{ kcal/mol}$  for a methylammonium-acetate pair). Sa *et al.* (36) have performed Car-Parrinello molecular dynamics simulations of an ammonium-benzene pair in aqueous solution and estimated the “cation- $\pi$ ” binding free energy to be  $-5.75 \text{ kcal/mol}$ .

Experimental studies on AmtB (9) and other Amt proteins (1,25) have shown that site S1 is selective for  $\text{NH}_4^+$  over biologically abundant cations  $\text{Na}^+$  and  $\text{K}^+$ . These ions do not permeate the proteins and do not even inhibit their ammonium-transport activity (1,9,25,37). We have calculated the binding free energies of  $\text{Na}^+$  and  $\text{K}^+$  from the free energies associated with the  $\text{NH}_4^+ \rightarrow \text{Na}^+$  and  $\text{NH}_4^+ \rightarrow \text{K}^+$  transformations, using a polarizable force field for all three ions (see Appendix). Compared to  $\text{NH}_4^+$ , the resulting binding affinities are reduced by  $9.2 \text{ kcal/mol}$  for  $\text{Na}^+$  and  $8.2 \text{ kcal/mol}$  for  $\text{K}^+$  (Table 2.1), which confirms that none of these ions would inhibit ammonium binding at physiological concentrations. The high selectivity of site S1 for  $\text{NH}_4^+$  is due to the specific coordination environment composed of the aromatic rings of Phe107 and Trp148, the hydroxyl group of Ser219, and two water molecules. While the number of coordinating ligands in S1 is comparable to that of  $\text{NH}_4^+$  in solution (4 to 5 water molecules (22)), it is lower than that of  $\text{Na}^+$  or  $\text{K}^+$  (5 to 6 for sodium and 6 to 7 for potassium (38)).

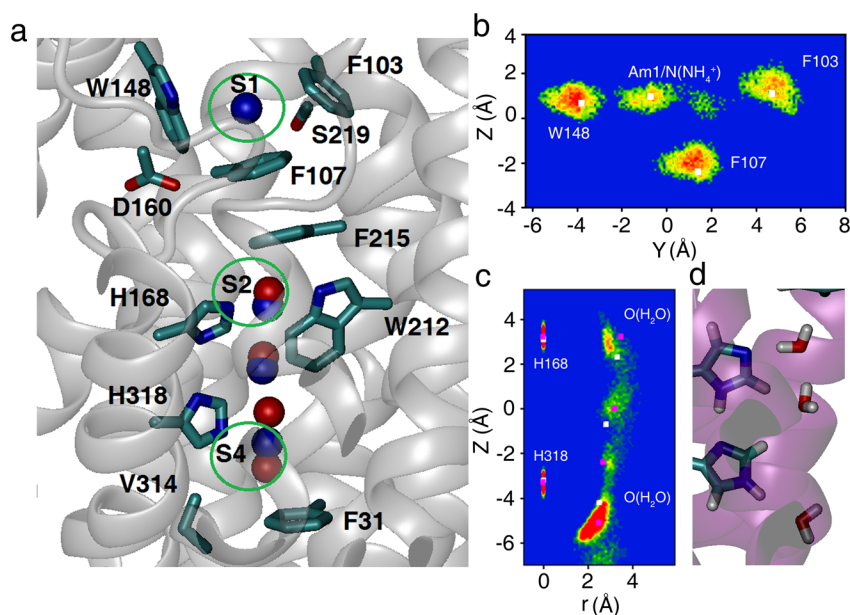


**Figure 2.1** (a) Crystal structure of AmtB monomer (PDB id: 1U7G) (11). The locations of four density maxima identified by Khademi *et al.* (11) are marked as blue spheres. For comparison, four density maxima identified by Winkler *et al.* (PDB id: 1XQF, personal communication) (11) are marked as red spheres. Sites S1, S2, and S4 are depicted as green circles. Distribution of (b)  $\text{NH}_4^+$  in site S1 and of (c) water in the AmtB pore, from 60 ns PM/MM simulations. In panel (b), positions are projected onto YZ plane and the distributions of ammonium nitrogen and centers of mass of F103, F107 and W148 rings are shown. In panel (c), positions are represented in cylindrical coordinates, using the Ne atoms of His168 and His318 as principal axis. Distributions of water oxygen and Ne atoms of His168 and His318 are shown. The density maxima from 1U7G and 1XQF crystal structures are shown as white and purple dots, respectively. A corresponding snapshot is shown in panel (d).

### 2.2.2 Affinity of $\text{NH}_4^+$ in site S2

We have investigated the probability of  $\text{NH}_4^+$  reaching the S2 binding site, which is separated from S1 by the two phenyl rings of Phe107 and Phe215. An ion bound to site S2 would be coordinated by residues Phe215, Trp212, and His168. Most of these residues are conserved throughout the Amt/MEP family (11,12) and mutagenesis studies on AmtB have shown that mutants F215A, W212A, and H168A are all inactive (9,10). Interestingly, mutant W212F, which preserves the aromatic character of the residue and therefore its ability to form a cation- $\pi$  interaction with a charged substrate in S2, remains 80% active (9). This

observation, along with the fact that Trp212 is conserved either as Trp or Phe in all members of the Amt/MEP family, is suggesting that S2 is a cation-binding site and that tight ion-protein coordination in S2 is essential for transport.

The stability of  $\text{NH}_4^+$  at site S2 was investigated using two methods: PM/MM simulations as for site S1 and hybrid quantum mechanics/molecular mechanics (QM/MM) simulations.  $\text{NH}_4^+$  is initially placed at S2 and allowed to move freely, and the section of the pore below S2 is filled with water. The His168-His318 pair has two tautomers, depending on which of the two histidines is the hydrogen bond donor to the other. The “His168–H···His318–H” structure (see Figure 2.1.d) is considered to be the functional state at the time the substrate reaches S2. The reverse “H–His168···H–His318” state, which has a hydrogen atom pointing towards S2, would create an unfavorable electrostatic clash with  $\text{NH}_4^+$  in S2. The distributions of  $\text{NH}_4^+$  and water molecules in the pore are presented in Figure 2.2.a and Figure 2.2.b.  $\text{NH}_4^+$  maintains a strong hydrogen bond to His168 throughout both the 4-ns PM/MM simulation and the 60-ps QM/MM simulation. According to the PM/MM simulations, the average distances from  $\text{NH}_4^+$  to His168, Phe215, Trp148 and H-bonding water are 3.0 Å, 3.2 Å, 3.2 Å, and 3.0 Å, respectively. The positions of ammonium, water and His168 are represented by nitrogen, oxygen, and Nε, respectively. For Phe215 and Trp148, the positions are represented by the center of their six-membered rings. Although  $\text{NH}_4^+$  is stable in S2, and favors the formation of a highly structured water chain in the pore (Figure 2.2.a), its position does not correspond to any of the density maxima identified from X-ray crystallography, which are likely to represent water in a substrate-free pore (see Figure 2.1.c).

The position of  $\text{NH}_4^+$  is more diffuse for the QM/MM simulations (Figure 2.2.b), because they allow  $\text{NH}_4^+$  to deprotonate and represent a mixture of two states: an  $\text{NH}_4^+$  ion bound to a neutral His168 and an  $\text{NH}_3$  molecule bound to a protonated His168. The water molecules are more dynamic as well, showing a binding pattern extending away from the histidine scaffold. Free QM/MM simulations with methylammonium ( $\text{CH}_3\text{NH}_3^+$ , also known to permeate (11)) in S2 yield distributions similar to those of Figure 2.2.b, also involving proton transfer between  $\text{CH}_3\text{NH}_3^+$  and His168.

As reported in Table 2.1, the calculated  $\text{NH}_4^+$  binding affinity in site S2 is  $-13.0 \pm 1.0$  kcal/mol, which indicates that  $\text{NH}_4^+$  is almost as stable in S2 as it is in

S1. This large binding free energy is consistent with mutagenesis data (9,39) showing that AmtB retains its activity even for a highly disrupted S1 site. The high ammonium affinity of S2 would explain why the triple mutant F107A/W148A/S219A (in which the Phe, Trp and Ser residues around S1 are mutated to alanine) is even more active than the wild-type protein (9). In stark contrast, Luzhkov *et al.* (16) report a free energy barrier of +22.1 kcal/mol when the pore is filled with ammonia instead of water, using a conventional non-polarizable force field.

It is expected that the translocation of  $\text{NH}_4^+$  from S1 to S2 requires a transient reorganization of the aromatic side chains of Phe107 and Phe215. In accordance with a number of simulation studies (13,15,18), our simulations show that the side chains of Phe107 and Phe215 frequently rotate and adopt conformations in which the two aromatic rings are perpendicular and form an “L” shape susceptible to bind  $\text{NH}_4^+$  at an intermediate position between S1 and S2. An ammonium ion at that position would be stabilized by an H-bond with the Ala162 backbone, which would significantly reduce the translocation energy barrier. Mutagenesis data from Javelle *et al.* (9) show that F107A variant remains active but that variant F215A and double variant F107A/F215A are inactive, yet that none of these mutants leak water. This suggests that the phenylalanine gate is not so much preventing water from diffusing as it is providing key residues leading the substrate to S2 and stabilizing it in the vicinity of His168. Given the binding free energies of  $\text{NH}_4^+$  at S1 and S2 (−14.1 and −13.0 kcal/mol, respectively), the probability of the substrate going to S2 is much greater than the probability of it going back to the periplasm—irrespective of the details of the translocation mechanism.

**Table 2.1** Relative binding free energies of  $\text{NH}_4^+$ ,  $\text{Na}^+$  and  $\text{K}^+$  at the S1, S2 and S4 sites (in kcal/mol)

Mutation (Site)	$\Delta G_{mut}^{prot}$	$\Delta G_{mut}^{wat}$	$\Delta\Delta G_{bind}$ $\Delta G_{mut}^{prot} - \Delta G_{mut}^{wat}$	$K_d$ (nM) <sup>†</sup>
$\text{H}_2\text{O} \rightarrow \text{NH}_4^+$ (S1)	$-75.8 \pm 1.3^*$	$-61.7 \pm 0.8^{*,a}$	$-14.1 \pm 1.5$	2.56
$\text{H}_2\text{O} \rightarrow \text{NH}_4^+$ (S2)	$-74.7 \pm 0.6^*$	$-61.7 \pm 0.8^{*,a}$	$-13.0 \pm 1.0$	16.4
$\text{H}_2\text{O} \rightarrow \text{NH}_4^+$ (S4)	$-70.2 \pm 0.9^*$	$-61.7 \pm 0.8^{*,a}$	$-8.6 \pm 1.4$	$2.73 \times 10^5$
$\text{H}_2\text{O} \rightarrow \text{Na}^+$ (S1)	-85.2	$-80.3^b$	-4.9	$1.42 \times 10^7$
$\text{H}_2\text{O} \rightarrow \text{K}^+$ (S1)	-68.8	$-62.9^c$	-5.9	$2.62 \times 10^6$

\* Errors are standard deviations from five independent simulations.

<sup>†</sup> Equivalent dissociation constant calculated from  $[W] \cdot \exp(\Delta\Delta G_{bind}/k_B T)$ , where [W] is the concentration of water (55.4 M) and  $k_B$  is Boltzmann constant.

<sup>a</sup> Experimental value is  $-68.1 + 12.6 - 6.32 = -61.8$  kcal/mol (using  $-6.32$  kcal/mol as the experimental hydration free energy of water) (77,78). Unlike solvation free energies, the calculated  $\Delta G$  values do not contain the contribution from crossing the air-water interface ( $-12.6$  kcal/mol for the SWM4-NDP model) (68,79).

<sup>b</sup> Experimental value is  $-87.2 + 12.6 - 6.32 = -80.9$  kcal/mol (78).

<sup>c</sup> Experimental value is  $-70.5 + 12.6 - 6.32 = -64.2$  kcal/mol(78).



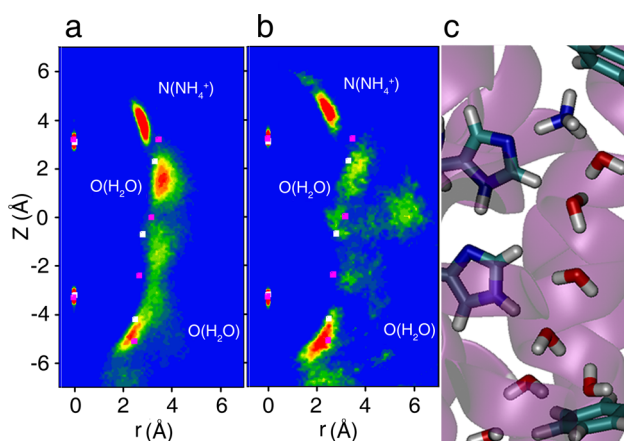


**Figure 2.2** Distribution of  $\text{NH}_4^+$  in S2 and of water in the pore, from (a) 4 ns PM/MM simulations and (b) 60 ps QM/MM simulations. Positions are represented as in Fig. 1c. Distributions of ammonium nitrogen, water oxygen, and Ne atoms of His168 and His318 are shown. For reference, the density maxima from 1U7G and 1XQF crystal structures are shown as white and purple dots, respectively. Panel (c) illustrates a representative configuration of the molecules.

### 2.2.3 Mechanism of $\text{NH}_4^+$ deprotonation in S2

We investigated two mechanisms for ammonium deprotonation at S2: 1) through the histidine side chains and 2) through the water chain in the pore (Figure 2.3). Water chains are common proton pathways in proteins and in nanotubes (40-44) but are most effective when water molecules are the only available proton acceptors. In presence of a better proton acceptor, such as ammonia or the unsaturated nitrogen atom of a histidine side chain, the proton conductivity of the chain may be significantly reduced (45,46). Imidazole, a model compound for the histidine side chain, has a higher proton affinity than water (225.2 kcal/mol versus 165.1 kcal/mol for water (47)) and a higher basicity (7.0 versus  $-1.74$ ).

The two deprotonation mechanisms are analyzed by calculating the potentials of mean force (PMFs) of proton transfer using constrained QM/MM simulations. The free energy barrier for the proton transfer from  $\text{NH}_4^+$  to His168 is only 1.7 kcal/mol, and the two protonation states are almost equally stable (Figure 2.3.a). In contrast, proton transfer from  $\text{NH}_4^+$  to the adjacent water molecule is prohibited (Figure 2.3.b). As the excess proton is pushed towards the water molecule,

forming an  $\text{H}_3\text{O}^+$  ion, the system becomes chemically unstable and another proton is quickly transferred from  $\text{H}_3\text{O}^+$  to  $\text{NH}_3$ .

This finding is consistent with the unconstrained QM/MM simulations of  $\text{NH}_4^+$  in S2. In these simulations proton transfer between  $\text{NH}_4^+$  and His168 happens about 40 times in 60 ps. Proton transfer between His168 and His318 is also observed (8 times in 60 ps), indicating that  $\text{NH}_4^+$ , His168, and His318 form a charge-delocalized structure<sup>42</sup> that entropically stabilizes the excess positive charge. The distribution of protons from the unconstrained simulations is converted into proton transfer PMFs using the equation

$$W(X) = -k_{\text{B}}T \ln \rho(X)$$

where  $\rho(X)$  is the distribution of reaction coordinate  $X$  and  $W(X)$  is the corresponding PMF (see dashed lines in Figure 2.3.a and Figure 2.3.c). Proton transfer events between  $\text{NH}_4^+$  and His168 are frequent enough that the unconstrained QM/MM PMF is statistically converged. The energy barrier for the proton transfer between His168 and His318 is 2.8 kcal/mol (Figure 2.3.c), which is higher than that for the transfer between  $\text{NH}_4^+$  and His168 but is low enough to be sampled at the picosecond time scale. The two protonation states have the same free energy.

The deprotonation mechanism observed in the QM/MM simulations is consistent with *ab initio* energy profiles calculated for the proton transfer reactions from an ammonium ion to imidazole (representing His168) and from an ammonium ion to water (see Figure 2.11.a). Based on comparisons with *ab initio* calculations performed in various implicit solvents, it appears that the protein environment of a histidine-bound ammonium in S2 has a polarity intermediate to that of liquid benzene and liquid water, such that the substrate exists both as  $\text{NH}_4^+$  and as  $\text{NH}_3$  bound to a protonated histidine.

The QM/MM simulations provide the following picture: As soon as  $\text{NH}_4^+$  reaches site S2, the excess proton delocalizes in three tautomeric forms:  $\text{NH}_4^+ \cdots \text{His168} \cdots \text{His318}$ ,  $\text{NH}_3 \cdots \text{His168H}^+ \cdots \text{His318}$ , and  $\text{NH}_3 \cdots \text{His168} \cdots \text{His318H}^+$ . The three forms are almost iso-energetic and exchange on the picosecond time scale: on average every  $\sim 1.5$  ps between ammonia and His168 and every  $\sim 7.5$  ps between His168 and His318. This charge-delocalized structure stabilizes the excess proton and may further increase the  $\text{NH}_4^+$  affinity of the S2 binding site.

These findings suggest that the His168-His318 dyad, which is highly conserved among proteins of the Amt/MEP family, is essential for ammonium binding and deprotonation. This is consistent with the fact that mutants H168A, H168F, H318A and H318F are all inactive (10), as none of these variants can H-bond to  $\text{NH}_4^+$  and serve as general base for deprotonation. The H168E mutant, on the other hand, retains 25% of the wild-type activity (10,39), consistent with the fact that the two side chains have similar basicities (9.2 for acetic acid, versus 7.0 for imidazole) and can form an H-bond with residue His318. We have performed two independent 30-ps unconstrained QM/MM simulations of the H168E mutant (where His168 is replaced by a neutral Glu, acting as H-bond donor to His318), which display a similar deprotonation process and fast proton movement across  $\text{NH}_4^+\cdots\text{Glu168}\cdots\text{His318}$ . This indicates that the deprotonation mechanism is robust and could be operating in fungal homologs having a Glu residue at position 168 (48).

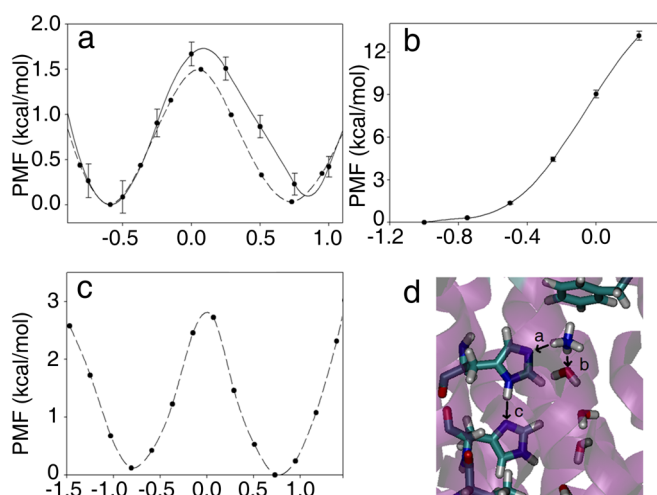


**Figure 2.3** Potentials of mean force (PMFs) for proton transfer reactions involving ammonium in site S2: (a) from ammonium to His168, (b) from ammonium to pore water, and (c) from His168 to His318. Panel (d) illustrates the proton transfer reactions, and the arrows correspond to the reaction from left to right in each panel. The results from constrained and unconstrained QM/MM simulations are shown in solid and dashed lines, respectively. Reaction coordinates are defined as:  $RC = d_{N(\text{amm})-\text{H}} - d_{N\epsilon(\text{His168})-\text{H}}$  for panel (a),  $RC = d_{N(\text{amm})-\text{H}} - d_{O(\text{wat})-\text{H}}$  for panel (b), and  $RC = d_{N\delta(\text{His168})-\text{H}} - d_{N\delta(\text{His318})-\text{H}}$  for panel (c). Note the different energy scales in panels (a)–(c). Error bars in panels (a) and (b) are calculated from the block averaging of mean forces (66).

#### 2.2.4 $\text{NH}_3$ diffusion along the protonated His168-His318 dyad

The leaving of  $\text{NH}_3$  from S2 creates a more confined charge-delocalized structure that has only two protonation states:  $\text{His168H}^+ \cdots \text{His318}$  and  $\text{His168} \cdots \text{His318H}^+$ . These two states are almost equally populated (Figure 2.3.c), and alternate at a rate faster than the substrate diffusion process. The proton transfer between His168 and His318 has a time scale of  $\sim 7.5$  ps, but not a single  $\text{NH}_3$  translocation event was observed in 60 ps of unconstrained QM/MM simulations. The  $\text{NH}_3$  substrate diffusing down the pore is therefore experiencing the field created by a mixture of both protonation states.

PMFs of  $\text{NH}_3$  diffusion are calculated using the adaptive biasing force (ABF) method for both the “His168H<sup>+</sup>” and “His318H<sup>+</sup>” states (Figure 2.4). The two states give slightly different free energy profiles, but both display low energy

barriers to  $\text{NH}_3$  diffusion. The average PMF, representing the force actually experienced by the substrate, is shown as a dotted line in Figure 2.4.a. Note that in its neutral  $\text{NH}_3$  form, the substrate is more likely to leave site S2 by exchanging with a water molecule in the pore than re-crossing the Phe107/Phe215 gate (Figure 2.4.a). The overall diffusion process is essentially barrierless.

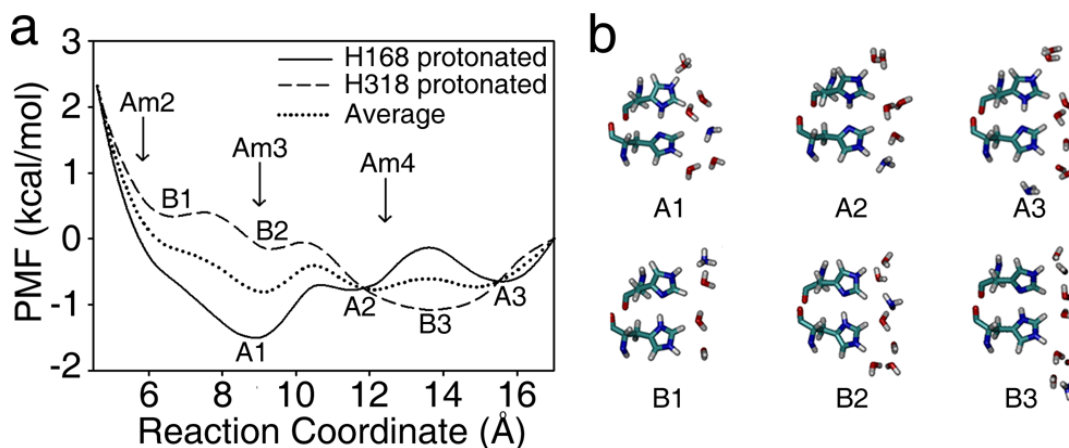


**Figure 2.4** PMFs for  $\text{NH}_3$  permeation after deprotonation at site S2. Two protonation states of the histidine side chains are considered: “His168 protonated” (solid-line PMF, snapshots A1 to A3) and “His318 protonated” (dashed-line PMF, snapshots B1 to B3). The reaction coordinate is the z-coordinate offset of ammonia from center of the Phe107 ring. The positions of sites Am2, Am3 and Am4 are from structure 1U7G (11).

### 2.2.5 Re-protonation of $\text{NH}_3$ at site S4

The excess proton is most likely to remain bound to the histidine side chains as long as sites S2 and S4 are occupied by water molecules, which are poor acceptors for the histidine protons (Figure 2.11.d). However, as soon as  $\text{NH}_3$  reaches S4 the excess proton has a much higher probability of transfer.  $\text{NH}_3$  is more exposed to solvent in site S4 than in site S2. The ABF simulations show that  $\text{NH}_3$  is usually coordinated by one water molecule in S2 but by 2 to 3 water molecules in S4. This increase in polarity of the environment stabilizes the  $\text{His318}\cdots\text{NH}_4^+$  form over the  $\text{His318H}^+\cdots\text{NH}_3$  one (Figure 2.11.a).

We investigated the re-protonation of  $\text{NH}_3$  in S4 using two independent 30-ps unconstrained QM/MM simulations, in which  $\text{NH}_3$  is initially placed at hydrogen-bonding position from His318 and is allowed to move freely. The substrate is

most likely found at this position (Figure 2.5.c) but it occasionally moves away and binds His318 through a water molecule (Figure 2.5.d). This corresponds to the secondary density maximum of Fig. 5a, at  $Z \sim -6 \text{ \AA}$ . During the QM/MM simulations, proton transfer is observed for  $\text{NH}_3$  at both positions, directly or through a water bridge (Figure 2.12). In both cases the substrate remains in contact with the aromatic ring of Phe31, which may provide a stabilizing cation- $\pi$  interaction for  $\text{NH}_4^+$  on its way to the cytoplasm. The re-protonation of  $\text{NH}_3$  was further analyzed using constrained QM/MM simulations. The free energy barrier for the proton transfer from His318 to  $\text{NH}_3$  is 2.5 kcal/mol, and the free energy of reaction is 1.3 kcal/mol (Figure 2.11.e).

As reported in Table 2.1, the calculated  $\text{NH}_4^+$  binding affinity in site S4 is  $-8.6 \pm 1.4$  kcal/mol, corresponding to a dissociation constant of 2–290  $\mu\text{M}$ . Considering that the internal  $\text{NH}_4^+$  concentration is expected to be lower than the micromolar (32) (or even sub-micromolar (21)) extracellular concentration, this suggests that the average substrate occupancy of S4 is significantly lower than that of S1/S2.

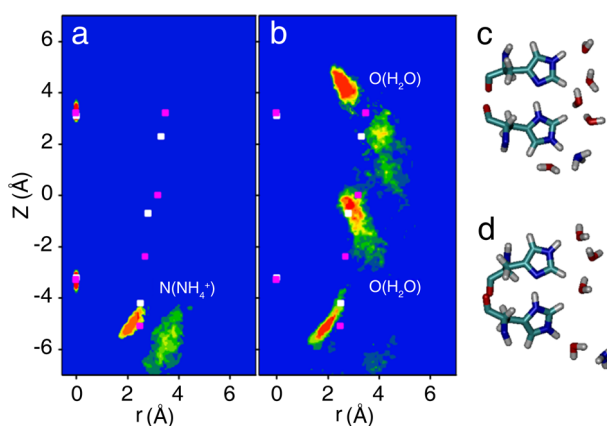


**Figure 2.5** Distribution of  $\text{NH}_3/\text{NH}_4^+$  near site S4 from 60 ps QM/MM simulations. Panel (a) shows the distribution of  $\text{NH}_3/\text{NH}_4^+$  and panel (b), the distribution of water. Positions are represented as in **Figure 2.1.c**. For reference, the density maxima from 1U7G and 1XQF crystal structures are shown as white and purple dots, respectively. Panel (c) is showing  $\text{NH}_3$  hydrogen bonding to His318 and panel (d) is showing  $\text{NH}_3$  indirectly hydrogen bonding to His318 (through water).

### 2.2.6 Coupling between $\text{NH}_3$ and $\text{H}^+$ transport

While protonation states  $\text{His168H}^+\cdots\text{His318}$  and  $\text{His168}\cdots\text{His318H}^+$  are almost equally populated when the substrate occupies site S2 (see **Figure 2.3.c**), independent QM/MM simulations show that the “His318 protonated” state becomes increasingly stable as the substrate diffuses down the pore as  $\text{NH}_3$ , from S2 to S4 (**Figure 2.11.c**). Therefore, the excess proton will likely be on His318 when the substrate reaches the lower section of the pore, in position to be re-protonated. While this suggests that the transport of  $\text{NH}_3$  and  $\text{H}^+$  is concerted, it is worth noting that any small molecule from the cytoplasm reaching S4 before  $\text{NH}_3$  (such as  $\text{HCO}_3^-$  or  $\text{HPO}_4^{2-}$ ) could take the proton without disrupting the  $\text{NH}_3:\text{H}^+$  transport stoichiometry. It is unlikely that the excess proton stored in the histidine dyad will be shuttled back to the periplasm after the departure of  $\text{NH}_3$  from S2, since here is no residue above His168 that can act as proton acceptor, and since the Phe107/Phe215 gate precludes the formation of a proton wire between S2 and S1. The transport of  $\text{NH}_3$  and  $\text{H}^+$  therefore appears to be coupled in a 1:1 stoichiometry.

### 2.2.7 Reset of His168 and His318 protonation states

Each co-transport of a proton through the His168-His318 dyad takes the system from a “His168–H $\cdots$ His318–H” state, required for substrate deprotonation in S2, to a “H–His168 $\cdots$ H–His318” state, that cannot bind NH $_4^+$  in S2 and is essentially inactive for NH $_3$ /H $^+$  co-transport. For the transport cycle to repeat, the original protonation state of the histidines has to be restored.

We have investigated a “reset” mechanism based on the formation of a transient water chain in the pore that creates a cyclic hydrogen bond network formed of two histidines and four or five water molecules between S2 and S4. Such transient conformation has been observed repeatedly in our free simulations of the “H–His168 $\cdots$ H–His318” state. Once that cyclic proton wire (or “proton loop”) is formed, two opposite reaction pathways can be imagined: 1) a “hydronium” pathway, in which the proton from N $\epsilon$  of His168 is transferred to the top water molecule in the pore, forming an unstable H $_3$ O $^+$  ion that diffuses down the water chain according to a Grotthuss-like mechanism and transfers its excess proton to N $\epsilon$  of His318; and 2) a “hydroxide” pathway, in which N $\epsilon$  of His318 gets a proton from water, generating an OH $^-$  ion that diffuses up and receives the excess proton from N $\epsilon$  of His168.

Based on gas-phase *ab initio* calculations (Figure 2.13.a-c), the “hydroxide” pathway has a much lower energy barrier than the “hydronium” pathway, and is strongly favored. The detailed mechanism was investigated using constrained QM/MM simulations with five water molecules between S2 and S4. The free energy surface along the “hydroxide” pathway (Figure 2.6.a) shows an activation energy of  $17.2 \pm 0.5$  kcal/mol and a shoulder corresponding to a OH $^-$  ion coordinated by three water molecules (Figure 2.6.c). Although four water molecules between S2 and S4 are sufficient to create a stable proton loop, the additional water molecule creates a full hydration shell around the hydroxide anion<sup>50</sup> and results in a significantly lower free energy barrier (Figure 2.13.d). Although the reaction barrier is relatively high, similar or even higher barriers have been seen in many proton transfer processes in proteins (50-52).

This “hydroxide” pathway is analogous to the “proton hole” mechanism proposed by Riccardi *et al.* (53) for a proton transfer between two imidazole moieties in solution. The “hole” is the deprotonated state of any mediating molecule (53) and, in the AmtB system, is transferred from His318 to His168



through bridging water molecules. We have also considered other resetting mechanisms but they all happen to be less likely. For instance, the His168 and His318 rings may rotate to be parallel or flip around to facilitate proton transfer. However, our calculations have shown that the rotation of the rings alone (before any proton transfer) has a free energy cost greater than 20 kcal/mol and results in no stable product state.

To directly estimate the relative free energies of the “H–His168···H–His318” and “His168–H···His318–H” states, we have used PM/MM simulations to calculate the mutation free energy from one state to the other. The resulting free energy is  $+1.7 \pm 0.8$  kcal/mol, compared to +3.5 and  $-2.6$  kcal/mol from the QM/MM simulations, depending on the specific structure of the water chain (see Figure 2.13). This confirms that the two His-His protonation states have comparable energies once the water molecules in the pore adopt their equilibrium configuration.

This reset step is likely to have slow kinetics, and is possibly the rate-determining step in the transport process. The experimental transport rate under nitrogen-limiting conditions is 10–10000 molecules per second (12), which can be converted to an overall activation energy of 12.5–16.6 kcal/mol, using Eyring’s rate theory with a pre-factor of  $1.5 \times 10^{13} \text{ s}^{-1}$  derived from our simulations of the proton transfer reaction between His168 and His318 (see section “Mechanism of  $\text{NH}_4^+$  deprotonation in S2”). The calculated barrier of  $17.2 \pm 0.5$  kcal/mol for the reset of the protonation state of His168 and His318 is slightly above that range, but considering that concerted proton transfer reactions usually show enhanced nuclear quantum effects (54,55), the effective barrier is expected to be 2–6 kcal/mol lower when zero-point energy and tunneling effect corrections are applied (56-58). The overall co-transport mechanism is therefore consistent with the experimental rate.

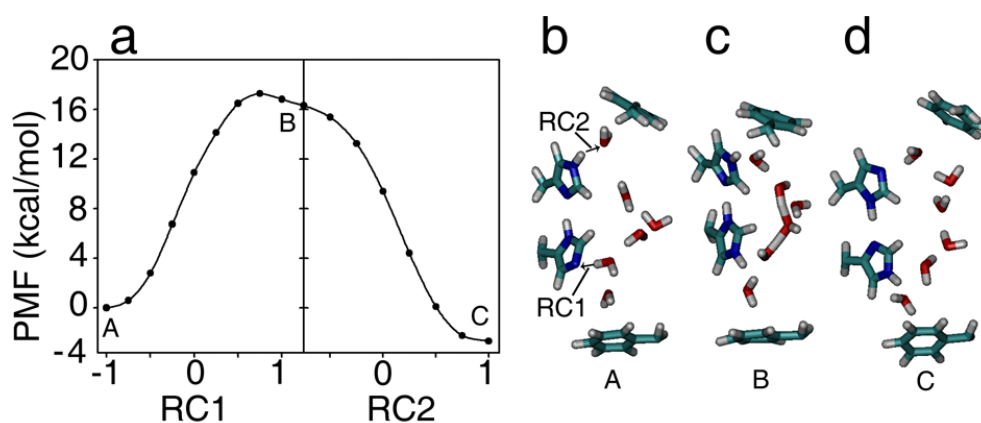


**Figure 2.6** PMFs for proton transfer between His168 and His318 through a water chain calculated from QM/MM simulations in the protein environment. Panel (a) shows the free energy profile along two reaction coordinates, which are defined as  $RC1 = d_{O(\text{water in } S4)\text{-H}} - d_{N(\text{His318})\text{-H}}$  and  $RC2 = d_{N(\text{His168})\text{-H}} - d_{O(\text{water in } S2)\text{-H}}$ . Panels (b), (c), and (d) are snapshots for reactant A, intermediate B, and product C, respectively. The reaction coordinates are illustrated in panel (b). When RC1 is scanned, RC2 is fixed at 0.75 Å, and when RC2 is scanned, RC1 is fixed at 1.25 Å. Each point corresponds to a 5-ps constrained QM/MM simulation.

### 2.3 Conclusion

We have investigated co-transport mechanisms for net ammonium ( $\text{NH}_4^+$ ) transport through AmtB using polarizable mechanics/molecular mechanics simulations, QM/MM simulations, and *ab initio* calculations. The overall mechanism is summarized in Figure 2.7.a and the free energy levels along the transport cycle are shown in Figure 2.7.b. The free energy over the whole cycle is  $-1.9$  kcal, which is an indication of the accuracy of our calculations. (In the absence of a trans-membrane potential, a perfectly-sampled simulation, performed using a consistent description of the atomic forces, would result in a strictly zero free energy difference over the cycle.) Our simulations show that site S1 provides a coordination that is highly selective for  $\text{NH}_4^+$  over  $\text{Na}^+$  and  $\text{K}^+$  ions. They also show that  $\text{NH}_4^+$  is stable in site S2, where it is involved in two cation- $\pi$  interactions (with Phe205 and Trp212) and two hydrogen bonds (with His168 and one of the water molecules in the pore). First-principles calculations show that, once  $\text{NH}_4^+$  reaches S2, the excess proton easily transfers to His168 and the complex  $\text{NH}_4^+\cdots\text{His168}\cdots\text{His318}$  forms a charge-delocalized structure in which rapid proton movement is observed. After deprotonation,  $\text{NH}_3$  diffuses through the hydrophobic pore with almost no free energy barrier. Once it reaches site S4, the Phe31-coordinated substrate accepts a proton from  $\text{His318H}^+$  (either directly or through a bridging water molecule) and diffuses into the cytoplasm as  $\text{NH}_4^+$ .

The deprotonation/diffusion/re-protonation of ammonium leaves the His168-His318 pair in a protonation state that is inactive for the next co-transport cycle. To restore the initial state, a proton needs to transfer from His168 to His318 through a chain of water molecules occupying the pore. This “histidine reset” mechanism involves a high-energy intermediate, as expected from the experimental turnover rate of AmtB, which is more in line with the rate of a conventional enzyme than of a channel. Contrary to other slow processes, such as the diffusion of  $\text{NH}_4^+$  through the pore as a whole, which is kinetically irrelevant because  $\text{NH}_4^+$  deprotonation in S2 is spontaneous, the “reset” step appears to be a kinetic bottleneck.

Because of the technical challenge of measuring slow transport events, it remains unclear whether AmtB favors the transport of  $\text{NH}_3$  or  $\text{NH}_4^+$  (9). Mutants F107A, W148A, and S219A are all more active than the wild-type protein (9). Even the triple mutant F107A/W148A/S219A, for which all residues coordinating

the substrate in S1 are displaced, is slightly more active than the wild type (9). This clearly shows that S1 is not essential for the activity. According to most propositions for a neutral ( $\text{NH}_3$ ) permeation mechanism, site S1 is important for the recruitment and deprotonation of  $\text{NH}_4^+$ . None of these functions are likely to play out the same in the triple mutant. Furthermore, mutagenesis studies show that all residues surrounding site S2 are important for the activity (10). Mutants of F215, W212, and H168 are mostly inactive, with the exception of W212F and H168E. Both of these active mutants are still functional in the  $\text{NH}_3/\text{H}^+$  co-transport mechanism we are proposing.

The electrogenic mechanism presented here does not exclude that electroneutral transport might also take place. However, it illustrates the most plausible pathway for the transport of the charged  $\text{NH}_4^+$  in the Amt/MEP family of proteins, and highlights the role of the two histidines lining the pore. Our calculations also show that a glutamic acid residue in position 168 could play the same role, suggesting that *Saccharomyces cerevisiae*'s Mep1 and Mep2 (48) (in which His168 is replaced by Glu) may also exploit this mechanism.

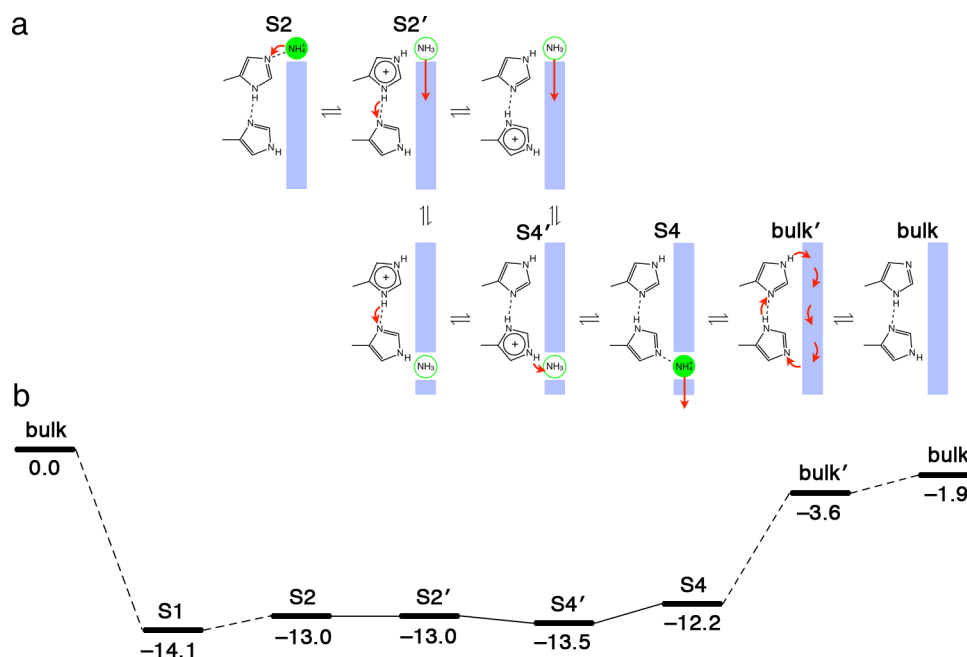


**Figure 2.7** Schematic illustration of the  $\text{NH}_3/\text{H}^+$  co-transport cycle. Panel (a) shows the scheme of the transport mechanism. Each state is labelled according to the positions of  $\text{NH}_4^+/\text{NH}_3$  in the pore.  $\text{NH}_4^+$  in site S2 transfers its excess proton to the His168-His318 dyad. After deprotonation,  $\text{NH}_3$  can diffuse down the pore into S4 binding site, where it can receive the excess proton from His318. Once  $\text{NH}_4^+$  moves out of the pore (state bulk'), the protonation state of the His168-His318 dyad is reset by a concerted proton transfer through a water chain in the pore. Areas in blue represent water-accessible regions. Curved red arrows represent proton transfer and straight red arrows represent substrate diffusion. Panel (b) shows the free energies (in kcal/mol) of the most important structures in the transport process. The first and the last state are the same in the thermodynamic cycle. The difference in their energy levels is due to the computation errors throughout the process.

## 2. 4 Experimental Details

### 2.4.1 Simulation System Preparation

The AmtB monomer structure used in this work is based on the X-ray structure determined by Khademi *et al* (11). (Protein Data Bank ID: 1U7G). Three mutated residues (F68S, S126P, and K255L) in 1U7G are modified back to their native states. Both His168 and His318 are neutral. We use the “His168–H··His318–H” protonation state for the initial structure, based on our previous simulation study (30) showing that this state reproduces the experimental density (12) inside the pore much more accurately than the reverse “H–His168··H–His318” state. The Membrane Builder tool of CHARMM-GUI (51) is then used to add a lipid bilayer and a water box with dimensions of 92.3 Å × 77.4 Å × 91.2 Å around the monomer. Specifically, 185 dimyristoylphosphatidylcholine (DMPC) molecules (94 on the periplasmic side and 91 on the cytoplasmic side) and 13111 TIP3P water molecules (51) are added, and the system is neutralized by adding 34 K<sup>+</sup> and 36 Cl<sup>-</sup> ions, corresponding to 0.1 M salt concentration. All simulations are equilibrated for at least 200 ps before data collection.

### 2.4.2 Molecular Dynamic (MD) Simulations

MD simulations are performed with the CHARMM program (52), using a hybrid polarizable mechanics/molecular mechanics (PM/MM) description of the system. NH<sub>4</sub><sup>+</sup> and surrounding water molecules and protein side chains are described by a polarizable force field based on the classical Drude oscillator (53-56), and parameterized to reproduce both the free energy of hydration and the ion-protein interactions. The rest of the system is described by the non-polarizable CHARMM param27 force field (57). See Appendix and Figure 2.10 for details.

### 2.4.3 Binding Free Energy Calculations

Relative binding free energies ( $\Delta\Delta G_{\text{bind}}$ ) are calculated using the standard thermodynamic integration method (58), as combinations of free energies of mutation of NH<sub>4</sub><sup>+</sup> to H<sub>2</sub>O at S1, S2, S4, and in bulk water. Mutations are performed using a hybrid residue that corresponds to the NH<sub>4</sub><sup>+</sup> polarizable model when  $\lambda = 0$  and to the SWM4 water model when  $\lambda = 1$  (see Figure 2.10.d). The transition of  $\lambda$  from 0 to 1 is split into 12 windows: 0, 0.05, 0.15, 0.25, 0.35, 0.45,

0.55, 0.65, 0.75, 0.85, 0.95, and 1. Each window corresponds to an independent simulation that includes 100 ps of equilibration and 100 ps of data collection. Five independent calculations are performed in order to get more reliable results and to estimate errors. The free energy calculations in the protein ( $\Delta G_{mut}^{prot}$ ) use polarizable force fields as described in the previous section. Free energies of hydration ( $\Delta G_{mut}^{wat}$ ) are calculated in a periodic system of 2000 SWM4 water molecules. The solvent box is large enough that the resulting solvation free energies show no system-size dependency. Since the system is periodic, the free energies do not contain a contribution from the air-water interface (68).

#### 2.4.4 Quantum Mechanics/Molecular Mechanics (QM/MM) Simulations

QM/MM simulations are performed using the CP2K program (59). The details of the CP2K setup can be found in SI. All initial structures used in QM/MM simulations are equilibrated by PM/MM simulations for at least 1 ns. The QM region includes  $\text{NH}_4^+$ , the surrounding side chains, and water molecules in the hydrophobic pore. The QM box is approximately  $14 \text{ \AA} \times 18 \text{ \AA} \times 22 \text{ \AA}$ , 6 to 8  $\text{\AA}$  larger than the extent of the QM fragments in each direction.

#### 2.4.5 Constrained QM/MM Simulations

Potentials of mean force (PMFs) of proton transfer reactions are calculated using constrained QM/MM molecular dynamics simulations. The reaction coordinate for a proton transfer,  $X$ , is defined as the difference in distances from the proton to the two heavy atoms involved in the hydrogen bond. The range of  $X$  is divided into nine windows ( $-1, -0.75, -0.5, -0.25, 0, 0.25, 0.5, 0.75, \text{ and } 1 \text{ \AA}$ ) and individual QM/MM simulations are performed for each window with  $X$  fixed using a Lagrange multiplier. The constraint forces are collected and then integrated over the full range of  $X$  to generate the PMF.

#### 2.4.6 Adaptive biasing force (ABF) simulations

PMFs for  $\text{NH}_3$  permeation in the hydrophobic pore are calculated using the ABF method (60-63), implemented in the NAMD program (64). CHARMM param27 force field (57) is used for all residues and water, and OPLS model (65) is used for  $\text{NH}_3$ . Two PMFs are calculated: one with charged His168 and neutral

His318 and the other with neutral His168 and charged His318. The reaction coordinate is the  $Z$ -coordinate offset of  $\text{NH}_3$  from the center of the phenyl ring of Phe107.  $\text{NH}_3$  is forced to move within the range  $\text{RC} = 4.5$  to  $17.0 \text{ \AA}$ . For each PMF, the system is equilibrated for 1 ns and data is collected for 30 ns.



## 2. 5 References

1. Ninnemann O, Jauniaux JC, Frommer WB. Identification of a high affinity NH<sub>4</sub><sup>+</sup> transporter from plants. *EMBO J* 1994, Aug 1;13(15):3464-71."
2. Siewe RM, Weil B, Burkovski A, Eikmanns BJ, Eikmanns M, Krämer R. Functional and genetic characterization of the (methyl)ammonium uptake carrier of *Corynebacterium glutamicum*. *J Biol Chem* 1996, Mar 8;271(10):5398-403.
3. Marini AM, Matassi G, Raynal V, André B, Cartron JP, Chérif-Zahar B. The human rhesus-associated rhag protein and a kidney homologue promote ammonium transport in yeast. *Nat Genet* 2000;26(3):341-4.
4. Marini AM, Urrestarazu A, Beauwens R, André B. The rh (rhesus) blood group polypeptides are related to NH<sub>4</sub><sup>+</sup> transporters. *Trends Biochem Sci* 1997, Dec;22(12):460-1.
5. Marini AM, Soussi-Boudekou S, Vissers S, Andre B. A family of ammonium transporters in *Saccharomyces cerevisiae*. *Mol Cell Biol* 1997, Aug;17(8):4282-93.
6. Marini AM, Vissers S, Urrestarazu A, André B. Cloning and expression of the MEP1 gene encoding an ammonium transporter in *Saccharomyces cerevisiae*. *EMBO J* 1994, Aug 1;13(15):3456-63.
7. Conroy MJ, Durand A, Lupo D, Li XD, Bullough PA, Winkler FK, Merrick M. The crystal structure of the *Escherichia coli* AmtB-GlnK complex reveals how GlnK regulates the ammonia channel. *Proc Natl Acad Sci U S A* 2007, Jan 23;104(4):1213-8.
8. Gruswitz F, O'Connell J, Stroud RM. Inhibitory complex of the transmembrane ammonia channel, AmtB, and the cytosolic regulatory protein, GlnK, at 1.96 Å. *Proc Natl Acad Sci U S A* 2007, Jan 2;104(1):42-7.
9. Javelle A, Lupo D, Ripoche P, Fulford T, Merrick M, Winkler FK. Substrate binding, deprotonation, and selectivity at the periplasmic entrance of the *Escherichia coli* ammonia channel AmtB. *Proc Natl Acad Sci U S A* 2008, Apr 1;105(13):5040-5.
10. Javelle A, Lupo D, Zheng L, Li XD, Winkler FK, Merrick M. An unusual twin-his arrangement in the pore of ammonia channels is essential for substrate conductance. *J Biol Chem* 2006, Dec 22;281(51):39492-8.

11. Khademi S, O'Connell J, Remis J, Robles-Colmenares Y, Miercke LJ, Stroud RM. Mechanism of ammonia transport by amt/MEP/rh: Structure of amtB at 1.35 Å. *Science* 2004, Sep 10;305(5690):1587-94.
12. Zheng L, Kostrewa D, Bernèche S, Winkler FK, Li XD. The mechanism of ammonia transport based on the crystal structure of amtB of *Escherichia coli*. *Proc Natl Acad Sci U S A* 2004, Dec 7;101(49):17090-5.
13. Bostick DL, Brooks CL. Deprotonation by dehydration: The origin of ammonium sensing in the amtB channel. *PLoS Comput Biol* 2007, Feb 9;3(2):e22.
14. Ishikita H, Knapp EW. Protonation states of ammonia/ammonium in the hydrophobic pore of ammonia transporter protein amtB. *J Am Chem Soc* 2007, Feb 7;129(5):1210-5.
15. Lin Y, Cao Z, Mo Y. Molecular dynamics simulations on the *Escherichia coli* ammonia channel protein amtB: Mechanism of ammonia/ammonium transport. *J Am Chem Soc* 2006, Aug 23;128(33):10876-84.
16. Luzhkov VB, Almlöf M, Nervall M, Aqvist J. Computational study of the binding affinity and selectivity of the bacterial ammonium transporter amtB. *Biochemistry* 2006, Sep 12;45(36):10807-14.
17. Nygaard TP, Alfonso-Prieto M, Peters GH, Jensen MØ, Rovira C. Substrate recognition in the *Escherichia coli* ammonia channel amtB: A QM/MM investigation. *J Phys Chem B* 2010, Sep 16;114(36):11859-65.
18. Nygaard TP, Rovira C, Peters GH, Jensen MØ. Ammonium recruitment and ammonia transport by *E. coli* ammonia channel amtB. *Biophys J* 2006, Dec 15;91(12):4401-12.
19. Akgun U, Khademi S. Periplasmic vestibule plays an important role for solute recruitment, selectivity, and gating in the rh/amt/MEP superfamily. *Proc Natl Acad Sci U S A* 2011, Mar 8;108(10):3970-5.
20. Soupene E, Lee H, Kustu S. Ammonium/methylammonium transport (amt) proteins facilitate diffusion of NH<sub>3</sub> bidirectionally. *Proc Natl Acad Sci U S A* 2002, Mar 19;99(6):3926-31.
21. Soupene E, He L, Yan D, Kustu S. Ammonia acquisition in enteric bacteria: Physiological role of the ammonium/methylammonium transport B (amtB) protein. *Proc Natl Acad Sci U S A* 1998, Jun 9;95(12):7030-4.

22. Boeckstaens M, André B, Marini AM. Distinct transport mechanisms in yeast ammonium transport/sensor proteins of the mep/amt/rh family and impact on filamentation. *J Biol Chem* 2008, Aug 1;283(31):21362-70.
23. Ludewig U. Ion transport versus gas conduction: Function of AMT/rh-type proteins. *Transfus Clin Biol* 2006;13(1-2):111-6.
24. Fong RN, Kim KS, Yoshihara C, Inwood WB, Kustu S. The W148L substitution in the escherichia coli ammonium channel amtB increases flux and indicates that the substrate is an ion. *Proc Natl Acad Sci U S A* 2007, Nov 20;104(47):18706-11.
25. Ludewig U, von Wirén N, Frommer WB. Uniport of NH<sub>4</sub><sup>+</sup> by the root hair plasma membrane ammonium transporter leamt1;1. *J Biol Chem* 2002, Apr 19;277(16):13548-55.
26. Cao Z, Mo Y, Thiel W. Deprotonation mechanism of NH<sub>4</sub><sup>+</sup> in the escherichia coli ammonium transporter amtB: Insight from QM and QM/MM calculations. *Angew Chem Int Ed Engl* 2007;46(36):6811-5.
27. Lin Y, Cao Z, Mo Y. Functional role of asp160 and the deprotonation mechanism of ammonium in the escherichia coli ammonia channel protein amtB. *J Phys Chem B* 2009, Apr 9;113(14):4922-9.
28. Yang H, Xu Y, Zhu W, Chen K, Jiang H. Detailed mechanism for amtB conducting NH<sub>4</sub><sup>+</sup>/NH<sub>3</sub>: Molecular dynamics simulations. *Biophys J* 2007, Feb 1;92(3):877-85.
29. Lamoureux G, Javelle A, Baday S, Wang S, Bernèche S. Transport mechanisms in the ammonium transporter family. *Transfus Clin Biol* 2010, Jul 29;17(3):168-75.
30. Lamoureux G, Klein ML, Bernèche S. A stable water chain in the hydrophobic pore of the amtB ammonium transporter. *Biophys J* 2007, May 1;92(9):L82-4.
31. Straatsma TP, McCammon JA. Computational alchemy. *Annual Review of Physical Chemistry* 1992;43(1):407-35.
32. Javelle A, Severi E, Thornton J, Merrick M. Ammonium sensing in escherichia coli. Role of the ammonium transporter amtB and amtB-glnK complex formation. *J Biol Chem* 2004, Mar 5;279(10):8530-8.

33. Ahn KH, Ku HY, Kim Y, Kim SG, Kim YK, Son HS, Ku JK. Fluorescence sensing of ammonium and organoammonium ions with tripodal oxazoline receptors. *Org Lett* 2003, May 1;5(9):1419-22.
34. Chipot C, Maigret B, Pearlman DA, Kollman PA. Molecular dynamics potential of mean force calculations: A study of the toluene-ammonium  $\pi$ -cation interactions. *J Am Chem Soc* 1996;118(12):2998-3005.
35. Gallivan JP, Dougherty DA. A computational study of cation- $\pi$  interactions vs salt bridges in aqueous media: Implications for protein engineering. *J Am Chem Soc* 2000;122(5):870-4.
36. Sa R, Zhu W, Shen J, Gong Z, Cheng J, Chen K, Jiang H. How does ammonium dynamically interact with benzene in aqueous media? A first principle study using the car-parrinello molecular dynamics method. *J Phys Chem B* 2006, Mar 16;110(10):5094-8.
37. Bakouh N, Benjelloun F, Hulin P, Brouillard F, Edelman A, Chérif-Zahar B, Planelles G. NH<sub>3</sub> is involved in the NH<sub>4</sub><sup>+</sup> transport induced by the functional expression of the human rh C glycoprotein. *J Biol Chem* 2004, Apr 16;279(16):15975-83.
38. Roux B, Bernèche S. On the potential functions used in molecular dynamics simulations of ion channels. *Biophys J* 2002, Mar;82(3):1681-4.
39. Hall JA, Kustu S. The pivotal twin histidines and aromatic triad of the escherichia coli ammonium channel amtB can be replaced. *Proc Natl Acad Sci U S A* 2011, Aug 9;108(32):13270-4.
40. Berezhkovskii A, Hummer G. Single-file transport of water molecules through a carbon nanotube. *Phys Rev Lett* 2002;89(6):64503.
41. Chen H, Ilan B, Wu Y, Zhu F, Schulten K, Voth GA. Charge delocalization in proton channels, I: The aquaporin channels and proton blockage. *Biophys J* 2007, Jan 1;92(1):46-60.
42. Hummer G, Rasaiah JC, Noworyta JP. Water conduction through the hydrophobic channel of a carbon nanotube. *Nature* 2001, Nov 8;414(6860):188-90.
43. Lee YS, Krauss M. Dynamics of proton transfer in bacteriorhodopsin. *J Am Chem Soc* 2004, Feb 25;126(7):2225-30.

44. Liang C, Jansen TL, Knoester J. Proton transport in biological systems can be probed by two-dimensional infrared spectroscopy. *J Chem Phys* 2011, Jan 28;134(4):044502.
45. Manca C, Tanner C, Leutwyler S. Excited state hydrogen atom transfer in ammonia-wire and water-wire clusters. *International Reviews in Physical Chemistry* 2005;24(3-4):457-88.
46. Tanner C, Thut M, Steinlin A, Manca C, Leutwyler S. Excited-state hydrogen-atom transfer along solvent wires: Water molecules stop the transfer. *J Phys Chem A* 2006, Feb 9;110(5):1758-66.
47. Hunter EP, Lias SG. Evaluated gas phase basicities and proton affinities of molecules: An update. *Journal of Physical and Chemical Reference Data* 1998;27:413.
48. Marini AM, Boeckstaens M, Benjelloun F, Chérif-Zahar B, André B. Structural involvement in substrate recognition of an essential aspartate residue conserved in mep/amt and rh-type ammonium transporters. *Curr Genet* 2006, Jun;49(6):364-74.
49. Robertson WH, Diken EG, Price EA, Shin JW, Johnson MA. Spectroscopic determination of the OH<sup>-</sup> solvation shell in the OH<sup>-</sup>·(H<sub>2</sub>O)<sub>n</sub> clusters. *Science* 2003, Feb 28;299(5611):1367-72.
50. Elsässer B, Fels G. Atomistic details of the associative phosphodiester cleavage in human ribonuclease H. *Phys Chem Chem Phys* 2010, Sep 28;12(36):11081-8.
51. Martín-García F, Mendieta-Moreno JI, López-Viñas E, Gómez-Puertas P, Mendieta J. The role of gln61 in hras GTP hydrolysis: A quantum mechanics/molecular mechanics study. *Biophys J* 2012, Jan 4;102(1):152-7.
52. Mujika JI, Lopez X, Mulholland AJ. Mechanism of c-terminal intein cleavage in protein splicing from QM/MM molecular dynamics simulations. *Org Biomol Chem* 2012, Feb 14;10(6):1207-18.
53. Riccardi D, König P, Prat-Resina X, Yu H, Elstner M, Frauenheim T, Cui Q. "Proton holes" in long-range proton transfer reactions in solution and enzymes: A theoretical analysis. *J Am Chem Soc* 2006, Dec 20;128(50):16302-11.
54. Limbach H-H, Klein O, Lopez Del Amo JM, Elguero J. Kinetic hydrogen/deuterium isotope effects in multiple proton transfer reactions.

Zeitschrift Für Physikalische Chemie/International Journal of Research in Physical Chemistry and Chemical Physics 2004;218(1/2004):17-50.

55. Smedarchina Z, Siebrand W, Fernández-Ramos A, Cui Q. Kinetic isotope effects for concerted multiple proton transfer: A direct dynamics study of an active-site model of carbonic anhydrase II. *J Am Chem Soc* 2003, Jan 8;125(1):243-51.

56. Alhambra C, Corchado JC, Sánchez ML, Gao J, Truhlar DG. Quantum dynamics of hydride transfer in enzyme catalysis. *J Am Chem Soc* 2000;122(34):8197-203.

57. Alhambra C, Luz Sánchez M, Corchado J, Gao J, Truhlar DG. Quantum mechanical tunneling in methylamine dehydrogenase. *Chem Phys Lett* 2001;347(4):512-8.

58. Cui Q, Karplus M. Is a “proton wire” concerted or stepwise? A model study of proton transfer in carbonic anhydrase. *The Journal of Physical Chemistry B* 2003;107(4):1071-8.

59. Jo S, Kim T, Iyer VG, Im W. CHARMM-GUI: A web-based graphical user interface for CHARMM. *J Comput Chem* 2008, Aug;29(11):1859-65.

60. Jorgensen WL, Chandrasekhar J, Madura JD, Impey RW, Klein ML. Comparison of simple potential functions for simulating liquid water. *J Chem Phys* 1983;79:926.

61. Brooks BR, Brooks CL, Mackerell AD, Nilsson L, Petrella RJ, Roux B, et al. CHARMM: The biomolecular simulation program. *J Comput Chem* 2009, Jul 30;30(10):1545-614.

62. Lamoureux G, Harder E, Vorobyov IV, Roux B, MacKerell AD. A polarizable model of water for molecular dynamics simulations of biomolecules. *Chem Phys Lett* 2006;418(1):245-9.

63. Lamoureux G, MacKerell Jr AD, Roux B. A simple polarizable model of water based on classical drude oscillators. *J Chem Phys* 2003;119:5185.

64. Lopes PE, Roux B, MacKerell AD. Molecular modeling and dynamics studies with explicit inclusion of electronic polarizability: Theory and applications. *Theoretical Chemistry Accounts: Theory, Computation, and Modeling (Theoretica Chimica Acta)* 2009;124(1):11-28.

65. Orabi EA, Lamoureux G. Cation-  $\pi$  and  $\pi$ - $\pi$  interactions in aqueous solution studied using polarizable potential models. *J Chem Theory Comput* 2011;8(1):182-93.
66. MacKerell Jr AD, Bashford D, Bellott M, Dunbrack Jr RL, Evanseck JD, Field MJ, et al. All-atom empirical potential for molecular modeling and dynamics studies of proteins. *The Journal of Physical Chemistry B* 1998;102(18):3586-616.
67. Kollman P. Free energy calculations: Applications to chemical and biochemical phenomena. *Chem Rev* 1993;93(7):2395-417.
68. Lamoureux G, Roux B. Absolute hydration free energy scale for alkali and halide ions established from simulations with a polarizable force field. *J Phys Chem B* 2006, Feb 23;110(7):3308-22.
69. Laino T, Mohamed F, Laio A, Parrinello M. An efficient real space multigrid QM/MM electrostatic coupling. *J Chem Theory Comput* 2005;1(6):1176-84.
70. Darve E, Pohorille A. Calculating free energies using average force. *J Chem Phys* 2001;115:9169.
71. Darve E, Rodríguez-Gómez D, Pohorille A. Adaptive biasing force method for scalar and vector free energy calculations. *J Chem Phys* 2008, Apr 14;128(14):144120.
72. Hénin J, Chipot C. Overcoming free energy barriers using unconstrained molecular dynamics simulations. *J Chem Phys* 2004, Aug 15;121(7):2904-14.
73. Hénin J, Fiorin G, Chipot C, Klein ML. Exploring multidimensional free energy landscapes using time-dependent biases on collective variables. *J Chem Theory Comput* 2009;6(1):35-47.
74. Phillips JC, Braun R, Wang W, Gumbart J, Tajkhorshid E, Villa E, et al. Scalable molecular dynamics with NAMD. *J Comput Chem* 2005, Dec;26(16):1781-802.
75. Gao J, Xia X, George TF. Importance of bimolecular interactions in developing empirical potential functions for liquid ammonia. *The Journal of Physical Chemistry* 1993;97(36):9241-7.
76. Flyvbjerg H, Petersen HG. Error estimates on averages of correlated data. *J Chem Phys* 1989;91:461.

77. Ben-Naim A, Marcus Y. Solvation thermodynamics of nonionic solutes. *J Chem Phys* 1984;81:2016.

78. Marcus Y. Thermodynamics of solvation of ions. Part 5.—Gibbs free energy of hydration at 298.15 K. *Journal of the Chemical Society, Faraday Transactions* 1991;87(18):2995-9.

79. Yu H, Whitfield TW, Harder E, Lamoureux G, Vorobyov I, Anisimov VM, et al. Simulating monovalent and divalent ions in aqueous solution using a drude polarizable force field. *J Chem Theory Comput* 2010;6(3):774-86.



## 2. 6 Appendix

### 2.6.1 Parameterization of polarizable force field

#### 2.6.1.1 Method

Polarizable models based on the classical Drude oscillator have been developed for water (1,2), aromatic compounds (3,4), amides (5), alcohols (6), and ions (7,8). We are extending these models to describe the interaction of some of these compounds with  $\text{Na}^+$ ,  $\text{K}^+$ , and  $\text{NH}_4^+$  [see Figure 2.8.a]. Polarizable models for the interaction of  $\text{Na}^+$ ,  $\text{K}^+$ , and  $\text{NH}_4^+$  with water have been reported previously (7). Optimization of the force field follows the procedure reported previously (7). It is based on adjusting pair-specific Lennard-Jones (LJ) parameters between atoms of ions ( $\text{Na}^+$ ,  $\text{K}^+$ , and  $\text{NH}_4^+$ ) and a few atoms of the interacting compounds, in order to reproduce the ab initio complexation energies.

Atoms selected for parameterization are those directly involved in the complexation and, if necessary, the nearby carbon. A non-atomic site (X) described in our previous study (7) is found necessary to model the interactions of  $\text{Na}^+$  and  $\text{NH}_4^+$  with toluene. Similar sites are also required to model the interaction of the three ions with phenol and the interaction of  $\text{NH}_4^+$  with indole and 3-methylindole. The non-atomic sites X are massless particles at the center of the six-membered ring with no electric charge and no LJ parameters other than the pair-specific LJ parameters with ions.

Pair-specific LJ parameters between the ions and atoms of the ligands are adjusted to reproduce the ab initio interaction energies. To simplify the optimization process, the pair-specific LJ parameters between different pairs of interacting atoms are set equal in some complexes (see Table 2.2 and Table 2.3). Optimization is first performed on the interactions of the ions with the “un-methylated” compounds, and the transferability of the optimized parameters to methylated compounds is then tested. Although the “un-methylated” parameters perform generally well, they are further adjusted to model ab initio results more closely. Numerical optimization of the pair-specific LJ parameters is performed following our previously reported protocol (7).

#### 2.6.1.2 Geometry optimization

Full geometry optimizations of the complexes between these ligands and the three cations  $\text{Na}^+$ ,  $\text{K}^+$ , and  $\text{NH}_4^+$  are performed at the MP2(FC)/6-311++G(d,p) level using Gaussian 09 program (9). Geometry optimization is performed without imposing any symmetry constraints, except for complexes of  $\text{NH}_4^+$  with imidazole and 4-methylimidazole, which are optimized constraining the ammonium NH bonds at their gas-phase values. This constraint is applied in order to avoid the transfer of the proton from  $\text{NH}_4^+$  to N1 of imidazole or 4-methylimidazole. The interaction energies are corrected for basis set superposition error (BSSE) using the Boys and Bernardi counterpoise technique (10). Potential energy surfaces (PESs) are computed at the same level of theory and all interaction energies are corrected for BSSE. The surfaces are computed with rigid monomers in their gas-phase optimized geometries, by scanning the intermolecular distances between the ions and ligands.

Table S1 lists the BSSE-corrected and uncorrected interaction energies in all optimized complexes as well as the interaction energies obtained from the optimized polarizable potential models.

Geometry optimization of  $\text{Na}^+$ ,  $\text{K}^+$ , and  $\text{NH}_4^+$  complexes with the 9 studied compounds is performed starting from different plausible conformations. The optimized geometries of the complexes are reported in Figure 2.8.b for  $\text{Na}^+$  and  $\text{K}^+$  and in Figure 2.8.c for  $\text{NH}_4^+$ . Ions bind preferably to electronegative oxygen and nitrogen atoms, but are involved in strong cation- $\pi$  interactions as well (see structures c, d2, e2, f, and g of Figure 2.9 and Figure 2.10).

Only one minimum energy conformer is observed for ethanol, NMA, and toluene complexes with the three cations (see Figure 2.9 **a**, **b**, **c** and Figure 2.10 **a**, **b**, **c**). Two minimum energy conformers are found in the interaction of the cations with phenol and p-methylphenol, with cations interacting either with O atom (Figure 2.9 **d1**, **e1** and S3 **d1**, **e1**) or with the  $\pi$  cloud (Figure 2.9 **d2**, **e2** and S3 **d2**, **e2**). As seen in conformers **d1** and **e1** in both figures, the interaction of the ions with O results in bending of the phenolic hydrogen out of the ring plane, in the opposite direction of the cation. Table S1 shows that interaction of the ions with O results in a more stable conformer compared to interaction with the  $\pi$  cloud, in agreement with previous computational study (11). Only one minimum energy conformer is found in the interaction of the cations with indole (Figure 2.9 **f** and Figure 2.10 **f**) and 3-methylindole (Figure 2.9 **g** and Figure 2.10 **g**), with the

cation centered on top of the six membered ring, in agreement with previously reported *ab initio* results (12). The interaction of the cations with imidazole (Figure 2.9 **h** and Figure 2.10 **h**) and 4-methylimidazole (Figure 2.9 **i** and Figure 2.10 **i**) gives one stable conformer in which the cation interacts with N1 rather than the  $\pi$  cloud, in accord with previous calculations (12).

Free optimization of  $\text{NH}_4^+$  in complex with imidazole or 4-methylimidazole results in spontaneous proton transfer from the ion to the ligand. Complexes **h** and **i** in Figure 2.8.c are therefore obtained by constraining the NH bonds of  $\text{NH}_4^+$  to the gas-phase optimized length (1.024 Å). Though proton transfer occurs readily in the gas phase, such transfer does not occur in aqueous solutions. For example no proton transfer is observed in a free optimization of the complex in which  $\text{NH}_4^+$  is hydrogen bonded to imidazole and three water molecules [Figure 2.8.c **j**]. The constrained optimizations aim to optimize potential models for  $\text{NH}_4^+$  interactions with the two ligands.

In all  $\text{NH}_4^+ - \pi$  complexes [Figure 2.8.c **c**, **d2**, **e2**, **f**, and **g**],  $\text{NH}_4^+$  is oriented such that N is on top of the center of the six-membered ring (X) with an  $\text{X} \cdots \text{N}-\text{H}$  angle in the range 26–37°. This is in agreement with our previous results for the  $\text{NH}_4^+$ -benzene complex (7), where the global minimum conformer is found between the unidentate and bidentate conformers.

### 2.6.2 Potential energy surfaces

*Ab initio* calculated PESs for  $\text{Na}^+$ ,  $\text{K}^+$ , and  $\text{NH}_4^+$  in complex with all studied compounds are reported in Figure 2.8.b (dashed lines). Curves **(a)** and **(b)** are calculated by scanning the distance between the center of mass (CM) of the ion and O of ethanol and NMA, respectively. Curves **(c)**, **(d)**, **(f)**, **(h)**, and **(i)** are calculated by scanning the distance between the CM of the ion and the center of the six-membered ring in toluene, phenol, p-methylphenol, indole, and 3-methylindole, respectively, with  $\text{NH}_4^+$  being oriented in a unidentate conformation. Curves **(e)** and **(g)** are calculated for the complexes of the ions with phenol and p-methylphenol, in which the geometry of the complex corresponds to the global

minimum conformers and the scan involved the distance between CM of the ion and the O atom. PESs for the cations in complex with imidazole, (**j**), and 4-methylimidazole, (**k**), are calculated by the scan of the distance between the CM of the ion and N1 in the interacting ligand.

### 2.6.3 Optimized force field

Table 2.3 and Table 2.4 summarize the optimized pair-specific LJ parameters of the polarizable models. Parameters for  $\text{NH}_4^+$ -toluene complex are those previously optimized for benzene- $\text{NH}_4^+$  interaction (7). The optimized parameters for  $\text{NH}_4^+$ -benzene interaction are found transferable to  $\text{NH}_4^+$ -toluene complex and no further adjustment is required. Figure S4 shows the excellent agreement between the PESs calculated using the optimized models (solid lines) and those from the MP2(FC)/6-311++G(d,p) calculations (dashed lines), especially near the equilibrium intermolecular distances. Table 2.2 lists the complexation energies of the global minimum conformers obtained using the optimized models ( $E^{\text{MM}}$ ) which are in close agreement with the ab initio BSSE-corrected ( $E^{\text{CP}}$ ) complexation energies. The slight underestimation of the complexation energy of cations with phenol and p-methylphenol (see Table 2.2) is due to the original force field not reproducing the bending of the phenolic hydrogen observed in the ab initio calculations.

We also examined the transferability of the optimized model for  $\text{NH}_4^+$ -imidazole to the complex of the ion with imidazole and three water molecules. The model gives  $-23.64$  kcal/mol for the complexation energy of  $\text{NH}_4^+(\text{H}_2\text{O})_3$  with imidazole, in good agreement with  $-21.89$  kcal/mol from the MP2(FC)/6-311++G(d,p) calculations.

### 2.6.4 AmtB simulation system

The simulation system is shown in Figure 2.10.a For molecular dynamics (MD) simulations of  $\text{Na}^+$ ,  $\text{K}^+$ , or  $\text{NH}_4^+$  in the periplasmic binding site S1, the side chains of amino acids Phe103, Phe107, Trp148, Phe215, and Ser219, as well as two water molecules near the ion, are represented by the polarizable force field, as shown in Figure 2.10.b. For simulations of  $\text{NH}_4^+$  in site S2, the side chains of amino acids Phe107, His168, Trp212, Phe215, His318, and four water molecules that have entered the pore from the cytoplasmic site are made polarizable, as

shown in Figure 2.10.c. These residues are selected because they are the nearest neighbors to the ions in the binding sites. Both Phe107 and Phe215 are treated with polarizable models because their side chains form a parallel displaced arrangement that results in additional stabilization due to the cooperation between cation- $\pi$  and  $\pi$ - $\pi$  interactions (7,13).

Parameters of the polarizable amino acids side chains are taken from the studied model compound (3-6):  $-\text{CH}_2\text{-OH}$  from ethanol for Ser219;  $-\text{CH}_2\text{-C}_6\text{H}_5$  from toluene for Phe103, Phe107, and Phe215;  $-\text{CH}_2\text{-C}_8\text{H}_6\text{N}$  from 3-methylindole for Trp148 and Trp212; and  $-\text{CH}_2\text{-C}_3\text{H}_3\text{N}_2$  from 4-methylimidazole for His168 and His318. Those polarizable fragments are linked to the  $\alpha$  carbons of the corresponding residues. To keep the fragment electrically neutral, the charge on the H atom removed from the model compound is transferred to the carbon atom. All bonded parameters between polarizable and non-polarizable atoms are taken from CHARMM param27 parameters (14).

While the interaction of the ions with neighboring amino acid side chains are described by the polarizable force field, CHARMM param27 parameters (along with the TIP3P water model (15)) are used for other interactions. Because the Drude oscillator model is based on point charges, the electrostatic interactions between the polarizable and non-polarizable fragments are described in a transparent way, as charge-charge interactions.

### 2.6.5 Free energy calculations

To maintain a constant number of interaction sites throughout the alchemical transformation, special hybrid residues are used [Figure 2.10.d]As described in our previous studies (7), these residues are created by bonding one fragment representing the first ion with a second “dummy” fragment representing the second ion. A force constant of  $5 \text{ kcal/mol/\text{\AA}^2}$  is assigned to the tether between the two fragments. The ligand mutation involves a linear variation of the non-bonded parameters.

A weak restraint potential is imposed on the ion to prevent large drifts away from the binding site and to allow for reliable estimation of relative binding free energies. The 1U7G crystal structure (16) of AmtB is showing the center of mass (CM) of  $\text{NH}_4^+$  in site S1 at distances of 2.50 and 2.84  $\text{\AA}$  from oxygen atoms of the nearest two water molecules, at distance 3.46  $\text{\AA}$  from atom CE2 of Phe107, and at

distance 3.82 Å from atom CE2 of Trp148 (atom CE2 in Phe107 corresponds to C3 or C5 in toluene, while it corresponds to C9 in 3-methylindole). We thus apply a potential of 5 kcal/mol/Å<sup>2</sup> at distances higher than 3.0 Å between the CM of the ion (Na<sup>+</sup>, K<sup>+</sup>, or NH<sub>4</sub><sup>+</sup>) and the oxygen atoms of the two polarizable water molecules. A similar potential is applied at distances larger than 4.5 Å between the CM of the ion and atom CE2 of Phe107 or Trp148. Ammonium in site S2 of the 1U7G structure is 3.44 Å away from atom NE2 of His168 and 4.17 Å away from atom NE1 of Trp212 (atoms NE2 and NE1 in His168 and Trp212, respectively, correspond to atoms N1 in 4-methylimidazole and N1 in 3-methylindole, respectively). A similar potential is thus applied at distances larger than 4.0 and 5.0 Å between the CM of NH<sub>4</sub><sup>+</sup> and atoms NE2 of His168 and NE1 of Trp212, respectively. In our simulations, we have observed that the average distances between the above mentioned atoms are well below the restraint distances, and they seldom go beyond the restraints. The same constraints are applied for Na<sup>+</sup> and K<sup>+</sup> simulations.

### 2.6.6 Polarizable mechanics/molecular mechanics (PM/MM) simulations setup

When NH<sub>4</sub><sup>+</sup> is placed in S1, two polarizable SWM4 water molecules (1) are positioned at hydrogen bonding distance of NH<sub>4</sub><sup>+</sup>. The polarizable region includes NH<sub>4</sub><sup>+</sup>, the surrounding side chains (F103, F107, F215, W148 and S219), and the two hydrogen-bonding water molecules. When NH<sub>4</sub><sup>+</sup> is placed in S2, the polarizable region includes NH<sub>4</sub><sup>+</sup>, the surrounding side chains (F107, H168, W212, F215 and H318), and three to four SWM4 water molecules in the hydrophobic pore. When NH<sub>4</sub><sup>+</sup> is placed in S4, the polarizable region includes the side chains of H168, H318 and F31, as well as five SWM4 water molecules in the pore and below S4. After NH<sub>4</sub><sup>+</sup> is added, a K<sup>+</sup> ion is removed from the bulk solution so that the system remains neutral. In all simulations, periodic boundary conditions are applied, and electrostatic interactions are computed using particle-mesh Ewald method (17) with 1.0 Å grid spacing. The van der Waals interactions are cut off at 12 Å. Velocity Verlet integrator is used and integration time step is 1 fs. All covalent bonds with hydrogen are fixed using the RATTLE/Roll algorithm (18). Modified, dual-thermostat Andersen–Hoover equations are used to maintain

constant temperature and constant pressure (1 atm) (19). Atoms are kept at 298.15 K and Drude oscillators at 1.0 K.

### 2.6.7 QM/MM simulations setup

All QM/MM simulations are performed using the CP2K program (20). The interaction energy of the QM region is calculated with the Quickstep module (21). The wavefunctions are described by plane waves augmented with a triple-zeta Gaussian basis set with p-type and d-type polarization functions (22). The plane waves are cut off at 300 Ry and the core electrons are described by Goedecker–Teter–Hutter pseudopotentials(23,34). BLYP functional (25,26) is used to compute the exchange and correlation energy. For the MM region, the interaction energy is calculated with the FIST module (20) and the CHARMM param27 force field (14) is used. Langevin dynamics (27) is used to control the temperature at 298.15 K. The friction coefficient is set at  $0.004 \text{ fs}^{-1}$  for the first 2 ps in order to quickly thermalize the system, and then changed to  $0.0005 \text{ fs}^{-1}$ . The QM periodic images are decoupled using atomic point charges derived from electron density (28). The electrostatic coupling between the QM and MM regions is computed via a real space multigrid procedure (20). IMMOM link atom approach (29) is used to treat the linkage between the QM and MM regions (i.e., between the  $C_\beta$ 's and the  $C_\alpha$ 's of the side chains).

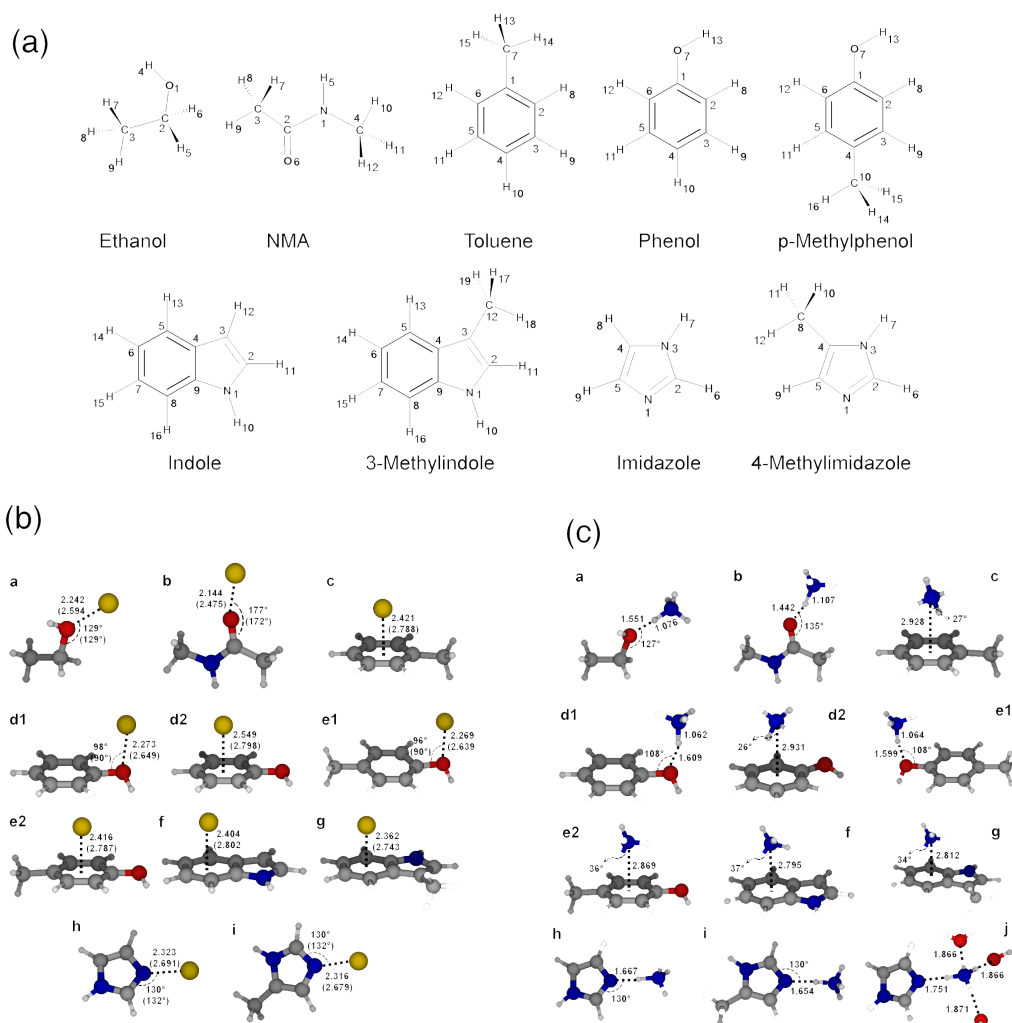


**Figure 2.8.** Compounds and structures used in parameterization. Panel (a) shows the diagrams of the nine compounds studied in complex with  $\text{Na}^+$ ,  $\text{K}^+$ , and  $\text{NH}_4^+$ . Benzene–ion and water–ion complexes have been described in previous work (7). Panel (b) shows the optimized geometries for complexes of  $\text{Na}^+$  with: a, ethanol; b, N-methylacetamide; c, toluene; d, phenol; e, p-methylphenol; f, indole; g, 3-methylindole; h, imidazole; and i, 4-methylimidazole. Parameters for corresponding  $\text{K}^+$  complexes in parentheses. Panel (c) shows Optimized geometries for complexes of  $\text{NH}_4^+$  with: a, ethanol; b, N-methylacetamide; c, toluene; d, phenol; e, p-methylphenol; f, indole; g, 3-methylindole; h, imidazole; and i, 4-methylimidazole. Structure j is showing optimized geometry of the imidazole– $\text{NH}_4^+(\text{H}_2\text{O})_3$  complex



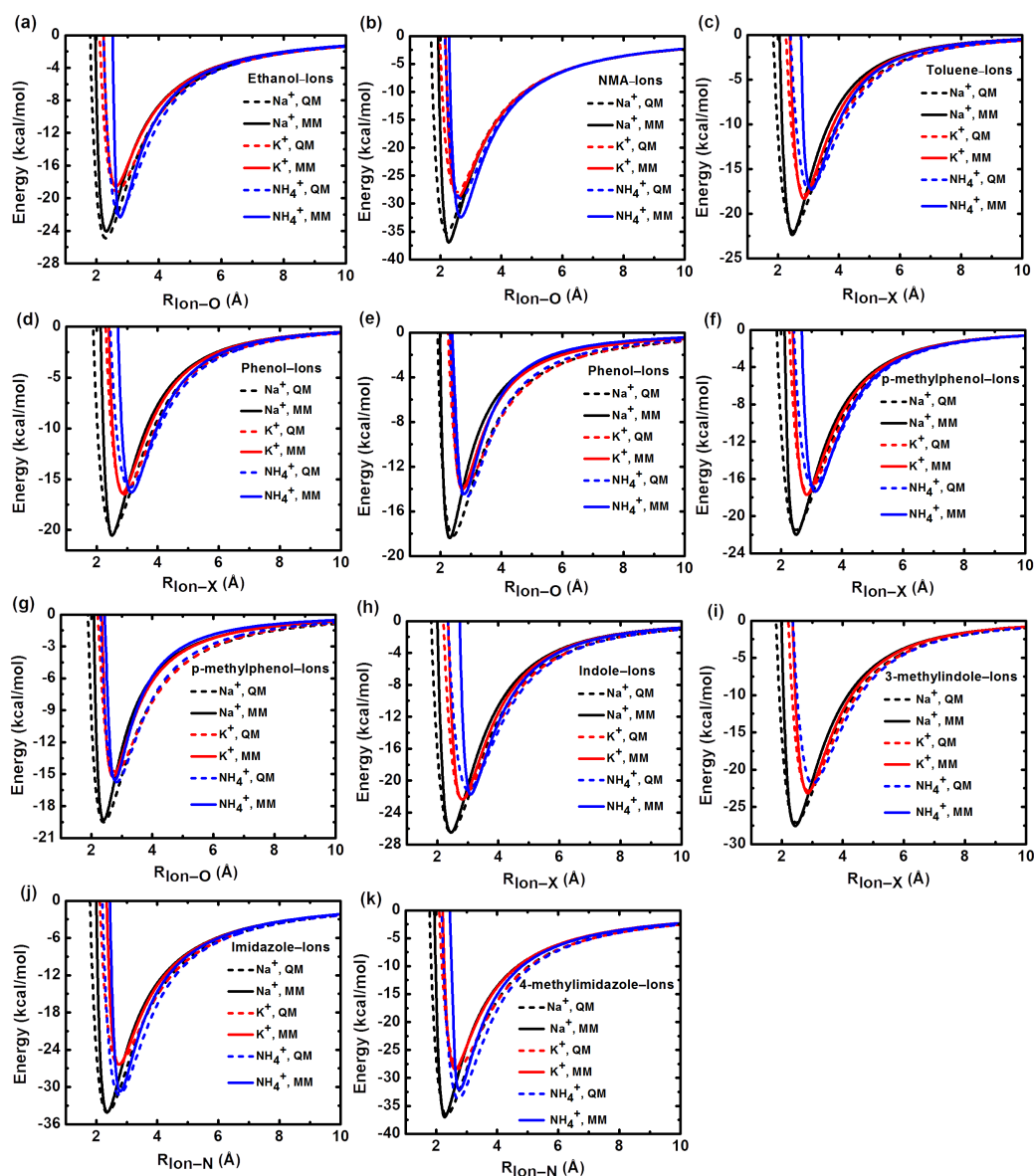


**Figure 2.9** Potential energy curves calculated using ab initio MP2(FC)/6-311++G(d,p) theory (“QM”, dashed lines) and Drude oscillator models (“MM”, solid lines) for the interaction of  $\text{Na}^+$ ,  $\text{K}^+$ , and  $\text{NH}_4^+$  with: (a) ethanol; (b) NMA; (c) toluene; (d,e) phenol; (f,g) p-methylphenol; (h) indole; (i) 3-methylindole; (j) imidazole; and (k) 4-methylimidazole

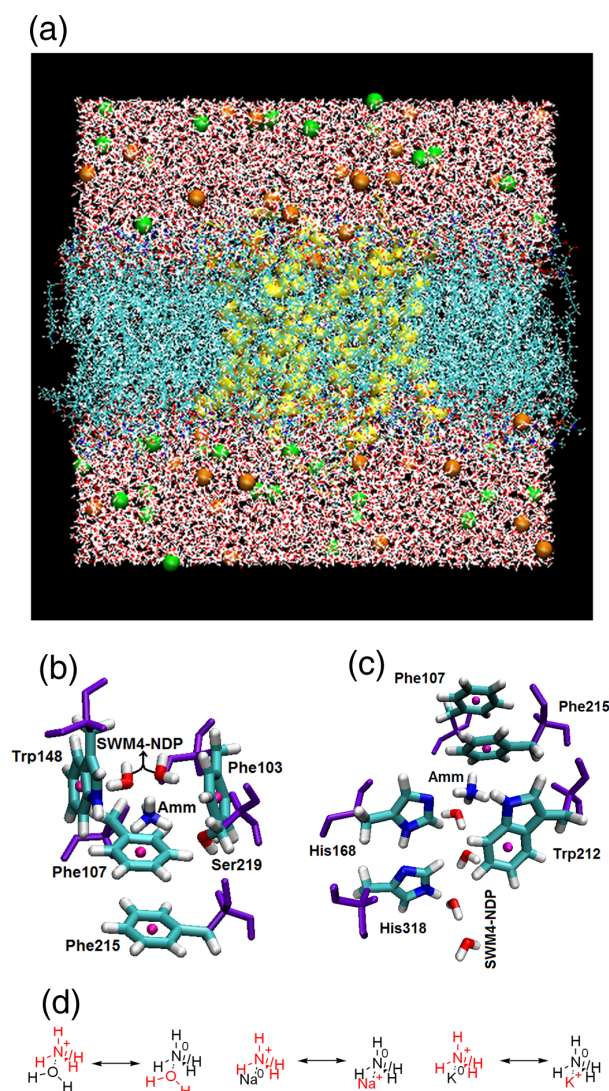


**Figure 2.10** Panel (a) shows AmtB membrane protein model (unit cell) for molecular dynamics simulations. The structure of AmtB monomer is shown in yellow cartoon. Atom colors are red for oxygen, blue for nitrogen, cyan for carbon, white for hydrogen, orange for potassium, and green for chloride. Panel (b) shows a snapshot from MD simulations showing ammonium ion in site S1 and surrounding residues. Atom colors are red for oxygen, blue for nitrogen, cyan for carbon, and white for hydrogen. Non-atomic sites in Phe and Trp side chains are presented as pink spheres and non-polarizable segments of the amino acids are colored in violet. Panel (c) shows a snapshot from MD simulations showing ammonium ion in S2 and surrounding residues. Colors are as in Figure S1. Panel (d) shows the ligand transformations involved in the free energy calculations. Fragments in red are “real” while those in black are “dummy”.

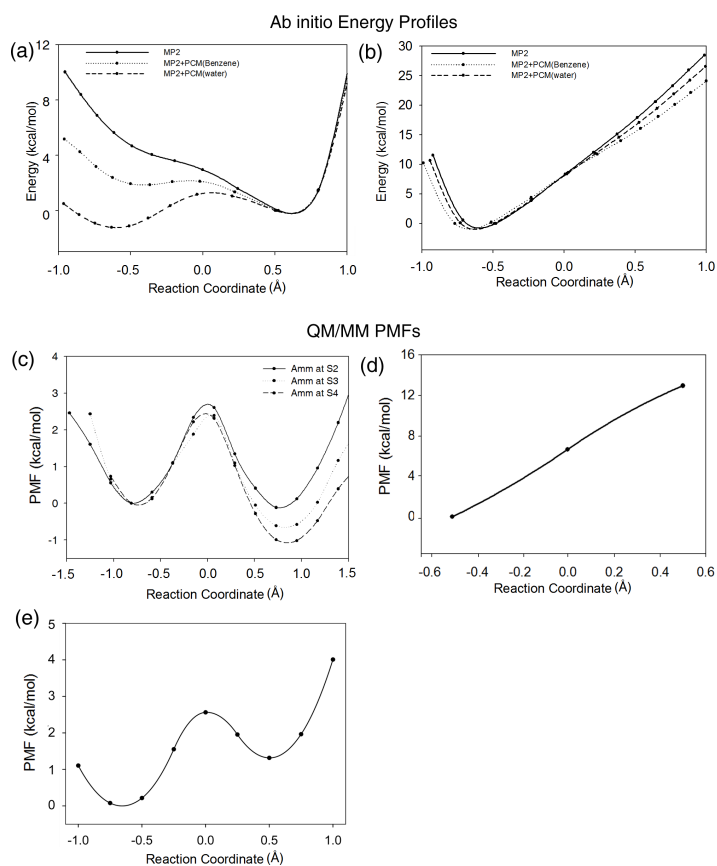


**Figure 2.11** *Ab initio* energy profiles [panels (a) and (b)] and QM/MM PMFs [panels (c), (d) and (e)] for proton transfer reactions. Panels (a) and (b) show the *ab initio* energy profiles for proton transfer from ammonium to imidazole and from ammonium to water, respectively, calculated at the MP2(FC)/6-311++(d,p) level using Gaussian 09 (9). The reaction coordinate is defined as  $RC = d_{N(\text{amm})-H} - d_{N(\text{imid})-H}$  for panel (a) and as  $RC = d_{N(\text{amm})-H} - d_{O(\text{wat})-H}$  for panel (b). In panel (a),  $RC \sim -0.5 \text{ \AA}$  corresponds to the ammonium–imidazole complex and  $RC \sim +0.6 \text{ \AA}$  corresponds to the ammonia–imidazolium complex. The energy profiles are shown in solid lines for MP2 in vacuum, in dotted lines for MP2 embedded in a polarizable continuum model (PCM) of liquid benzene (73), and in dashed lines for MP2 in a PCM of liquid water. Panels (c), (d) and (e) show the QM/MM PMFs for proton transfer from His168 to His318, from His318 to water in S4, and from His318 to NH<sub>3</sub> in S4, respectively. For panels (d) and (e), the His168–His318 histidine pair is positively charged in the reactant state. PMFs for proton transfer reactions from His318 to water and His318 to NH<sub>3</sub> are calculated from constrained QM/MM simulations, using reaction coordinates  $RC = d_{N(\text{His318})-H} - d_{O(\text{water})-H}$  and  $RC = d_{N(\text{His318})-H} - d_{N(\text{NH}_3)-H}$ . PMFs for proton transfer between His168 and His318 as a function of the substrate position in the pore are obtained from unconstrained QM/MM simulations, using reaction coordinate  $RC = d_{N(\text{His168})-H} - d_{N(\text{His318})-H}$ . Each PMF is collected from two independent 30-ps QM/MM simulations.

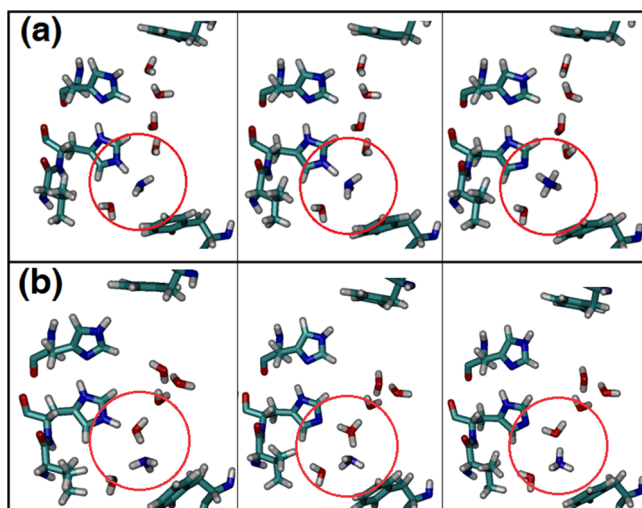


**Figure 2.12** QM/MM snapshots for proton transfer from protonated His318 to  $\text{NH}_3$ . Panel (a) shows the direct proton transfer and panel (b) shows the proton transfer through a bridging water molecule. The snapshots are time-ordered from left to right, and separated by  $\sim 10\text{--}20$  fs.

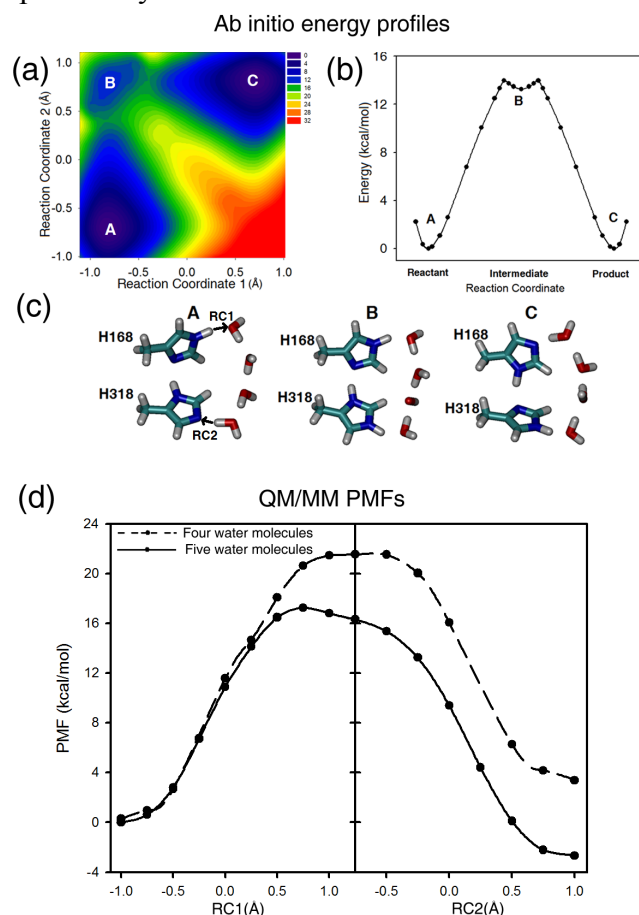


**Figure 2.13** *Ab initio* 2D energy profile [panels (a)-(c)] and QM/MM PMFs [panel (d)] for the proton transfer reaction between His168 and His318 through a water chain. Panels (a), (b) and (c) are results from a gas-phase model calculated at the B3LYP/6-311++(d,p) level using Gaussian 09 (9). The distance between the methyl carbons is fixed at the crystal structure value of  $4.34 \text{ \AA}$ . Panel (a) shows the 2D energy surface (in kcal/mol). Points A, B, and C are reactant, intermediate, and product, respectively.

and product, respectively. Panel (b) shows the 1D energy profile along reaction coordinate 2 (from reactant to intermediate) and reaction coordinate 1 (from intermediate to products). Panel (c) shows the structures of A, B, and C. The reaction coordinates are defined as:  $RC1 = d_{N(\text{His168})-H} - d_{O(\text{Top water})-H}$  and  $RC2 = d_{O(\text{Bottom water})-H} - d_{N(\text{His318})-H}$ . Panel (d) shows PMFs for proton transfer between His168 and His318 through a water chain calculated from QM/MM simulations in the protein environment. There are four water molecules between S2 and S4 for the dashed-line profile, and five for the solid-line profile. The reaction coordinates are defined as  $RC1 = d_{O(\text{water in S4})-H} - d_{N(\text{His318})-H}$  and  $RC2 = d_{N(\text{His168})-H} - d_{O(\text{water in S2})-H}$ . When RC1 is scanned, RC2 is fixed at 0.75 Å, and when RC2 is scanned, RC1 is fixed at 1.25 Å. Each point corresponds to a 5-ps constrained QM/MM simulation.

## 2.6.8 Tables

**Table 2.2** BSSE-corrected and uncorrected complexation energies ( $E^{\text{CP}}$  and  $E$ , respectively, in kcal/mol) and the interaction energies calculated by the optimized potential models ( $E^{\text{MM}}$ , in kcal/mol).

Molecule	Na <sup>+</sup>			K <sup>+</sup>			NH <sub>4</sub> <sup>+</sup>			
	$E$	$E^{\text{CP}}$	$E^{\text{MM}}$	$E$	$E^{\text{CP}}$	$E^{\text{MM}}$	$E$	$E^{\text{CP}}$	$E^{\text{MM}}$	
Ethanol	-27.64	-26.48	-26.48	-21.31	-20.21	-20.21	-27.00	-25.02	-24.94	
NMA	-39.15	-38.25	-38.25	-31.48	-30.36	-30.40	-39.10	-36.92	-36.95	
Benzene <sup>a</sup>	-24.00	-21.08	-21.04	-19.58	-17.14	-17.01	-19.78	-17.58	-17.56	
Toluene	-25.77	-22.96	-22.98	-21.25	-18.79	-18.80	-21.45	-18.92	-19.06	
Phenol	1	-26.16	-24.46	-22.25	-21.52	-19.59	-17.42	-24.90	-22.41	-19.30
	2	-24.49	-21.75	-22.30	-20.37	-18.01	-18.14	-20.67	-18.08	-18.64
p-methylphenol	1	-27.60	-25.97	-24.98	-22.89	-21.04	-19.02	-26.24	-23.82	-21.52
	2	-26.05	-23.37	-23.85	-21.96	-19.45	-20.26	-22.35	-19.71	-20.24
Indole	-30.45	-27.48	-27.40	-25.75	-23.22	-23.24	-26.80	-24.06	-24.06	
3-methylindole	-31.48	-28.51	-28.55	-26.83	-24.08	-24.10	-27.45	-24.60	-24.60	
Imidazole	-36.33	-35.28	-35.29	-28.28	-27.09	-27.10	-34.14	-32.61	-32.62	
4-methylimidazole	-38.42	-37.37	-37.40	-30.08	-28.86	-28.90	-36.19	-34.62	-34.65	

<sup>a</sup> from reference 7

**Table 2.3** Pair-specific LJ parameters between atoms of the interacting ligands and of Na<sup>+</sup>, K<sup>+</sup>, and NH<sub>4</sub><sup>+</sup>

Molecule	i	E <sub>min</sub> (kcal/mol)	R <sub>min/2</sub> (Å)	Pair-specific LJ parameters							
				Na <sup>+</sup>		K <sup>+</sup>		N(NH <sub>4</sub> <sup>+</sup> )		H(NH <sub>4</sub> <sup>+</sup> )	
				E <sub>min<sub>i,Na</sub></sub> (kcal/mol)	R <sub>min<sub>i,Na</sub></sub> (Å)	E <sub>min<sub>i,K</sub></sub> (kcal/mol)	R <sub>min<sub>i,K</sub></sub> (Å)	E <sub>min<sub>i,N</sub></sub> (kcal/mol)	R <sub>min<sub>i,N</sub></sub> (Å)	E <sub>min<sub>i,H</sub></sub> (kcal/mol)	R <sub>min<sub>i,H</sub></sub> (Å)
Ethanol	O1	0.150	1.765	0.0646602	3.3039910	0.1243324	3.5079747	0.2387032	3.2892187	0.0056963	2.9830579
	C2	0.056	2.100	0.1821140	4.1241884	0.1107728	4.4162018	0.2485402	4.4784472	0.0149625 <sup>d</sup>	3.1870509 <sup>d</sup>
NMA	O6	0.180	1.900	0.1265593	3.1410382	0.1175736	3.5155648	0.0268833	4.3252218	0.0004449	2.7216686
	C2	0.100	1.600	0.3200516	4.2791542	0.0927968	4.8724768	0.5612547	4.4757974	0.00518658	3.2710700
Benzene <sup>a</sup>	C1–6	0.069	2.090	0.2004369	3.3592376	0.4266716	3.5744944	0.4058387	3.3962713	0.1470587	3.5005950
	X	0.000	0.000	0.0099919	3.6398984	0.0	0.0	0.1470587	3.5000595	0.0060183	3.2808392
Toluene <sup>b</sup>	C1–6	0.069	2.090	0.2099100	3.3338282	0.3967730	3.5383424	0.4058387	3.3962713	0.1470587	3.5005950
	X	0.0	0.0	0.0087380	3.5086672	0.0	0.0	0.1470587	3.5000595	0.0060183	3.2808392
Phenol	O7	0.200	1.740	0.5611584	2.7723496	1.9813187	2.9146000	0.4299035	3.4721698	0.0024378	2.7034540
	X	0.000	0.000	0.0088122	4.0595579	0.0054752	4.4594059	0.0286866	4.5811533	0.0	0.0
p-methylphenol	O7	0.200	1.740	1.9972693	2.6512629	2.6417092	2.8654004	0.3975307	3.3358123	0.0184439	2.5637375
	X	0.0	0.0	0.0025728	4.4983402	0.0038311	4.5960484	0.0187195	4.6998372	0.0	0.0
Indole	C5–8	0.069	2.090	0.0334734	3.8759811	0.2198221	3.7019494	0.3072126	3.6967341	0.0122287	3.3760382
	C4,9	0.038	1.900	0.0334734	3.8759811	0.2198221	3.7019494	0.3072126	3.6967341	0.0122287	3.3760382
	X	0.0	0.0	0.0	0.0	0.0	0.0	0.6602695	3.1297834	0.0270212	2.9105631
3-methylindole	C5–8	0.069	2.090	0.0043736	4.5302101	0.1757715	3.7481552	0.3105234	3.7323063	0.0083613	3.4949277
	C4,9	0.038	1.900	0.0043736	4.5302101	0.1757715	3.7481552	0.3105234	3.7323063	0.0083613	3.4949277
	X	0.0	0.0	0.0	0.0	0.0	0.0	0.6632312	2.9908044	0.0271424	2.7715841
Imidazole	N1	0.069	1.956	0.1802843	3.1905921	0.8180299	3.2755577	0.1159641	3.9018492	0.0104965	2.7094400
	C4,5	0.095	2.070	0.1935770	3.6796462	0.1161164 <sup>c</sup>	3.7566521 <sup>c</sup>	0.4762014 <sup>e</sup>	3.3762713 <sup>e</sup>	0.0194882 <sup>e</sup>	3.1570509 <sup>e</sup>
	C2	0.093	1.980	0.1935770	3.6796462	0.1148876 <sup>c</sup>	3.6666521 <sup>c</sup>	0.4711621 <sup>e</sup>	3.2862713 <sup>e</sup>	0.0192820 <sup>e</sup>	3.0670509 <sup>e</sup>
4-methylimidazole	N1	0.069	1.956	0.1937232	3.0987322	0.2187421	3.4183194	0.1135793	3.8854367	0.0131107	2.7372252
	C2	0.093	1.980	0.2048993	3.9754195	0.2902294	4.3026690	0.4711621 <sup>e</sup>	3.2862713 <sup>e</sup>	0.0192820 <sup>e</sup>	3.0670509 <sup>e</sup>

<sup>a</sup> Parameters from reference 7<sup>b</sup> Parameters for interaction with NH<sub>4</sub><sup>+</sup> are same as for benzene (7).<sup>c</sup> Obtained from alkali potassium (8) and imidazole (9) parameters using the Lorenz–Berthelot mixing rules<sup>d</sup> Obtained from ammonium (7) and ethanol (6) parameters using the Lorenz–Berthelot mixing rules<sup>e</sup> Obtained from ammonium (7) and imidazole (3) parameters using the Lorenz–Berthelot mixing rules

**Table 2.4** Average distances (in Å) from ammonium to surrounding residues and water in S1. For ammonium, water and S219, the positions are represented by nitrogen, oxygen, and hydroxyl oxygen, respectively. For F103, F107 and W148, the positions are represented by the center of their six-membered rings.

Residue or molecule	Mode 1	Mode 2	Exp. <sup>a</sup>
S219	2.8	5.0	2.8
F107	3.7	3.2	4.2
F103	5.9	4.1	5.5
W148	4.2	5.0	3.9
Wat1	2.8	2.8	2.8
Wat2	2.8	2.8	2.5

### 2.6.9 References

1. Lamoureux G, Harder E, Vorobyov IV, Roux B, MacKerell AD. A polarizable model of water for molecular dynamics simulations of biomolecules. *Chem Phys Lett* 2006;418(1):245-9."
2. Lamoureux G, MacKerell Jr AD, Roux B. A simple polarizable model of water based on classical drude oscillators. *J Chem Phys* 2003;119:5185.
3. Lopes PE, Roux B, MacKerell AD. Molecular modeling and dynamics studies with explicit inclusion of electronic polarizability: Theory and applications. *Theoretical Chemistry Accounts: Theory, Computation, and Modeling (Theoretica Chimica Acta)* 2009;124(1):11-28.
4. Lopes PE, Lamoureux G, Roux B, Mackerell AD. Polarizable empirical force field for aromatic compounds based on the classical drude oscillator. *J Phys Chem B* 2007, Mar 22;111(11):2873-85.
5. Harder E, Anisimov VM, Whitfield T, MacKerell AD, Roux B. Understanding the dielectric properties of liquid amides from a polarizable force field. *J Phys Chem B* 2008, Mar 20;112(11):3509-21.
6. Anisimov VM, Vorobyov IV, Roux B, Mackerell AD. Polarizable empirical force field for the primary and secondary alcohol series based on the classical drude model. *J Chem Theory Comput* 2007;3(6):1927-46.
7. Orabi EA, Lamoureux G. Cation-  $\pi$  and  $\pi$ - $\pi$  interactions in aqueous solution studied using polarizable potential models. *J Chem Theory Comput* 2011;8(1):182-93.
8. Yu H, Whitfield TW, Harder E, Lamoureux G, Vorobyov I, Anisimov VM, et al. Simulating monovalent and divalent ions in aqueous solution using a drude polarizable force field. *J Chem Theory Comput* 2010;6(3):774-86.
9. Frisch, MJEa and Trucks, GW and Schlegel, HB and Scuseria, GE and Robb, MA and Cheeseman, JR and Scalmani, G and Barone, V and Mennucci, B and Petersson, GA and others. *Gaussian 09, revision A. 02*, gaussian. Inc., Wallingford, CT 2009, Sep 20;2(3):4.
10. Boys SF, Bernardi F. The calculation of small molecular interactions by the differences of separate total energies. Some procedures with reduced errors. *Molecular Physics* 2002;100(1):65-73.



11. Gallivan JP, Dougherty DA. Cation- $\pi$  interactions in structural biology. *Proc Natl Acad Sci U S A* 1999, Aug 17;96(17):9459-64.
12. Mecozzi S, West AP, Dougherty DA. Cation- $\pi$  interactions in aromatics of biological and medicinal interest: Electrostatic potential surfaces as a useful qualitative guide. *Proc Natl Acad Sci U S A* 1996, Oct 1;93(20):10566-71.
13. Vijay D, Sastry GN. The cooperativity of cation- $\pi$  and  $\pi$ - $\pi$  interactions. *Chem Phys Lett* 2010;485(1):235-42.
14. MacKerell Jr AD, Bashford D, Bellott M, Dunbrack Jr RL, Evanseck JD, Field MJ, et al. All-atom empirical potential for molecular modeling and dynamics studies of proteins. *The Journal of Physical Chemistry B* 1998;102(18):3586-616.
15. Jorgensen WL, Chandrasekhar J, Madura JD, Impey RW, Klein ML. Comparison of simple potential functions for simulating liquid water. *J Chem Phys* 1983;79:926.
16. Khademi S, O'Connell J, Remis J, Robles-Colmenares Y, Miercke LJ, Stroud RM. Mechanism of ammonia transport by amt/MEP/rh: Structure of amtB at 1.35 Å. *Science* 2004, Sep 10;305(5690):1587-94.
17. Darden T, York D, Pedersen L. Particle mesh ewald: An  $N \log(N)$  method for ewald sums in large systems. *J Chem Phys* 1993;98:10089.
18. Martyna GJ, Tuckerman ME, Tobias DJ, Klein ML. Explicit reversible integrators for extended systems dynamics. *Molecular Physics* 1996;87(5):1117-57.
19. Lamoureux G, Roux B. Modeling induced polarization with classical drude oscillators: Theory and molecular dynamics simulation algorithm. *J Chem Phys* 2003;119:3025.
20. Laino T, Mohamed F, Laio A, Parrinello M. An efficient real space multigrid QM/MM electrostatic coupling. *J Chem Theory Comput* 2005;1(6):1176-84.
21. VandeVondele J, Krack M, Mohamed F, Parrinello M, Chassaing T, Hutter J. Quickstep: Fast and accurate density functional calculations using a mixed gaussian and plane waves approach. *Computer Physics Communications* 2005;167(2):103-28.
22. Schäfer A, Huber C, Ahlrichs R. Fully optimized contracted gaussian basis sets of triple zeta valence quality for atoms li to kr. *J Chem Phys* 1994;100:5829.

23. Goedecker S, Teter M, Hutter J. Separable dual-space gaussian pseudopotentials. *Physical Review B* 1996;54(3):1703.

24. Hartwigsen C, Goedecker S, Hutter J. Relativistic separable dual-space gaussian pseudopotentials from H to rn. *Physical Review B* 1998;58(7):3641.

25. Becke AD. Density-functional exchange-energy approximation with correct asymptotic behavior. *Physical Review A* 1988;38(6):3098.

26. Lee C, Yang W, Parr RG. Development of the colle-salvetti correlation-energy formula into a functional of the electron density. *Physical Review B* 1988;37(2):785.

27. Ricci A, Ciccotti G. Algorithms for brownian dynamics. *Molecular Physics* 2003;101(12):1927-31.

28. Blochl PE. Electrostatic decoupling of periodic images of plane-wave-expanded densities and derived atomic point charges. *Journal of Chemical Physics* 1995;103(17):7422-8.

29. Maseras F, Morokuma K. IMOMM: A new integrated ab initio+ molecular mechanics geometry optimization scheme of equilibrium structures and transition states. *J Comput Chem* 2004;16(9):1170-9.

### **Chapter 3**

## **DIFFERENT HYDRATION PATTERNS IN THE PORES OF AMTB AND RHCG COULD DETERMINE THEIR TRANSPORT MECHANISMS**

This chapter was published in the *Biochemistry Journal* (2013, 52, 7091-7098) by the following authors: Sefer Baday, Shihao Wang, Simon Berneche, and Guillaume Lamoureux.

### 3.1 Abstract

The ammonium transporters of the Amt/Rh family facilitate the diffusion of ammonium across cellular membranes. Functional data suggest that Amt proteins, notably found in plants, transport the ammonium ion ( $\text{NH}_4^+$ ) while human rhesus (Rh) proteins transport ammonia ( $\text{NH}_3$ ). Comparison between the X-ray structures of the prokaryotic AmtB, assumed to be representative of Amt proteins, and the human RhCG reveals important differences at the level of their pore. Despite these important functional and structural differences between Amt and Rh proteins, studies of the AmtB transporter have led to the suggestion that proteins of both subfamilies work according to the same mechanism and transport ammonia. We performed molecular dynamics simulations of the AmtB and RhCG proteins under different water and ammonia occupancy states of their pore. Free energy calculations suggest that the probability of finding  $\text{NH}_3$  molecules in the pore of AmtB is negligible in comparison to water. The presence of water in the pore of AmtB could support the transport of proton. The pore lumen of RhCG is found to be more hydrophobic due to the presence of a phenylalanine conserved among Rh proteins. Simulations of RhCG also reveal that the signature histidine dyad is occasionally exposed to the extra-cellular bulk, which is never observed in AmtB. These different hydration patterns are consistent with the idea that Amt and Rh proteins are not functionally equivalent and that permeation takes place according to two distinct mechanisms.

### 3.2 Introduction

Proteins from the Amt/Rh family facilitate the transport of ammonium across cellular membrane. Functional studies have generally suggested that members of the Amt subfamily, notably found in plants, transport the ammonium ion ( $\text{NH}_4^+$ ) (1-4), while the mammalian Rh proteins conduct ammonia ( $\text{NH}_3$ ) (5,6).

The elucidation of the structure of the prokaryotic AmtB transporter, the first in the Amt/Rh family, has brought essential new insights toward the understanding of the function of ammonium transporters (7,8). Nevertheless, the mechanism of transport and the substrate of AmtB itself remain a matter of debate with important consequences since AmtB is often considered as an archetype of the Amt subfamily. A close examination of the structural and functional data reveals many incompatible observations. On the basis of X-ray diffraction data, it was suggested that the pore of AmtB is occupied by ammonia molecules diffusing in single file (7). Electronic density was however also observed in crystals grown in absence of ammonium salt, arguing against the above conclusion (9). While different functional studies based on transport assays, growth experiments, and pH measurements led to the suggestion that AmtB transports ammonia (7,10), a critical assessment of these different approaches shows the difficulties in applying such measurements to AmtB and in interpreting the available data (11). A mutational study has also highlighted the specific chemistry essential to transport in AmtB, supporting the idea of strong interactions with an ammonium ion rather than with neutral ammonia (12). Incomplete or partial analyses of the available X-ray and functional data on AmtB have led to an amalgam between the function of Amt and Rh proteins, which are now often both described as “ammonia channels”.

Comparison of the X-ray structures of the AmtB (7) and RhCG (13) pores reveals significant differences (Figure 3.1). While the two transporters share the same overall pore architecture, some residues at key positions differ (14). First, the two phenylalanine residues forming a gate at the entrance of the pore lumen do not adopt the same conformation in the crystals of the two proteins. Whether this apparent difference is functionally important is unknown. Second, a threonine (Thr273) is found at the entrance of the pore lumen of AmtB, above the histidine dyad. Electronic density in that region of the pore was observed in RhCG crystals

and attributed to a water molecule. While both the threonine side chain and the water molecule present a hydroxyl group at similar positions, their mobilities are different and can potentially differentiate the two pores. Finally, in RhCG a phenylalanine (Phe74) occupies a large portion of the pore at the level of the two signature histidine residues, while the pore of AmtB is unobstructed.

Among contentious elements is the possible presence of water molecules in the pore lumen of the ammonium transporters (15). As we demonstrated in a previous study, water molecules in the pore can stabilize the charged  $\text{NH}_4^+$  and transport proton, allowing for electrogenic transport in AmtB (16). Water molecules could thus be determinant for the transport mechanism.

To better understand the similarities and differences between the Amt and Rh proteins, we perform molecular dynamics simulations of the AmtB and RhCG proteins. More specifically we compare the ammonia and water occupancy in the pore of the two transporters. The simulations uncover important differences, notably at the level of the pore lumen which is hydrophobic in RhCG but hydrophilic in AmtB. The RhCG simulations also reveal a pore exposing the histidine dyad to extracellular bulk water. Our study suggests that two distinct mechanisms sustain ammonium permeation in Amt and Rh proteins.

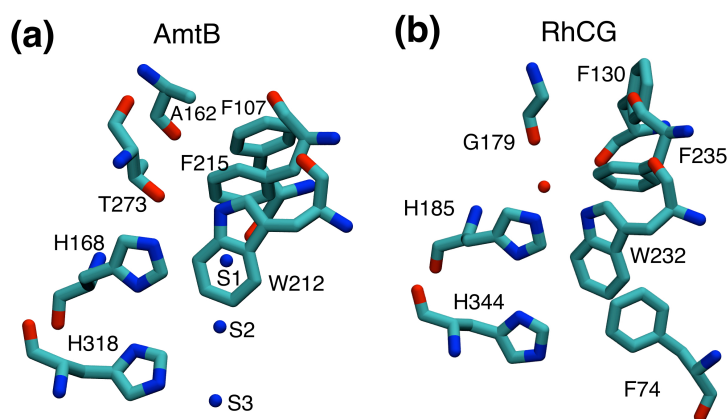


**Figure 3.1** Details of the pore of the AmtB (a) and RhCG (b) proteins (PDB entries 1U7G and 3HD6). a) Electronic density in the pore lumen of AmtB was attributed to three ammonia molecules putatively diffusing in single file. b) In RhCG, electronic density just above His185 was attributed to a water molecule. In both schemes, the extracellular side is upward.

### 3.3 Results

#### 3.3.1 Stability of ammonia molecules in the pore of AmtB

To first investigate the stability of ammonia molecules in the pore of AmtB, we performed a simulation of the AmtB trimer starting with three ammonia molecules placed in each pore at positions corresponding to experimental electron density maxima. In all monomers, all three ammonia molecules leave the pore: Some after only a few nanoseconds of simulation, other after 80 or 90 ns. At the end of the simulation, the pores of two of the three monomers are filled with three or four water molecules (Figure 3.2.a). In monomer A, in the last few nanoseconds of the 100-ns simulation, a water molecule inserts between the two histidines residues. A similar conformation is more extensively sampled in another simulation (Figure 3.3.c; see below). Overall, the trajectories presented in Figure 3.2 show that ammonia molecules are metastable in the AmtB pore and are replaced by water molecules on the timescale of the simulation.

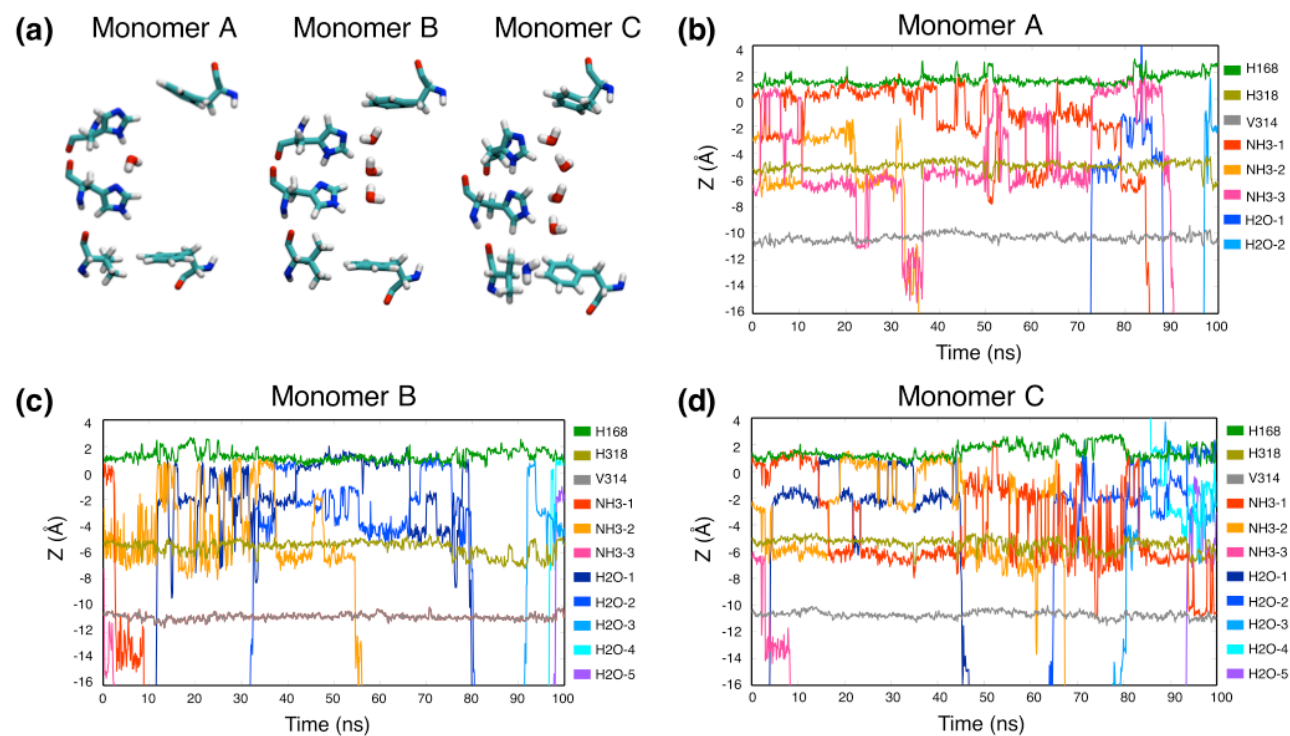


**Figure 3.2** Simulation of AmtB initiated with three ammonia molecules in each pore. a) Configurations at the end of the simulation showing key residues and water molecules in the pore for all three monomers. b-d) Positions along Z-axis of ammonia and water molecules in the pore of monomers A, B, and C.  $Z=0$  corresponds to the center of mass of the protein. Some water molecules entering the pore only briefly are not shown in the time series



### 3.3.2 Stability of water molecules in the pore of AmtB

To confirm water stability in the AmtB pore, two additional simulations of the trimeric system were performed, with and without water molecules initially present in the pore. Water molecules that were placed beforehand in the pore undergo many exchanges with water molecules from the cytosolic vestibule (see Figure 3.10). In simulations in which the pore was initially empty, water molecules are seen entering the pores and occupying up to four distinct binding sites. Figure 3.3.a shows conformations of water molecules inside the pore at the end of a simulation of the AmtB trimer initiated with three empty pores. The time series of Figure 3.3.b-c show that water molecules filled up the pore in less than 10 ns in monomers A and B. In monomer C, three water molecules fill up the pore after about 35 ns. In this situation, water molecules usually form a stable chain as illustrated in Figure 3.3.a. Water molecules exchange positions many times over the whole simulation, with entry and exit of some of them. All movement of water molecules in and out the pore happen from the intra-cellular side, except one event (see Figure 3.3.d, at  $t \approx 55$  ns). This shows that the gate formed by the Phe residues on the extra-cellular side of the pore has extremely low permeability to water, in agreement with experiments showing that AmtB does not conduct water (7). In monomer B, a water molecule intercalates between the two histidine residues in the interval  $t = 30$  to 40 ns, and again starting at  $t = 60$  ns (see Figure 3.3.c). The water molecule is metastable in this position and is replaced a few times over the remaining 40 ns. When a water molecule is found between residues His168 and His318, the two side-chains are further away from each other, and His168 N $\epsilon$  is no longer in position to stabilize water molecules in the pore. Once the intercalated water molecule leaves, the two histidine side-chains regain their initial conformation. Figure 3.4 presents the density profile describing the average water occupancy in AmtB extracted from the simulation initiated with empty pores. The density profile for each monomer is shown in Figure 3.11.

We also performed simulations of the AmtB trimer considering an alternative protonation state of the histidine dyad with hydrogen atoms on N $\epsilon$  of His168 and N $\delta$  of His318, without water molecules initially bound to the pore. The density profile (reported in Figure 3.4) shows that water molecules are less stable for this reverse protonation state than for the canonical one, in agreement with our

previous work (15). Nevertheless, a water chain of three or more water molecules is observed for a non-negligible fraction of the simulation time for the reversed protonation state, which would allow proton diffusion as recently proposed (16). The standard-deviation of the density profiles, calculated by dividing the simulations in 5 intervals, is shown in Figure 3.12.

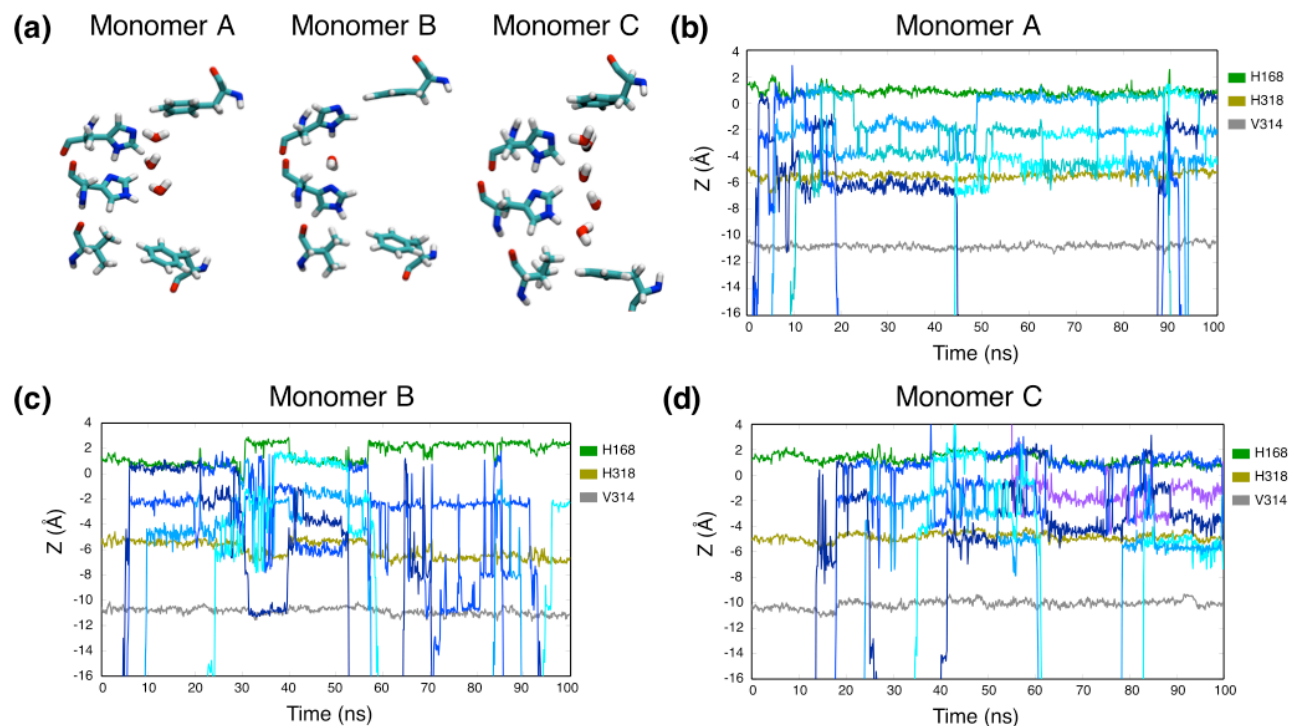


**Figure 3.3** Simulation of AmtB started with empty pores. a) Configurations of water molecules in the pores of all monomers at the end of the simulation. b-d) Positions along the Z-axis of water molecules in the pore of monomers A, B, and C. Traces that are not labeled in the legend correspond to water molecules.  $Z=0$  corresponds to the center of mass of the protein.

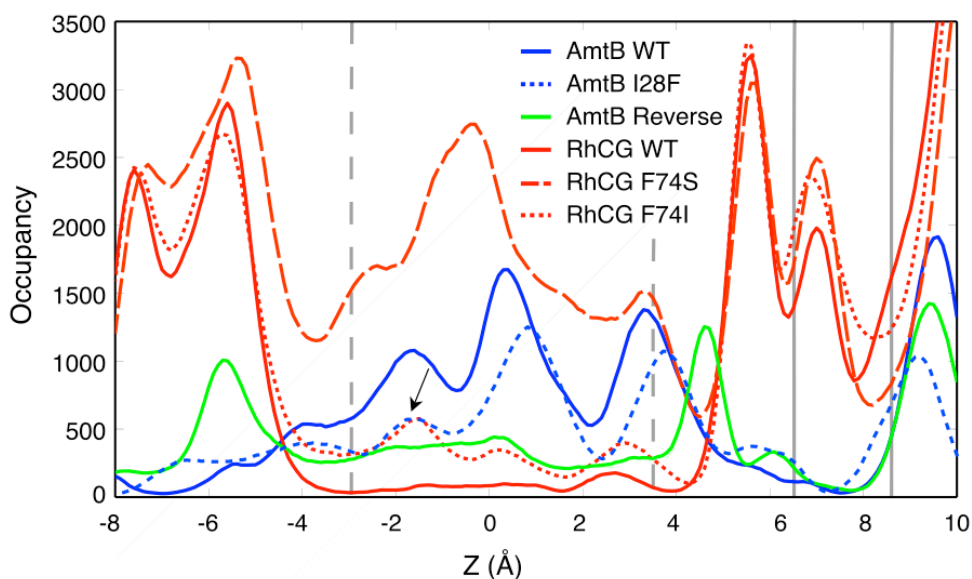


**Figure 3.4** Water occupancy in the pore of the different constructs of AmtB and RhCG. In all cases, histograms were calculated from 100-ns long simulations initiated with empty pores, and averaged over the three monomers. The  $Z$  position is calculated relative to the center of mass of the alpha-carbons of the two histidines residues lining the pore. The grey dashed lines indicate the position of the  $N\epsilon$  atoms of these two histidines. The solid lines correspond to the position of the  $C\alpha$  of the two phenylalanines on the extracellular side of the pore. The meaning of the arrow is described in the text.

### 3.3.3 Relative stabilities of water and ammonia in the pore of AmtB

The simulations presented above suggest that  $\text{NH}_3$  and  $\text{H}_2\text{O}$  molecules may both occupy the pore of AmtB. To have a more precise idea of their relative stability, we have performed free energy perturbation (FEP) calculations in which a water molecule is alchemically transformed into an ammonia molecule both in water bulk and in the pore of AmtB. The free energy difference between transferring an ammonia (A) or a water (W) molecule from the bulk to the pore can be expressed as:

$$\begin{aligned}
 \Delta\Delta G &= [G(A_{\text{pore}}) - G(A_{\text{bulk}})] - [G(W_{\text{pore}}) - G(W_{\text{bulk}})] \\
 &= [G(A_{\text{pore}}) - G(W_{\text{pore}})] - [G(A_{\text{bulk}}) - G(W_{\text{bulk}})] \\
 &= \Delta G(W_{\text{pore}} \rightarrow A_{\text{pore}}) - \Delta G(W_{\text{bulk}} \rightarrow A_{\text{bulk}})
 \end{aligned}
 \tag{1}$$

The perturbation calculation in the bulk water system in which a water molecule is alchemically transformed to ammonia (second term of Equation 3.1) yields a free energy difference of  $+2.7 \pm 0.1$  kcal/mol (BAR estimate), comparable to the difference of experimental solvation free energy for water and ammonia of +2 kcal/mol (24). Several similar FEP calculations were performed in the pore (first term of Equation 3.1) with various occupancy states. For these calculations, water and ammonia molecules in the pore were restrained to their respective binding sites (see Methods). Results from these calculations are reported in Table 3.1. The free energy differences for transforming a water molecule into ammonia in the pore are between 0.9 and 4.0 kcal/mol. The average of the different perturbation calculations is +2.8 kcal/mol, which yields an average free energy difference between the transfer of water and ammonia from bulk water to the pore,  $\Delta\Delta G$ , of about +0.1 kcal/mol. Given the uncertainty of the calculations, it implies that, on average, the transfer of a water molecule from bulk water into the pore is energetically equivalent to the transfer of an ammonia molecule. These results are comparable to those of Luzhkov et al. (29) who calculated a  $\Delta\Delta G$  of +2.0 kcal/mol for the transformation  $aaa \rightarrow waa$ , while we report +1.0 kcal/mol (Table 1). Accordingly, potential of mean force calculations by Lin et al. have shown little difference between the energetics of ammonia and water in the pore of AmtB (30). Ullmann et al. also found comparable binding free energies for ammonia and water in sites S1 to S4 of Amt-1 from *A. fulgidus*, using Monte Carlo simulations (31).

However, the binding free energy difference is not the only factor determining the probability of observing either water or ammonia molecules in the pore of AmtB. The concentration of both molecules in the environment of the transporter needs to be taken into account as well. We can incorporate the effect of concentration using the following Boltzmann relation

$$\frac{P_{\text{NH}_3}}{P_{\text{H}_2\text{O}}} = \frac{[\text{NH}_3]}{[\text{H}_2\text{O}]} e^{-\Delta\Delta G/k_{\text{B}}T} \quad (2)$$

where  $\frac{P_{\text{NH}_3}}{P_{\text{H}_2\text{O}}}$  the relative binding probability of ammonia versus water in the pore of AmtB,  $\frac{[\text{NH}_3]}{[\text{H}_2\text{O}]}$  is the ratio of water and ammonia concentrations in solution,  $\Delta\Delta G$  is the binding free energy difference between water and ammonia,  $k_{\text{B}}$  is the Boltzmann constant,  $T$  is the temperature.

For a hypothetical concentration of 1 mM for  $\text{NH}_3$  —which is high considering that the AmtB transporter is reportedly expressed at  $\text{NH}_4^+$  concentrations of 50  $\mu\text{M}$  or less (30)— we get a relative probability  $\frac{P_{\text{NH}_3}}{P_{\text{H}_2\text{O}}} = 1.5 \times 10^{-5}$ , with  $[\text{H}_2\text{O}] = 55$  M,  $\Delta\Delta G = 0.1$  kcal/mol, and  $k_{\text{B}}T(315\text{K}) = 0.626$  kcal/mol. With  $\Delta\Delta G = -1.9$  kcal/mol, corresponding to the most favorable transfer of ammonia to the pore of AmtB (first line of Table 3.1), the relative probability is  $\frac{P_{\text{NH}_3}}{P_{\text{H}_2\text{O}}} = 3.8 \times 10^{-4}$ .

Thus, even in artificially high ammonia concentration corresponding to 10 times the one expected in the crystallization experiments of Khademi et al. (7), the probability of finding an ammonia molecule in the pore of AmtB is more than a thousand times lower than that of a water molecule. The probability of finding three ammonia molecules in the pore would be less than  $10^{-10}$  of the probability of finding three water molecules. Taken together, the simulations and free energy calculations suggest that the pore of the AmtB transporter in its resting state is occupied by water molecules for a non-negligible fraction of the time, and that the presence of  $\text{NH}_3$  is highly unlikely.

**Table 3.1** Free energy of various perturbations in the pore of AmtB (kcal/mol)

Perturbation*	Forward	Backward	Average	BAR Estimate	$\Delta\Delta G$
www→aww	1.7	-1.6	1.6	0.9±0.1	-1.8±0.2
aww→aaw	3.2	-4.1	3.6	2.5±0.2	-0.3±0.3
aaw→aaa	3.4	-3.5	3.4	3.7±0.1	1.0±0.2
www→wwa	3.9	-4.7	4.3	3.5±0.1	0.7±0.2
wwa→waa	4.6	-3.6	4.1	4.0±0.1	1.3±0.2
waa→aaa	2.4	-0.9	1.6	1.7±0.2	-1.0±0.3
www→waw	3.6	-3.2	3.4	3.6±0.2	0.9±0.3
awa→aaa	3.7	-3.8	3.7	2.9±0.1	0.2±0.2

\*Triplets denote the occupancy state of sites S1, S2 and S3 as identified on Figure 3.9 (w=H<sub>2</sub>O, a=NH<sub>3</sub>).  $\Delta\Delta G = (\text{BAR Estimate}) - 2.7 \pm 0.1$  kcal/mol, as defined in the text.

### 3.3.4 Stability of ammonia and water molecules in the pore of RhCG

To assess the stability of ammonia molecules in the pore of the RhCG protein, we performed a simulation starting with three ammonia molecules bound to the pore. Figure 3.5a displays the final conformation of molecules in the pore of the three monomers. The time series in Figure 3.5b-d show that the three ammonia molecules leave the pore in all three monomers. In monomer A, an ammonia molecule stays in the vicinity of the pore, just below His344. Contrary to what was observed for AmtB, the pores remain mostly empty. In monomer A, transient visits of NH<sub>3</sub> and H<sub>2</sub>O are seen, with a higher frequency in the first half of the simulation. In monomer C, the two histidines lining the pore (His185/His344) rotate and expose a polar nitrogen to the pore lumen, attracting water molecules (see Figure 3.5d). The stabilization of water molecules in the pore favors the reorientation of the Phe74 side chain. In AmtB, the rotation of the histidine dyad was considered as a potential mechanism allowing for proton transport in the pore, but free energy calculations suggest that it is energetically prohibitive (16).

Whether such conformational change could play a role in the transport of ammonium in RhCG remains to be seen and will require further calculations.

We also carried out a simulation of RhCG starting with empty pores. Analysis of the trajectory shows that while water molecules can occasionally enter the pore, they cannot find stable positions and even less form a chain of three or more molecules. No rotation of the two histidines and water stabilization were observed in this second simulation. The density profile presented in Figure 3.4 illustrates that only a small number of water molecules are found in the pore at the level of the histidine dyad. Figure 3.6a shows the final conformation of the pore and water molecules in its vicinity for each monomer. A simulation initiated with water molecules in the pores yielded similar results (see Figure 3.11.b). Interestingly, in all monomers, a water molecule is seen forming a hydrogen bond with His185 and the carbonyl group of Gly179, occupying a position also identified by X-ray crystallography (see Figure 3.8.b). The simulations further reveal that a chain of water molecules can transiently form between His185 and the extra-cellular bulk (Figure 3.6b,c), opening a direct access to His185. Such conformation is not observed in AmtB, in which access to His168 is blocked by two stacked phenylalanine residues. A comparison of the X-ray structures of RhCG and AmtB reveals subtle but important differences between the two proteins in that region of the pore. First, in the conformations captured by X-ray crystallography, the aromatic rings of the two phenylalanine residues at the entrance of the pore are parallel in AmtB but perpendicular in RhCG (see Figure 3.1). These conformations remain predominant during the MD simulations for AmtB and RhCG (Figure 3.12 and Figure 3.13). Second, in AmtB, Thr273 makes a hydrogen bond with Trp212 and occasionally with His168 during simulations, while in RhCG a water molecule is found at that position, interacting with both His185 and Trp232. Simulations show that this water molecule can also form a hydrogen bond with water molecules at the level of the two phenylalanine residues (Phe130/Phe235).



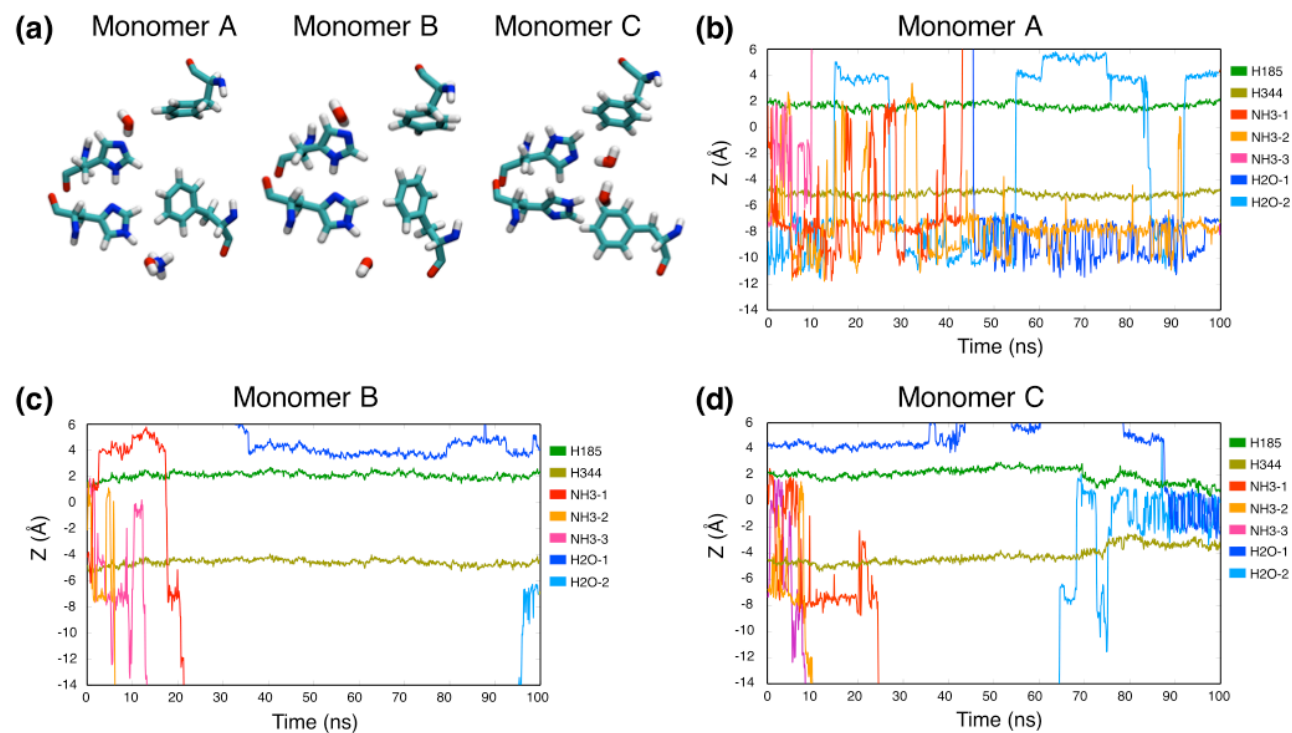


**Figure 3.5** Simulation of RhCG performed with three ammonia molecules initially bound to each pore. a) Configuration of the pore at the end of the simulation for all three monomers. b-d) Positions along the  $Z$ -axis of ammonia and water molecules in the pore of monomers A, B and C.  $Z=0$  corresponds to the center of mass of the protein. A few ammonia and water molecules are seen going back and forth in monomer A. No such transition is seen in monomer B. In monomer C a configuration is observed in which F74 is tilted down, allowing for two water molecules to occupy the pore.

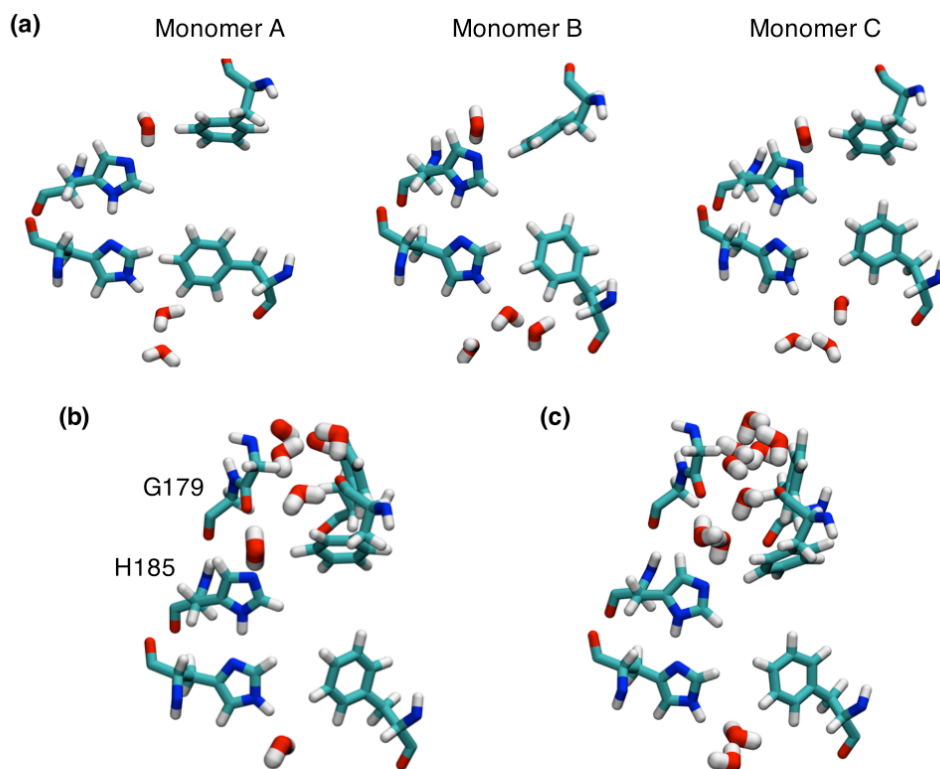


**Figure 3.6** Simulation of RhCG started with empty pores. a) Final configuration of the molecules in the pore for each monomer after 100 ns of simulation. All three pores remained empty, while a water molecule was seen above His185 at the position of a crystallographic water (see Figure 3.1). b-c) Water molecules are observed in greater number in the upper part of the pore, forming a discontinuous (b) or continuous (c) chain. The presence of these water molecules suggests that an  $\text{NH}_4^+$  molecule from the extra-cellular bulk could reach His185

### 3.3.5 Simulation of AmtB and RhCG mutants

The simulations reported above suggest that residue Phe74 prevents the formation of a stable water chain in the pore of RhCG. Sequence and structure alignments indicate that residue Phe74 in RhCG corresponds to residue Ile28 in AmtB (14). We hypothesized that amino acids at these positions are determinant for the formation or absence of a water chain in the pore lumen and that mutating the amino acids could confer the properties of one transporter to the other. We thus simulated both the I28F mutant of AmtB and F74I mutant of RhCG with the pore lumens initially empty. For most of the AmtB I28F mutant simulation, two

water molecules are present in the pore (Figure 3.7a). As illustrated by the density profile in Figure 3.4, the presence of the phenylalanine does not on its own prevent water molecules from occupying the pore, but it significantly decreases the water density in its lower part (arrow on Figure 3.4) and by the same occasion the probability of observing a continuous chain of water. The hydration of the upper part of the pore seems to be favored by the polar N $\epsilon$  atom of His168, which faces the pore lumen and help stabilizing a water molecule. On the other hand, a continuous water chain is observed for most of the simulation time in one monomer of the RhCG F74I mutant (Figure 3.7b). However, the lack of a polar group facing the pore, like His168 N $\epsilon$  in AmtB, seems to limit the overall hydration of the pore (Figure 3.4).

Interestingly, in the related RhAG protein, mutation of the equivalent phenylalanine residue to a serine (F65S) is associated with overhydrated hereditary stomatocytosis (OHSt) of red cells, which is a hemolytic anemia characterized by monovalent cation leaks (33,34). We have performed a 100-ns long simulation of the RhCG F74S mutant. In all three monomers water molecules occupy the pore in large enough amount to potentially accommodate a cation (Figure 3.7c). The pore of the RhCG F74S mutant is more hydrophilic than that of wild-type AmtB (Figure 3.4), and stabilizes water molecules through a distinct hydrogen-bonding scaffold (see also Figure 3.14). In conclusion, the presence of a phenylalanine in the pore of RhCG at the level of the histidine dyad has a direct impact on the hydration of the pore. Moreover, the histidine residues on the extra-cellular side (His168 in AmtB and His185 in RhCG) do not have the same environment and favor different hydration patterns of the pore. In RhCG, His185 contributes to the stabilization of water molecules at the level of the two external phenylalanine residues and not of the pore lumen below the phenylalanines; it is the opposite for His168 in AmtB.

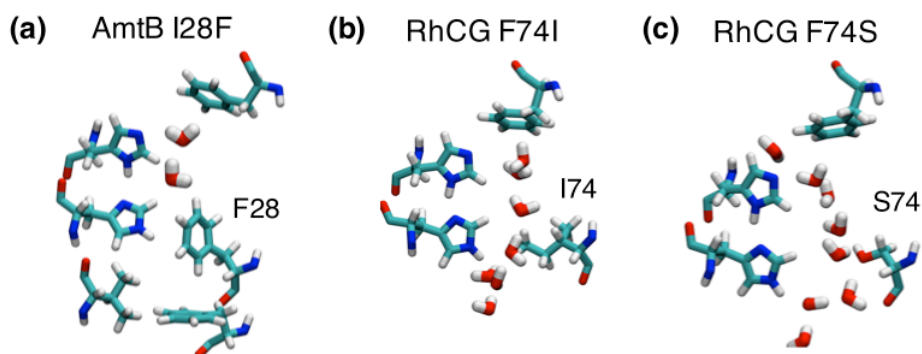


**Figure 3.7** Representative configurations from the AmtB I28F, RhCG F74I, and RhCG F74S mutant simulations. a) In the pore of the I28F mutant of AmtB a constriction at the level of His318 and Phe28 prevents the formation of a water wire. Water molecules are however frequently seen in the upper part of the pore. b) Reciprocally, in RhCG, replacing Phe74 by an isoleucine residue allows the formation of a water wire spanning the whole pore lumen. This configuration is often observed but not as frequently as in AmtB WT. c) Such water chain is more frequently observed in the pore of RhCG F74S, where water molecules are even more stable and numerous than in AmtB WT.

### 3. 4 Discussion

To better understand the transport mechanism in the related but functionally different AmtB and RhCG transporters, we have performed simulations under different occupancy states of the pore of both proteins. The simulations and free energy calculations show that, contrary to what is often assumed, the pore of the AmtB protein is more likely to be occupied by water molecules than ammonia. Because the concentration of water is much larger than that of ammonia, the probability of finding a water molecule at any binding site of the pore is at least  $2.6 \times 10^3$  times that of an ammonia molecule according to our estimates (using the binding energy differences from Table 3.1 and assuming an  $\text{NH}_3$  concentration of 1 mM). The low binding affinity of the pore for ammonia molecules — comparable to that for water molecules— combined with the low concentration of ammonia implies that the permeation in AmtB cannot be described as a single file diffusion of ammonia, as it was proposed on the basis of X-ray diffraction data (7). The presence of electronic density in the pore of AmtB observed in crystals grown without ammonium salt supports the idea that the pore lumen can be occupied by water molecules (8,15). As was shown previously, these water molecules contribute to the stabilization of  $\text{NH}_4^+$  in site S2, from where it can spontaneously transfer a proton to His168 and diffuse as  $\text{NH}_3$  (16). The present work confirms that a chain of water can transiently form in the pore of AmtB when the histidine dyad is in its reverse protonation state. Such chain could serve as a proton wire from His168 to His318, allowing for the reset of the histidine dyad protonation state in an electrogenic transport involving the co-transport of  $\text{NH}_3$  and  $\text{H}^+$  (16).

Our simulations of RhCG have shown that  $\text{NH}_3$  can diffuse freely in and out of the pore, in agreement with free energy calculations performed on Rh50, another Rhesus transporter of known structure (35). In contrast with AmtB, the water occupancy in the pore is much less in RhCG. The presence of a phenylalanine, strongly conserved in the Rh protein family, occupies a large portion of the pore at the level of the histidine dyad and prevents the formation of a stable water chain. This residue is however not the only determinant of the pore hydration. The fact that the polar nitrogen of His185 is pointing towards the extra-cellular bulk rather than towards the pore lumen, like in AmtB, seems to also contribute to the reduction of the hydrophilicity of the pore. If His185 has access

to water molecules coming from the extra-cellular bulk, it is less likely to be available for interaction with water in the hydrophobic pore. Thus, the electrogenic transport mechanism proposed for AmtB may not apply to RhCG, in line with the generally accepted idea that Rh proteins sustain an electroneutral transport of ammonia. Interestingly, the RhCG mutant F74S (and to a lesser extent F74I) leads to a higher hydration of the pore and the formation of water chain at the level of the histidine dyad similar to the one observed in AmtB. We surmise that these mutants could potentially sustain electrogenic transport, though we have not attempted here a full description of the energetics underlying the permeation mechanism. The increased hydration of the pore as observed in the simulation of RhCG F74S can potentially explain the permeation of monovalent cations reported for the homologous RhAG F65S mutant, which is characteristic of overhydrated stomatocytic red blood cells (33,34).

The transport mechanism in wild-type RhCG remains unresolved but our simulations suggest some elements of answer. Contrary to what is observed in AmtB, the upper part of the RhCG pore, at the level of Phe130 and Phe235, is partially hydrated, even allowing a continuous chain of water molecules to form between His185 and the extra-cellular water bulk (Figure 3.6c). His185 seems to be optimally placed to accept a proton from an incoming  $\text{NH}_4^+$ , which could further diffuse down the pore as  $\text{NH}_3$ . Further investigation will be required to elucidate the complete permeation mechanism in RhCG. Nevertheless, our simulations and free energy calculations suggest that small variations in the sequence of ammonium transport proteins, notably at the level of their pore lumen, might have important functional consequences.

### 3.5 Methods

#### 3.5.1 Simulation systems

The crystal structure from PDB entry 1U7G was used for the simulations of AmtB (7). Residues Ser68, Pro126 and Leu255 were mutated to the corresponding amino acids in the wild-type (WT) sequence (F68, S126 and K255). Two protonation states for the histidine dyad His168/His318 were considered. In the first protonation state, hydrogen atoms are positioned on N $\delta$  of His168 and N $\epsilon$  of His318. In the second protonation state, hydrogen atoms are on N $\epsilon$  of His168 and N $\delta$  of His318. Membrane-protein systems were built using the CHARMM-GUI web service (17). A membrane bilayer composed of 289 dimyristoylphosphatidylcholine (DMPC) lipids was assembled around the trimeric AmtB structure and solvated with more than 20,000 TIP3P water molecules. Ions (55 K<sup>+</sup> and 61 Cl<sup>-</sup>) were added to reproduce a 0.15 M KCl concentration and to obtain a neutral system. The tetragonal unit cell of 114  $\times$  114  $\times$  90  $\text{\AA}^3$  contains about 120,000 atoms.

The RhCG system was built following the same procedure, using PDB entry 3HD6. The structure of two missing loops (residues 35-52 and 362-383) was modeled using cyclic coordinate descent (CCD) loop modeling method (18) implemented in the Rosetta program (9). The histidine dyad in the pore is neutral with hydrogen atoms positioned on N $\delta$  of His185 and N $\epsilon$  of His344. (By analogy with AmtB, this protonation state is assumed to be the functional form of the pore.) The RhCG trimer is surrounded by a membrane bilayer of 321 DMPC lipids, solvated by 21,407 TIP3P water molecules and 0.15 M KCl. The system containing 121,237 atoms holds in an orthogonal box of 115  $\times$  122  $\times$  83  $\text{\AA}^3$ . The systems for the AmtB and RhCG mutants were constructed by changing the side-chain atoms of the targeted amino acid in the equilibrated wild-type systems.

All systems were equilibrated using CHARMM (version c34b2) (19), and simulated for 100 ns using the NAMD simulation package (version 2.7b4) (20) with the CHARMM 27 force field (21). Particle-Mesh Ewald method (22) was applied for the calculation of electrostatic interactions, using a grid spacing of 1  $\text{\AA}$ . The cut-off distance for van der Waals interactions was taken at 12  $\text{\AA}$  with a switching function starting at 10  $\text{\AA}$ . Time step for the integration of the motion

was set to 1 fs. Short-range non-bonded interactions were calculated every 2 steps and long-range interactions every 4 steps. Simulations were performed in an isothermal-isobaric ensemble with a pressure of 1 atm and a temperature of 315 K. Parameters for ammonia ( $\text{NH}_3$ ) were taken from the OPLS model (23). According to this model, the free energy of solvation of  $\text{NH}_3$  in TIP3P water molecules is 2.7 kcal/mol higher than that of  $\text{H}_2\text{O}$ , comparable to the experimental free energy difference of 2.0 kcal/mol (24). If the small difference has an impact on the simulations, it would bias our results toward a higher occupancy probability of  $\text{NH}_3$  in the hydrophobic pore.

### 3.5.2 Free-Energy Perturbation Calculations

Free-energy perturbation (FEP) simulations (25) were used to calculate the free energy difference between water and ammonia for different occupancy states of the AmtB pore. For these FEP calculations performed with NAMD, the molecular system contains a hybrid residue representing simultaneously both an ammonia and a water molecule. Interactions of the atoms of this residue with surrounding atoms are scaled by a thermodynamic parameter  $\lambda$ . When  $\lambda = 0$  only the interactions of the water molecule with surrounding atoms are considered, while only the interactions of ammonia molecule are considered when  $\lambda = 1$ . A linear combination of these interaction energies is applied when  $\lambda$  is between 0 and 1. There is no interaction between the ammonia and water molecules, except that their heavy atoms are linked by a harmonic tether with a force constant of 500 kcal/mol $\cdot\text{\AA}^2$  (26).

The reaction coordinate ( $\lambda$ ) in the FEP simulations is discretized into windows of width 0.1 for  $\lambda$  ranging from 0.1 to 0.9 and these windows were simulated for 200 ps (first 20 ps for equilibration). At the end points,  $\lambda$  was progressively increased with windows at [0, 0.001, 0.01, 0.05, and 0.95, 0.99, 0.999, 1] that were simulated for 100 ps (first 10 ps for equilibration). For each perturbation calculation, the combined forward and backward simulations amounted to a total simulation time of 4.8 ns. Free energy differences and statistical errors were calculated by combining the forward and backward configurational ensembles using the Bennett acceptance ratio (BAR) method as implemented in the ParseFEP toolkit (27) of the VMD visualization platform (28).



FEP simulations were performed using a monomeric AmtB system, containing 185 DMPC, 33 K<sup>+</sup> and 35 Cl<sup>-</sup>, for a total of about 67,000 atoms (box size 92 × 78 × 92 Å<sup>3</sup>). In the FEP simulations, the hybrid residue and water molecules were restrained along the z-coordinate (normal to the membrane) to maintain them in a single file. For each site, a harmonic flat-bottom restraint defined in function of the distance to the center of mass of the C $\alpha$  of His168 and His318 was applied. Fig. S1 illustrates the boundaries beyond which the restraint is effective for each site. The perturbation calculations in bulk water were performed on a system containing 284 water molecules with dimensions of 20 × 20 × 20 Å<sup>3</sup> at a constant pressure of 1 atm.

### 3. 6 References

1. Ninnemann, O., Jauniaux, J. C., and Frommer, W. B. (1994) Identification of a high affinity NH<sub>4</sub><sup>+</sup> transporter from plants, *EMBO J* 13, 3464-3471.
2. Siewe, R. M., Weil, B., Burkovski, A., Eikmanns, B. J., Eikmanns, M., and Krämer, R. (1996) Functional and genetic characterization of the (methyl)ammonium uptake carrier of *Corynebacterium glutamicum*, *J Biol Chem* 271, 5398-5403.
3. Marini, A. M., Soussi-Boudekou, S., Vissers, S., and Andre, B. (1997) A family of ammonium transporters in *Saccharomyces cerevisiae*, *Mol Cell Biol* 17, 4282-4293.
4. Ludewig, U., von Wirén, N., and Frommer, W. B. (2002) Uniport of NH<sub>4</sub><sup>+</sup> by the root hair plasma membrane ammonium transporter LeAMT1;1, *J Biol Chem* 277, 13548-13555.
5. Ripoche, P., Bertrand, O., Gane, P., Birkenmeier, C., Colin, Y., and Cartron, J. P. (2004) Human Rhesus-associated glycoprotein mediates facilitated transport of NH<sub>3</sub> into red blood cells, *Proc Natl Acad Sci U S A* 101, 17222-17227.
6. Mouro-Chanteloup, I., Cochet, S., Chami, M., Genetet, S., Zidi-Yahiaoui, N., Engel, A., Colin, Y., Bertrand, O., and Ripoche, P. (2010) Functional reconstitution into liposomes of purified human RhCG ammonia channel, *PLoS One* 5, e8921.
7. Khademi, S., O'Connell, J., Remis, J., Robles-Colmenares, Y., Miercke, L. J., and Stroud, R. M. (2004) Mechanism of ammonia transport by Amt/MEP/Rh: structure of AmtB at 1.35 Å, *Science* 305, 1587-1594.
8. Zheng, L., Kostrewa, D., Bernèche, S., Winkler, F. K., and Li, X. D. (2004) The mechanism of ammonia transport based on the crystal structure of AmtB of *Escherichia coli*, *Proc Natl Acad Sci U S A* 101, 17090-17095.
9. Wang, C., Bradley, P., and Baker, D. (2007) Protein--protein docking with backbone flexibility, *Journal of molecular biology* 373, 503-519.
10. Soupene, E., He, L., Yan, D., and Kustu, S. (1998) Ammonia acquisition in enteric bacteria: physiological role of the ammonium/methylammonium transport B (AmtB) protein, *Proc Natl Acad Sci U S A* 95, 7030-7034.

11. Javelle, A., Lupo, D., Li, X. D., Merrick, M., Chami, M., Ripoche, P., and Winkler, F. K. (2007) Structural and mechanistic aspects of Amt/Rh proteins, *J Struct Biol* 158, 472-481.
12. Fong, R. N., Kim, K. S., Yoshihara, C., Inwood, W. B., and Kustu, S. (2007) The W148L substitution in the Escherichia coli ammonium channel AmtB increases flux and indicates that the substrate is an ion, *Proc Natl Acad Sci U S A* 104, 18706-18711.
13. Gruswitz, F., Chaudhary, S., Ho, J. D., Schlessinger, A., Pezeshki, B., Ho, C. M., Sali, A., Westhoff, C. M., and Stroud, R. M. (2010) Function of human Rh based on structure of RhCG at 2.1 Å, *Proc Natl Acad Sci U S A* 107, 9638-9643.
14. Zidi-Yahiaoui, N., Callebaut, I., Genetet, S., Le Van Kim, C., Cartron, J. P., Colin, Y., Ripoche, P., and Mouro-Chanteloup, I. (2009) Functional analysis of human RhCG: comparison with E. coli ammonium transporter reveals similarities in the pore and differences in the vestibule, *Am J Physiol Cell Physiol* 297, C537-C547.
15. Lamoureux, G., Klein, M. L., and Bernèche, S. (2007) A stable water chain in the hydrophobic pore of the AmtB ammonium transporter, *Biophys J* 92, L82-L84.
16. Wang, S., Orabi, E. A., Baday, S., Bernèche, S., and Lamoureux, G. (2012) Ammonium transporters achieve charge transfer by fragmenting their substrate, *J Am Chem Soc* 134, 10419-10427.
17. Jo, S., Kim, T., Iyer, V. G., and Im, W. (2008) CHARMM-GUI: a web-based graphical user interface for CHARMM, *J Comput Chem* 29, 1859-1865.
18. Canutescu, A. A., and Dunbrack, R. L. (2003) Cyclic coordinate descent: A robotics algorithm for protein loop closure, *Protein Sci* 12, 963-972.
19. Brooks, B. R., Brooks, C. L., Mackerell, A. D., Nilsson, L., Petrella, R. J., Roux, B., Won, Y., Archontis, G., Bartels, C., Boresch, S., Caflisch, A., Caves, L., Cui, Q., Dinner, A. R., Feig, M., Fischer, S., Gao, J., Hodoseck, M., Im, W., Kuczera, K., Lazaridis, T., Ma, J., Ovchinnikov, V., Paci, E., Pastor, R. W., Post, C. B., Pu, J. Z., Schaefer, M., Tidor, B., Venable, R. M., Woodcock, H. L., Wu, X., Yang, W., York, D. M., and Karplus, M. (2009) CHARMM: the biomolecular simulation program, *J Comput Chem* 30, 1545-1614.

20. Phillips, J. C., Braun, R., Wang, W., Gumbart, J., Tajkhorshid, E., Villa, E., Chipot, C., Skeel, R. D., Kalé, L., and Schulten, K. (2005) Scalable molecular dynamics with NAMD, *J Comput Chem* 26, 1781-1802.
21. MacKerell Jr, A. D., Bashford, D., Bellott, M., Dunbrack Jr, R. L., Evanseck, J. D., Field, M. J., Fischer, S., Gao, J., Guo, H., and Ha, S. (1998) All-atom empirical potential for molecular modeling and dynamics studies of proteins, *The Journal of Physical Chemistry B* 102, 3586-3616.
22. Essmann, U., Perera, L., Berkowitz, M. L., Darden, T., Lee, H., and Pedersen, L. G. (1995) A smooth particle mesh ewald method, *J Chem Phys* 103, 8577-8593.
23. Gao, J., Xia, X., and George, T. F. (1993) Importance of bimolecular interactions in developing empirical potential functions for liquid ammonia, *The Journal of Physical Chemistry* 97, 9241-9247.
24. Ben-Naim, A., and Marcus, Y. (1984) Solvation thermodynamics of nonionic solutes, *The Journal of chemical physics* 81, 2016.
25. Zwanzig, R. W. (1954) High-temperature equation of state by a perturbation method. I. Nonpolar gases. , *J Chem Phys* 22, 1420-1426.
26. Orabi, E. A., and Lamoureux, G. (2012) Cation-pi and pi-pi Interactions in Aqueous Solution Studied Using Polarizable Potential Models, *journal of chemical theory and computation* 8, 182-193.
27. Liu, P., Dehez, F., Cai, W., and Chipot, C. J. (2012) A toolkit for the analysis of free-energy perturbation calculations, *Journal of Chemical Theory and Computation* 8, 2606-2616.
28. Humphrey, W., Dalke, A., and Schulten, K. (1996) VMD: visual molecular dynamics, *J Mol Graph* 14, 33-8, 27-8.
29. Luzhkov, V. B., Almlöf, M., Nervall, M., and Aqvist, J. (2006) Computational study of the binding affinity and selectivity of the bacterial ammonium transporter AmtB, *Biochemistry* 45, 10807-10814.
30. Lin, Y., Cao, Z., and Mo, Y. (2006) Molecular dynamics simulations on the Escherichia coli ammonia channel protein AmtB: mechanism of ammonia/ammonium transport, *J Am Chem Soc* 128, 10876-10884.

31. Ullmann, R. T., Andrade, S. L., and Ullmann, G. M. (2012) Thermodynamics of transport through the ammonium transporter Amt-1 investigated with free energy calculations, *J Phys Chem B* 116, 9690-9703.
32. Javelle, A., Severi, E., Thornton, J., and Merrick, M. (2004) Ammonium sensing in Escherichia coli. Role of the ammonium transporter AmtB and AmtB-GlnK complex formation, *J Biol Chem* 279, 8530-8538.
33. Bruce, L. J., Guizouarn, H., Burton, N. M., Gabillat, N., Poole, J., Flatt, J. F., Brady, R. L., Borgese, F., Delaunay, J., and Stewart, G. W. (2009) The monovalent cation leak in overhydrated stomatocytic red blood cells results from amino acid substitutions in the Rh-associated glycoprotein, *Blood* 113, 1350-1357.
34. Genetet, S., Ripoché, P., Picot, J., Bigot, S., Delaunay, J., Armari-Alla, C., Colin, Y., and Mouro-Chanteloup, I. (2012) Human RhAG ammonia channel is impaired by the Phe65Ser mutation in overhydrated stomatocytic red cells, *Am J Physiol Cell Physiol* 302, C419-C428.
35. Hub, J. S., Winkler, F. K., Merrick, M., and de Groot, B. L. (2010) Potentials of mean force and permeabilities for carbon dioxide, ammonia, and water flux across a Rhesus protein channel and lipid membranes, *J Am Chem Soc* 132, 13251-13263.

### 3.7 Appendix

#### 3.7.1 Figures

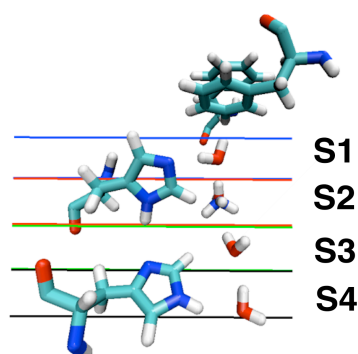


**Figure 3.8** Boundaries along the Z-axis of the flat-bottom restraints applied to water and ammonia molecules during the free energy perturbation calculations. The harmonic potential is effective only when the molecule is outside the region delimited by the two horizontal planes: blue (S1), red (S2), green (S3), and black (S4). The positions of these boundaries are defined relative to the center of mass of the Ca's of His168 and His318.

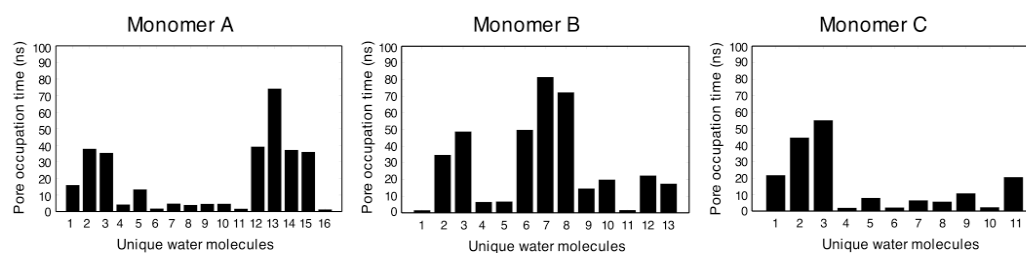


**Figure 3.9** Residence time for water molecules in the pore of AmtB WT. The data is taken from a simulation initiated with three water molecules bound to the pore of each monomer. The bars show the time that each water molecule has spent in the pore, in order of appearance. The three first water molecules in each monomer were present in the pore at the beginning of the simulation. At least three water molecules are found in the pore of each monomer at the end of the simulation.

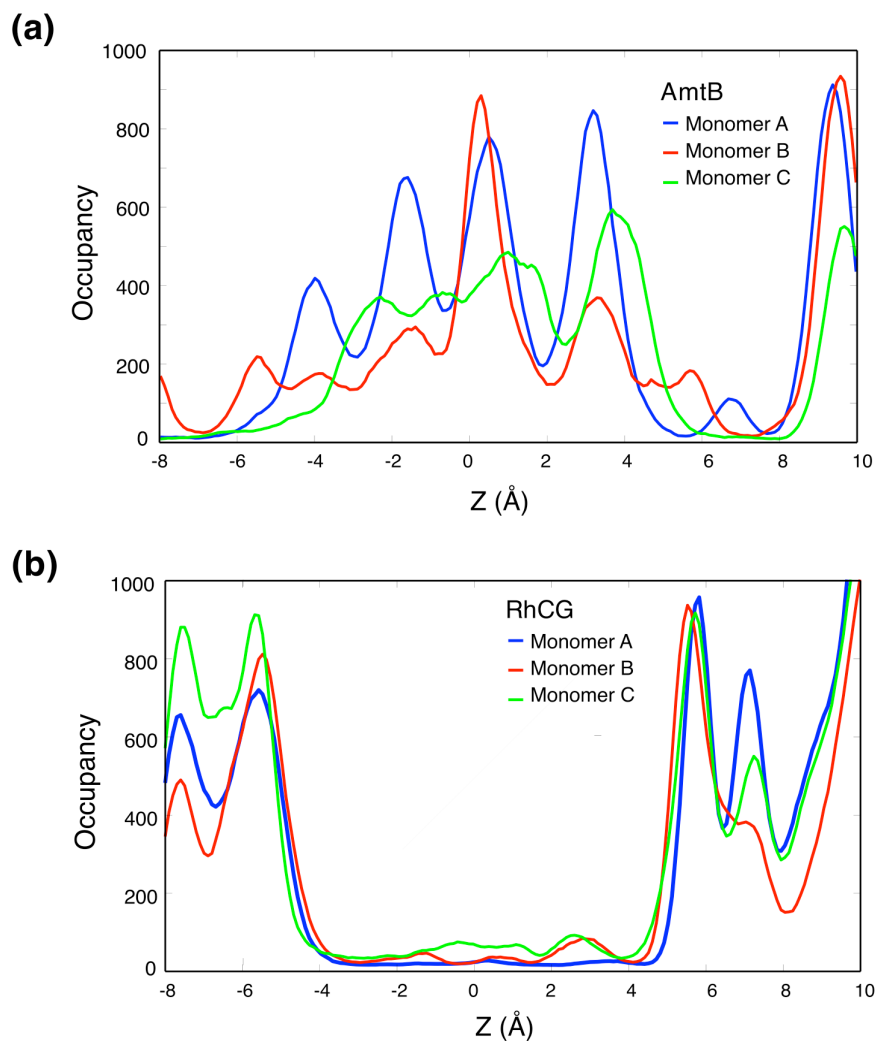


**Figure 3.10** Water occupancy in the pore of each monomer of AmtB WT (a) and RhCG WT (b). For both proteins, histograms were calculated from 100-ns long simulations initiated with empty pores. All monomers of AmtB show water at the level of the two histidine residues (i.e.  $-3.5 \text{ \AA} < Z < 3.5 \text{ \AA}$ ), while little water is seen in any monomer of RhCG.

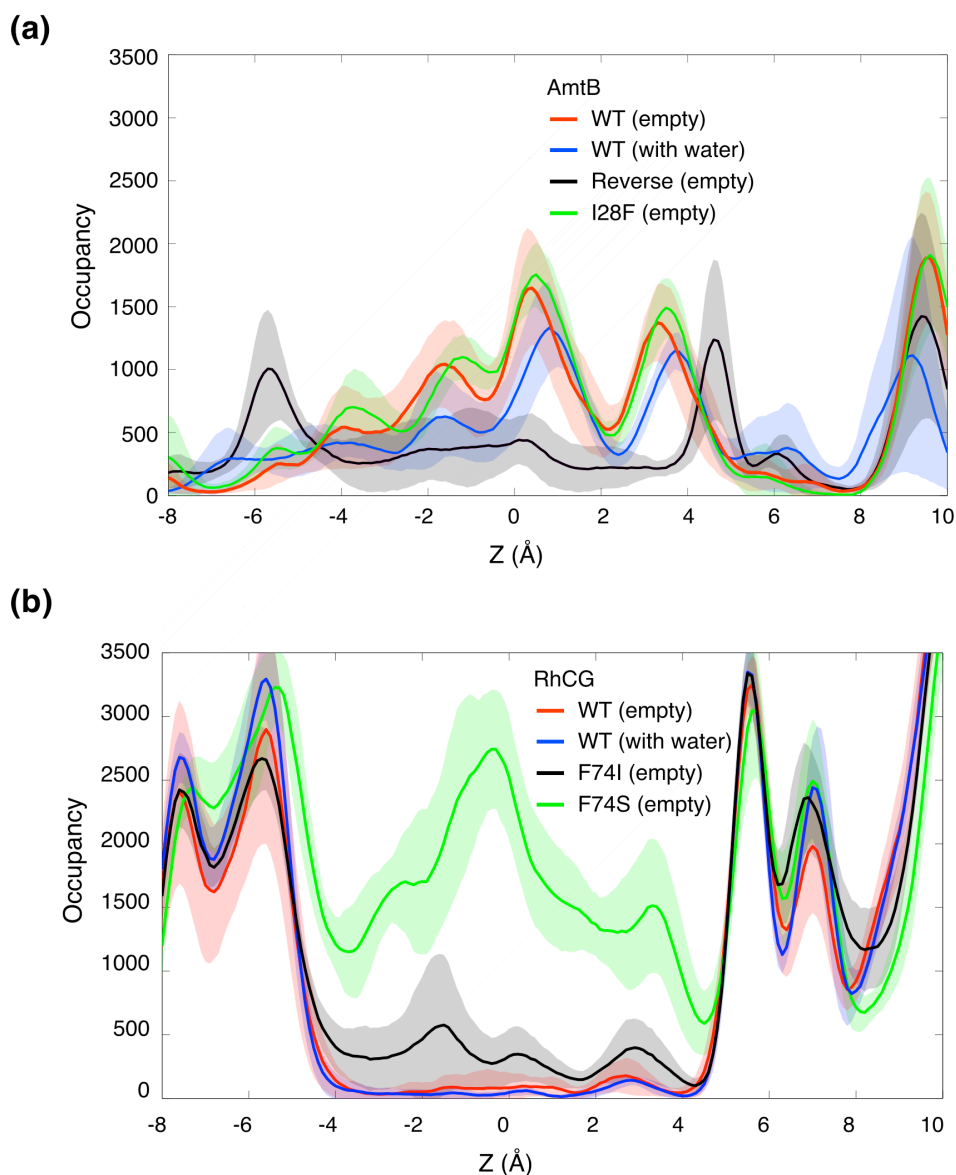


**Figure 3.11** Water occupancy in the pore of the different constructs of (a) AmtB and (b) RhCG. In all cases, histograms were calculated from 100-ns long simulations, and averaged over the three monomers. The simulations were initiated with empty pores, or with water molecules in the pores as indicated. Each of the trajectories was split in 5 intervals providing as many histograms forming an ensemble from which a standard deviation  $\sigma(Z)$  was calculated. The occupancy number are plotted with an envelop corresponding to plus/minus the standard deviation. The Z position is calculated relative to the center of mass of the alpha-carbons of the two histidines residues lining the pore.



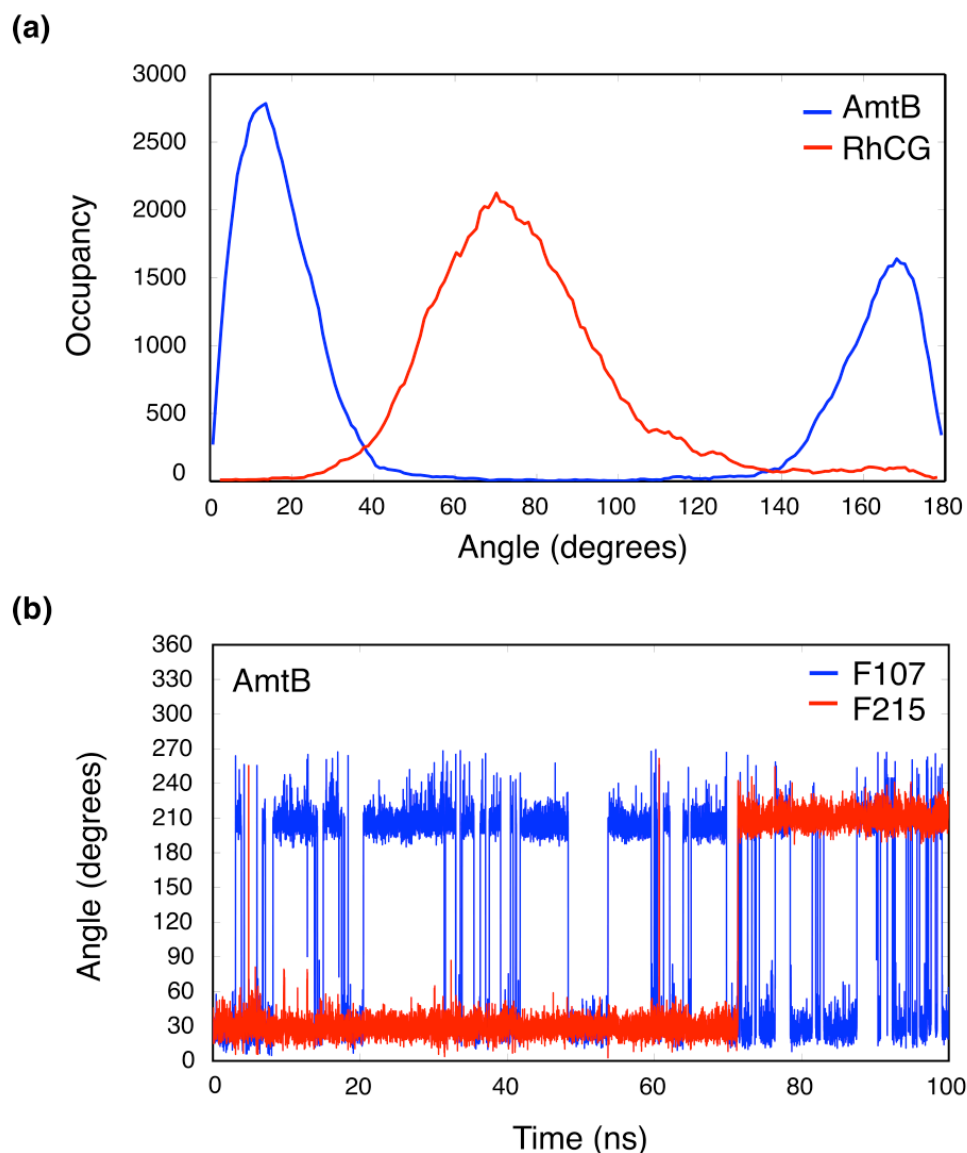


**Figure 3.12** a) Relative orientation of the aromatic groups of two phenylalanine residues in AmtB (Phe107/Phe215) and RhCG (Phe130/Phe235) proteins. The distributions of the angle between the normal vectors of the two phenyl rings show that the two residues are mostly seen in the conformations revealed by X-ray crystallography, i.e. perpendicular for RhCG and parallel for AmtB. The occupancy units are arbitrary. b) The time series show the angle between the normal vector to the phenyl ring and the Z-axis for residues Phe107 and Phe215 in monomer A of AmtB. Many 180°-flips are seen for Phe107, and only a few for Phe215.

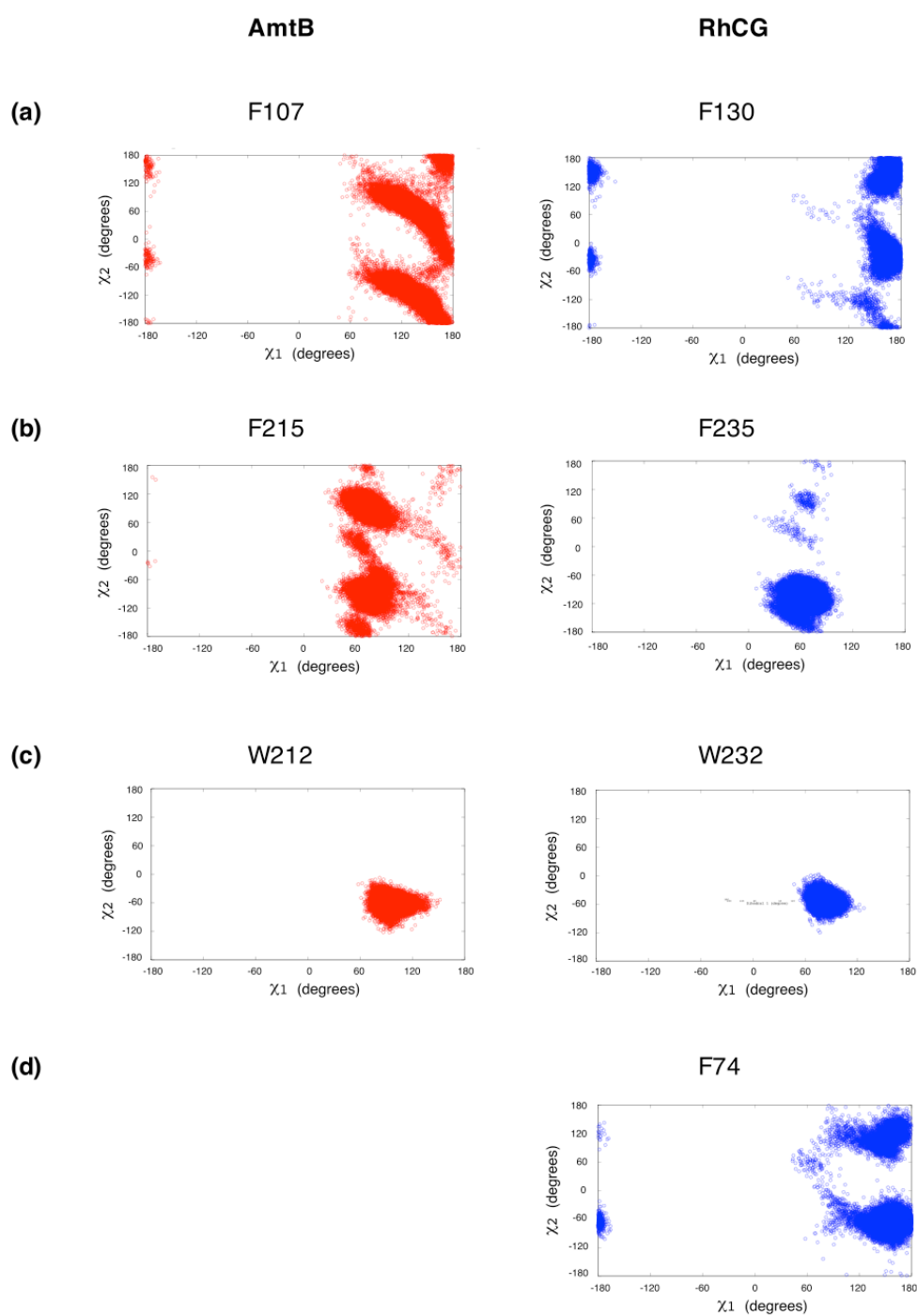


**Figure 3.13** Rotameric states of key aromatics residues around the pore of AmtB WT and RhCG WT.  $\chi_1$  and  $\chi_2$  dihedral angles are plotted for the two phenylalanine residues on the extracellular side of the pore (a, b), the tryptophan lining the pore (c), and the phenylalanine exclusively found in the pore of Rh proteins (d). Graphs in (a) and (b) show that the phenylalanines at the entrance of

the pore are more mobile, notably in AmtB. The tryptophan lining the pore is quite stable in both AmtB and RhCG (c). The phenylalanine F74 in the pore of RhCG can rotate on itself by  $180^\circ$  ( $\chi_2$ ) and twist by about  $60^\circ$  ( $\chi_1$ ).

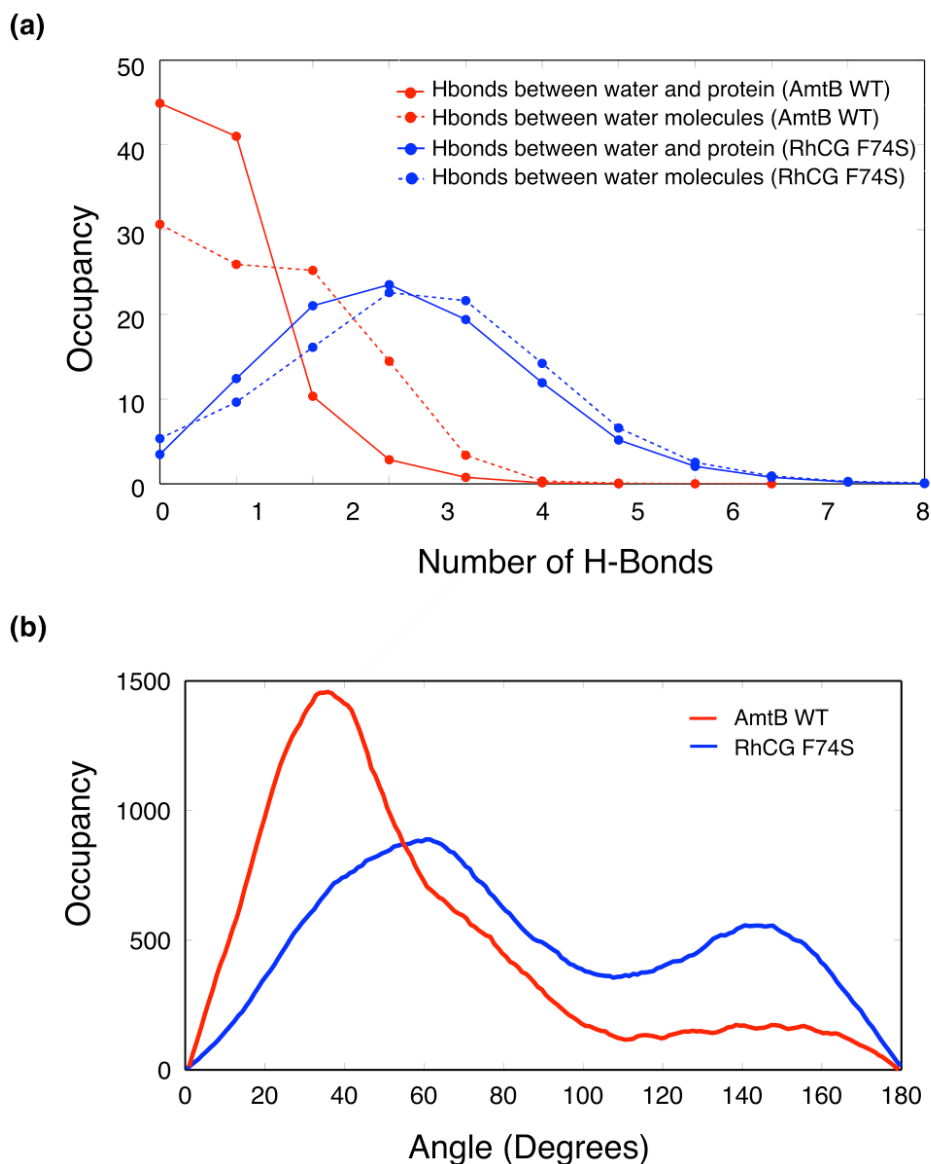


**Figure 3.14** Structural order of the water molecules in the pore of AmtB WT and RhCG F74S. a) Histograms of the number of hydrogen bonds formed between water molecules in the pore and the protein (solid lines) and among the water molecules (dashed lines). Occupancy in panel (a) is defined as the percentage of the total number of frames. b) Distributions of the angles between the dipole moments of the pore water molecules and the Z-axis. The data show that the water

chain in the pore of AmtB is well ordered, with the negative pole of the water molecules (the oxygen atom) preferentially pointing downward. Water molecules in RhCG F74S have more diverse orientations. Occupancy units in panel (b) are arbitrary.

## **Chapter 4**

### **THE MECHANISM OF AMMONIUM TRANSPORT IN RHCg PROTEIN**

#### 4.1 Abstract

The Rh family of membrane proteins facilitates the diffusion of ammonium across cellular membranes. While functional data suggest that human rhesus (Rh) proteins transport neutral ammonia ( $\text{NH}_3$ ), the details of the transport mechanism have not been elucidated. Here, we present a novel mechanism for electroneutral ammonium transport in RhCG protein using molecular and quantum mechanical calculations. We show that  $\text{NH}_4^+$  is recruited and binds with high affinity to a conserved histidine residue (His185) to which it transfers a proton. The resulting  $\text{NH}_3$  molecule diffuses down a hydrophobic pore, overcoming small free energy barriers. The excess proton bound to His185 is circulated back to the extracellular vestibule through a network of H-bonds, which involves a highly conserved and functionally important aspartic acid (Asp177). QM/MM simulations illustrate the feasibility of the proton transfer from His185 to Asp177. The protonated Asp177 is then found to be exposed to extracellular bulk water where the proton can be released. Our simulations reveal that a serine residue (Ser181) plays an important role in the function of RhCG, bridging His185 to Asp177 through a H-bond network. We suggest that the permeation mechanism in Rh proteins share many features with that proposed for AmtS except that the excess proton is transported across the membrane in AmtS and shuffled back to the recruitment side in Rh proteins.

## 4.2 Introduction

Ammonium is a nitrogen source for bacteria, yeast and plants, where it is transported by the Amt/Mep family of proteins at low ammonium concentrations (1-4). In mammals, ammonium is notably produced in great quantity during glutamine metabolism and needs to be excreted due to its toxicity at high concentrations. Erythrocytic RhAG and non-erythrocytic RhBG and RhCG from the Rh family of proteins mediate ammonium transport in mammals (5-6).

Functional studies have strongly suggested that Amt proteins transport charged ammonium ( $\text{NH}_4^+$ ) whereas Rh proteins transport its neutral form, ammonia ( $\text{NH}_3$ ) (1-6). However, the elucidation of different structures of Amt and Rh proteins, all revealing a hydrophobic pore that prevents the translocation of  $\text{NH}_4^+$ , has suggested that both protein families transport ammonia {7, 8, 16, 38, 39}.

Amt and Rh proteins share many structural features but important differences are notable. Like in AmtB from *E. coli*, the hydrophobic pore of RhCG is lined with two histidines (His185 and His344), and two phenylalanines (Phe130 and Phe235) are found on the extracellular side of this pore. The conformation of these two phenylalanine residues is however different in the two protein architectures. In AmtB they create a barrier that notably blocks water access to the histidine dyad, while in RhCG they line a hydrophilic pore reaching down to His185 (Figure 4.1a,b). Furthermore, a phenylalanine residue (Phe74) is found at the level of the histidine dyad in RhCG, preventing the formation of a water chain in that region, further differentiating its pore from that of AmtB in which no such residue is found. Our recent study suggests that these structural differences lead to different hydration patterns that are likely to be determinant of the transport mechanisms (40).

There is a consensus that AmtB presents a recruitment site with high binding affinity for  $\text{NH}_4^+$ , which needs to deprotonate for permeation to take place (9-13). There is however a debate on the deprotonation mechanism. It is generally proposed that  $\text{NH}_4^+$  deprotonates on the extracellular side of the pore, allowing for the net transport of  $\text{NH}_3$  (9,11,12). We have rather proposed that  $\text{NH}_4^+$  transfer a proton to the signature histidine dyad, followed by diffusion of  $\text{NH}_3$  down the hydrophobic pore, and the transport of the excess proton through a water wire filling this pore. The overall process results in the net transport of  $\text{NH}_4^+$ , in agreement with the bulk of functional studies on Amt proteins (13).

In the case of Rh proteins, it is generally understood that the transport mechanism simply involves the diffusion of  $\text{NH}_3$  down its gradient (41). Based on free energy calculations, we here propose that Rh proteins, like Amt, recruits  $\text{NH}_4^+$  at a binding sites formed by a signature histidine that capture a proton. We further show that this proton is transferred back to the extracellular side through a network of hydrogen bonds that involves a highly conserved aspartic acid residue (Asp177). Our calculations suggest that in both Amt and Rh proteins, the histidine dyad acts as a proton acceptor. The two classes of proteins are distinguished by the pathway through which the proton is released, resulting in the net transport of  $\text{NH}_4^+$  for Amt and  $\text{NH}_3$  for Rh proteins.

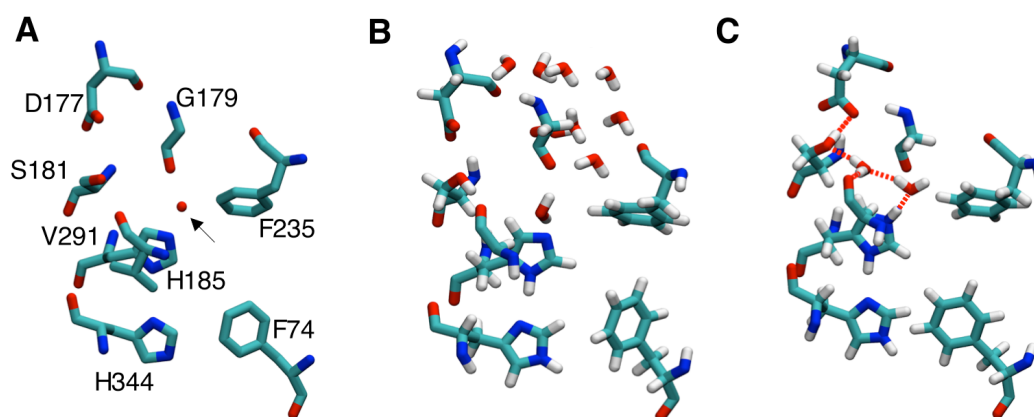


**Figure 4.1** Molecular representations of the RhCG pore. a) The X-ray structure (PDB entry 3HD6) is shown with key residues labeled and a crystallographic water indicated by an arrow. b) A conformation extracted from a MD simulation shows hydration of the pore reaching His185. c) When His185 is protonated a network of hydrogen bonds forms from His185 Ne atom to Asp177 carboxyl group.



## 4.3 Results and Discussion

### 4.3.1 Recruitment of ammonium and proton transfer to His185

By comparison with the AmtB structure, it was suggested that RhCG lacks a recruitment binding site for ammonium at the extracellular vestibule (16,41). However, we have previously shown using molecular dynamics simulations that the extracellular vestibule extends through a continuous hydrated pore reaching a crystallographic water molecule interacting with His185. We investigated the binding of ammonium to this site in the vicinity of His185. We first performed a 50 ns classical molecular dynamics simulations of the RhCG trimer with one  $\text{NH}_4^+$  molecule initially bound to His185 in each pore. In order to equilibrate ammonium at this site it was restrained to stay within 3.5 Å of the N $\epsilon$  atom of His185 and O atom of Gly179 for the first 5 ns of simulation. Through the whole trajectory, the ammonium molecules remain in the vicinity of His185, with which they interact directly or through a water molecule (Figure 4.2). The binding affinities of  $\text{NH}_4^+$  was calculated by alchemically transforming  $\text{NH}_4^+$  into  $\text{H}_2\text{O}$  at this putative recruitment site, while simultaneously performing the opposite transformation in bulk water. The resulting free energy difference of  $-5.5 \pm 0.5$  kcal/mol corresponds to the relative binding free energy of ammonium to the pore. The binding affinity at a corresponding site in AmtB was found to be about -13 kcal/mol (13). The binding affinity difference between the two proteins arises from slightly different coordination schemes. While  $\text{NH}_4^+$  is coordinated by a histidine, a tryptophan, a phenylalanine and a water molecule in AmtB, in RhCG there are little interactions with aromatic amino acids and  $\text{NH}_4^+$  is coordinated by a histidine and two water molecules and oxygen atoms from G179 and N236. The relatively high binding affinity for  $\text{NH}_4^+$  allows for an efficient recruitment, whereas recruiting  $\text{NH}_3$  would be much less efficient because of its lower concentration and lower binding affinity.

Once  $\text{NH}_4^+$  is bound to the recruitment site, it is unlikely to diffuse further down since the pore is highly hydrophobic, as was shown by free energy calculation in a homologous Rh50 channel (41). Using QM/MM simulations we calculated the PMF of the proton transfer from  $\text{NH}_4^+$  to His185. The free energy profile shown in Figure 4.3 reveals a reaction free energy of 2 kcal/mol and a

barrier of 3 kcal/mol. Thus our calculations suggest that  $\text{NH}_4^+$  is recruited at His185 and that a proton can efficiently be exchanged between ammonium and His185.

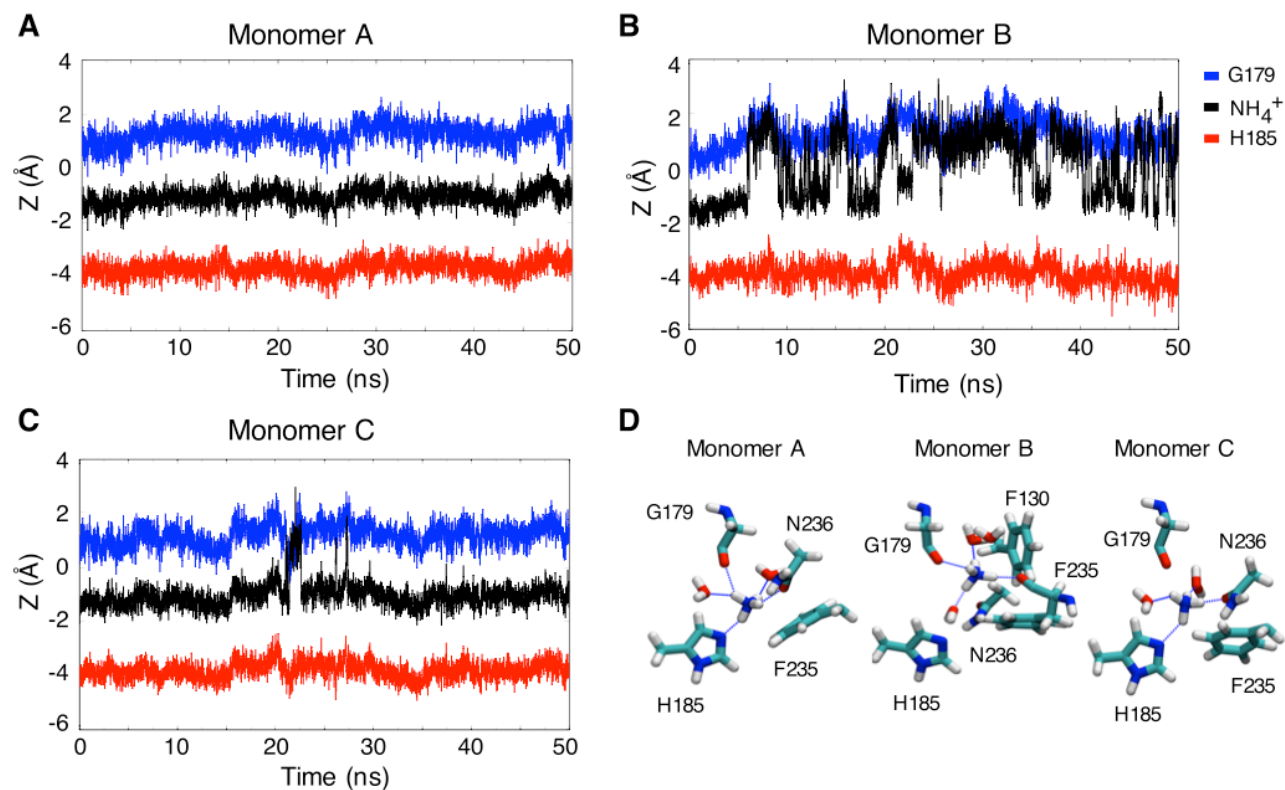


**Figure 4.2** Simulation of RhCG initiated with an ammonium molecule bound to His185 in each pore. a-c) The time series show the position, along the Z-axis, of ammonium in the pore of monomer A (a), monomer B (b) and monomer C (c) over the duration of the simulation. For reference, the positions of Gly179 O and His185 Ne atoms are shown. Z=0 corresponds to the center of mass of Phe130 and Phe235 Ca atoms. d) The conformation of the pore of each monomer is shown at the end of the simulation, highlighting key residues and the ammonium molecule.

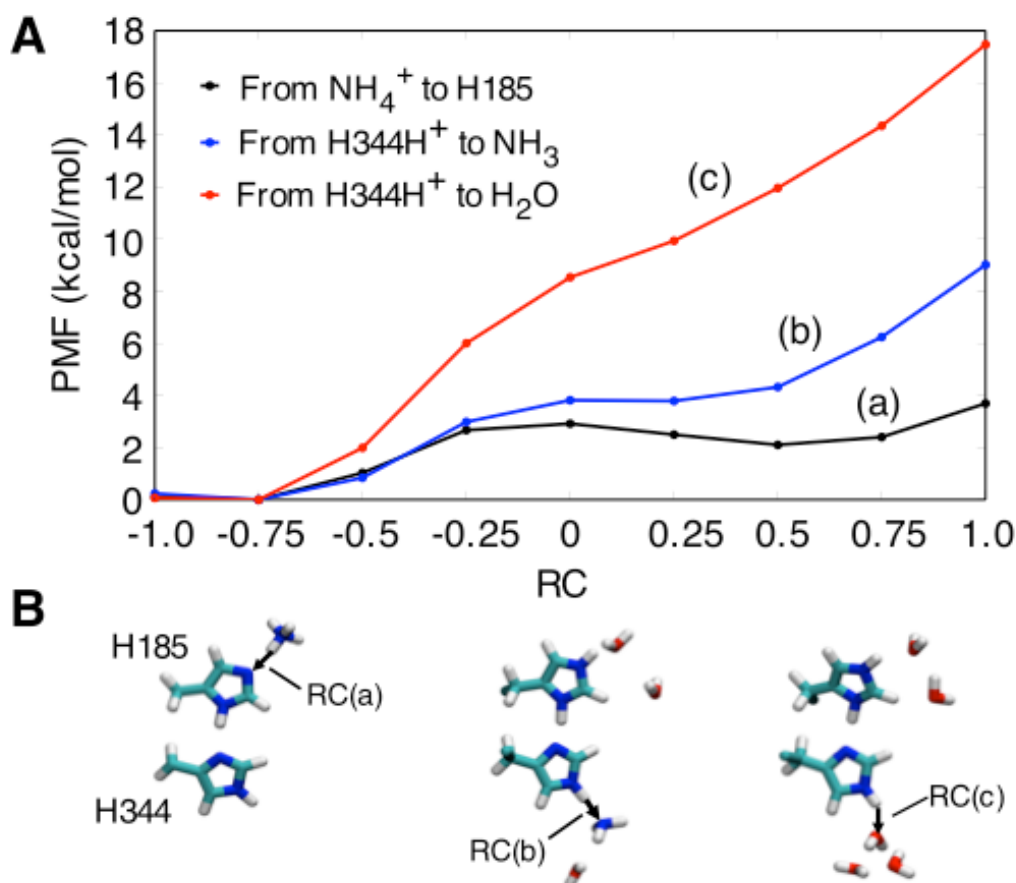


**Figure 4.3** Potentials of mean force (PMFs) obtained from QM/MM simulations for proton transfer reactions occurring in the RhCG pore. The different PMFs correspond to the proton transfer from  $\text{NH}_4^+$  to His185 (black), from His344 $\text{H}^+$  to  $\text{NH}_3$  (blue), and from His344 $\text{H}^+$  to a water molecule (red). The reaction coordinate is defined as  $\text{RC} = d_{\text{Donor-Proton}} - d_{\text{Acceptor-Proton}}$ .

### 4.3.2 Dynamics of ammonia after deprotonation of ammonium

To investigate on the dynamics of ammonia in the pore after deprotonation of ammonium we simulated RhCG trimer with one ammonia molecule initially placed close to the N $\epsilon$  atom of the protonated His185. Ammonia was restrained to stay within 3.5 Å of His185 N $\epsilon$  and G179 O for the first 5 ns of the 100 ns simulation. As illustrated in Figure 4.4, ammonia rapidly moves to the hydrophobic section of the pore at the level of the two signature histidine residues. In monomers A and C, the ammonia molecule diffused pass Phe74 and His344, while in Monomer B it diffused back to the extracellular bulk. The PMF of ammonia diffusing down the pore was calculated using ABF simulations (see Methods). The PMF shown in Figure 4.4d is in line with the observations based

on the unbiased simulations. It further reveals that ammonia is more stable near His185, with free energy barriers of about 2 to 3 kcal/mol opposing the diffusion of  $\text{NH}_3$  toward the intra- or extracellular bulk. Overall, the permeation of ammonia across the pore involves relatively low free energy barriers, in agreement with similar PMF obtained for Rh50 (41).

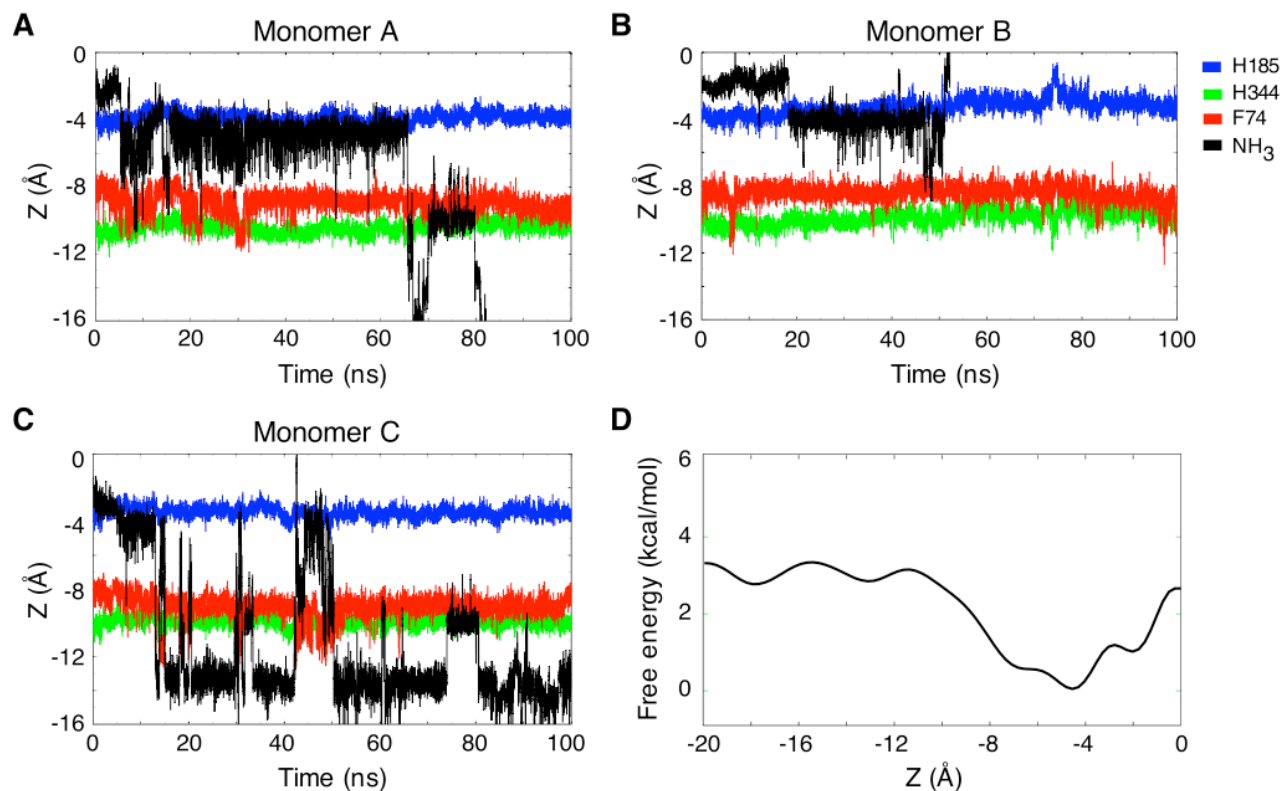


**Figure 4.4** Simulation of RhCG initiated with one ammonia molecules binding to H185 in each pore of the trimer. The time series show the position of ammonia along the pore in monomer A (a), monomer B (b) and monomer C (c) during the simulation. The positions of the His185 and His344 N $\epsilon$  atoms and the center of mass of the aromatic ring of Phe74 is shown as reference. d) The potential of mean force underlying ammonia diffusion in the hydrophobic pore reveals a main free energy barrier of  $\sim 3$  kcal/mol. In all plots,  $Z=0$  corresponds to the center of mass of Phe130 and Phe235 C $\alpha$  atoms.

### 4.3.3 H-bond network linking His185 to Asp177 through water molecules and Ser181

After deprotonation of  $\text{NH}_4^+$  to His185, the proton on His185 has to be transferred either to the intracellular bulk or back to the extracellular bulk to allow the recruitment of a new ammonium molecule. To explore possible proton diffusion pathways, we performed simulations of RhCG monomer in which His185 is protonated. We also further analyzed the simulation of the previous section in which His185 is protonated with an ammonia molecule in its vicinity. In these simulations we observed a network of hydrogen bonds from His185 to Asp177, involving water molecules and Ser181. In the 50 ns simulation of RhCG monomer, two similar H-bond networks between His185 and Asp177 are formed through almost the entire simulation. The first network consists of His185, two water molecules, Ser181 and Asp177, and remains stable up to the 28th ns of the simulation (Figure 4.5, a-b). After 32 ns of simulation, the side chain of Ser181 rotates and allows another water molecule to bridge Asp177 with the rest of the network (Figure 4.5c). In the RhCG trimer simulation, the H-bond network forms in two ways. A first one involves direct interaction of Ser181 and Asp177 as illustrated in Figure 4.5b. This is observed in Monomer B and C when the H-bond distance between Ser181 and Asp177 is short (Figure 4.8a). Another possible network takes place with a water molecule connecting Ser181 to Asp177 (Figure 4.8c). There are thus at least three possible network schemes bridging His185 to Asp177 that differ only in the arrangement of the side chain of Ser181 and neighbouring water molecules. Interestingly, none of these H-bond networks is observed when His185 is not protonated. The protonation of His185 seems to favor the formation of stable H-bond networks going from His185 to Asp177, which could potentially facilitate the transport of a proton from the protonated His185 back to the extracellular side

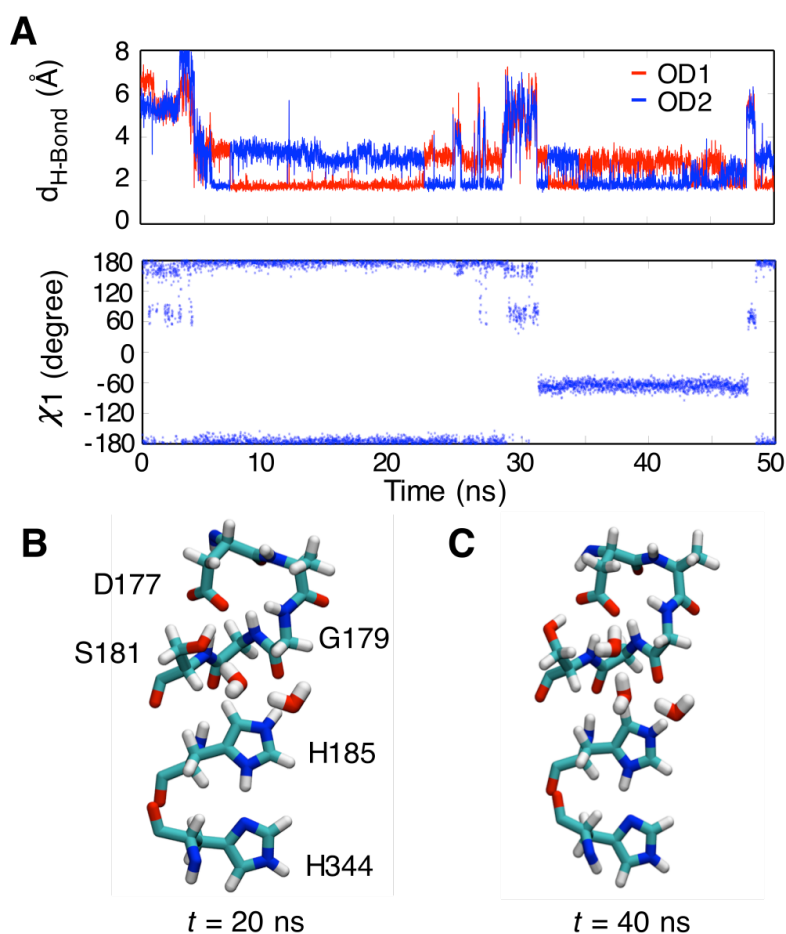


**Figure 4.5** Simulation of RhCG monomer with H185 protonated. a) The upper panel shows the H-bond distance between the Ser181 and Asp177 side chains, and the lower-panel shows the  $\chi_1$  dihedral angle of Ser181. b-c) The molecular representations show the H-bond network at  $t=20$  ns (b) and  $t=40$  ns (c).

#### 4.3.4 Proton transfer from His185 to Asp177

The transfer of a proton through the network of H-bonds connecting the protonated His185 to Asp177 was investigated using QM/MM simulations. Considering the structure presented in Figure 4.5b, we calculated a two-dimensional PMF from 100 ten-picosecond constrained QM/MM simulations in which the first reaction coordinate corresponds to the proton transfer from His185 to a water molecule and the second reaction coordinate is the proton transfer from Ser181 to Asp177. The PMF shows that the proton on His185 is first transferred to the water molecule and then the excess proton is stabilized by the aspartic acid Asp177 (Figure 4.6). It is interesting to note that the presence of the aspartic acid Asp177 is essential to attract the proton, which otherwise could not simply



transfer to the nearby water molecule. The formation of a  $\text{H}_3\text{O}^+$  molecule corresponds to the free energy barrier and no local free energy well is associated with the presence of such molecule. The free energy difference of the reaction is 9 kcal/mol with a barrier of 16 kcal/mol. This reaction constitutes the rate-limiting step of ammonium transport in RhCG. In our previous work we estimated the activation free energy of ammonium transport in AmtB between 12.5-16.6 kcal/mol. Since the transport rate of ammonium in RhCG and AmtB proteins are in the same order of magnitude, the activation free energy for RhCG is expected to be similar to that of AmtB (14). However, RhCG functions under mM ammonium concentrations, while AmtB functions under  $\mu\text{M}$  ammonium concentrations (16,37). The difference in ammonium concentrations in the environments in which these proteins are found (three order of magnitude) suggests that the activation free energy of RhCG protein could be about 4 kcal/mol higher. Overall, the free energy barrier calculated here is consistent with the free energy of activation derived from experimentally measured transport rates.

These calculations suggest that residues Asp177 and Ser181 play a crucial role in the transport of ammonium. The functional study performed by Yahiaoui et al. (2009) showed that mutation of aspartic acid Asp177 to asparagine impairs the ammonium transport in RhCG protein. We propose that residue Ser181 could have a similar impact. The simulations and free energy calculations we have carried out with His185 in its protonated state show that Ser181 is likely to be involved in the deprotonation of His185. In the configuration shown in Figure 4.5c, Ser181 is not directly involved in the proton transfer but it plays a structural role by maintaining Asp177 in position, allowing for the formation of a stable H-bond network that is chemically equivalent to the one seen in Figure 4.5b.

When His185 is protonated, it forms with His344 a dyad in which the +1 charge is delocalized. This implies that a proton could potentially be transferred from His344 N $\epsilon$  atom to a water molecule, or even to the ammonia molecule diffusing down the pore after deprotonation of ammonium. We used QM/MM simulations to calculate the corresponding PMFs (see Figure 4.3). While proton transfer to a water molecule seems unlikely, the transfer to  $\text{NH}_3$  cannot be excluded with a reaction free energy of 4 kcal/mol. In that event, could the proton on His185 N $\epsilon$  atom be transported through a water chain to His344 N $\epsilon$  atom like proposed for

Amt transporters (13). We carried out a 50 ns simulation of RhCG trimer with His185 protonated and His344 deprotonated to investigate the possible hydration of the pore. The simulation shows that no chain of water molecules forms in the pore of RhCG under such conditions (Figure 4.9). Lack of pore hydration when His344 is deprotonated reinforces the idea of a proton release from His185 toward the extracellular side. Even if His344 was to lose a proton to an ammonia molecule, it could accept a proton from a water molecule, allowing proton release from His185. The PMF of Figure 4.3 shows that His344 is a much better proton acceptor than water.

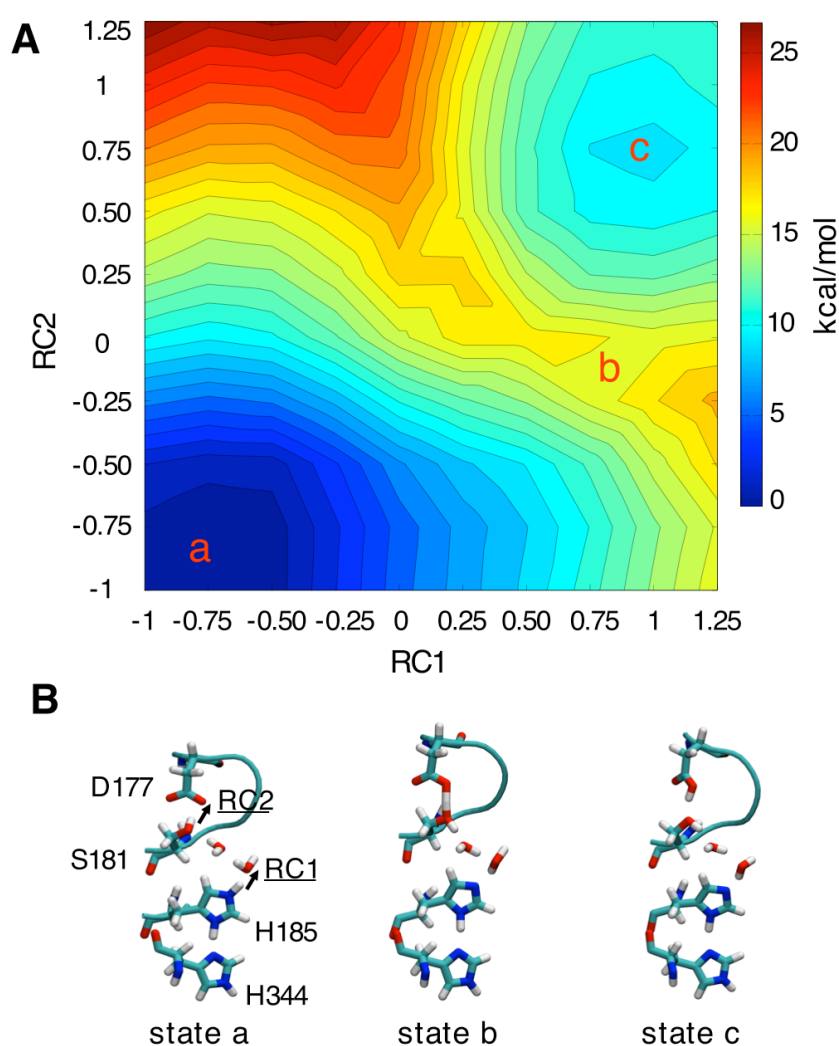


**Figure 4.6** Proton transfer from His185 to Asp177 through a network of H-bonds involving Ser181 and water molecules. a) The potential of mean force with the two reaction coordinates defined as  $RC1 = d_{\text{His185N}\epsilon\text{-H}} - d_{\text{Water-H}}$  and  $RC2 = d_{\text{Ser181O}\gamma\text{-H}} - d_{\text{Asp177OD1-H}}$  is shown. Each contour level corresponds to 1 kcal/mol. b) The molecular representations illustrate the initial “a”, intermediate “b”, and final “c” states, with the reaction coordinates shown in state a..

### 4.3.5 Release of the proton from D177

The free energy of deprotonation of an acid at a given pH can be calculated using the equation:

$$\Delta G^{Deprotonation}(pH) = -2.3kT(pH - pK_a) \quad (1)$$

where  $pK_a$  is the dissociation constant of the acid,  $k$  is the Boltzmann constant,  $T$  is the temperature. For an aspartic acid in solution, which has a  $pK_a$  of 4, the equation yields a deprotonation free energy of -4.1 kcal/mol (with  $kT = 0.6$  for  $T = 315K$ ). To calculate the free energy of releasing a proton from Asp177, we performed FEP calculations that involved the deprotonation of Asp177 and protonation of an aspartic acid dipeptide in bulk solution simultaneously. The starting conformation used for this calculation and obtained after equilibration of the monomeric molecular system with a protonated Asp177 is shown in Figure 4.10. The FEP calculation provides the free energy difference between the deprotonation of the aspartic acid in the protein and the one in solution  $\Delta\Delta G = \Delta G_{Protein}^{Deprotonation} - \Delta G_{Solution}^{Deprotonation} = 0.6 \pm 0.4$  kcal/mol. Taking into account the deprotonation free energy of an aspartic acid in solution, the free energy of releasing a proton from Asp177 to the extracellular solution is -3.5 kcal/mol. This result indicates that the release of a proton from Asp177 to bulk solution is favorable but not as much as the release from an aspartic acid in solution, which is better hydrated.

To close the transport cycle, we consider that the released proton react with  $NH_3$  in solution to form  $NH_4^+$ . At pH 7, considering a  $pK_a$  of 9.25 for  $NH_4^+$ , the reaction free energy is -3.1 kcal/mol. Given the periodic boundary conditions applied to the simulation systems, the overall mechanism should be energetically neutral since both sides of the membrane are strictly equivalent. In practice the free energy balance yields a difference of +0.9 kcal/mol, which reflects the accuracy of the calculation (Table 4.1).

#### 4. 4 Conclusion

Proteins from the Rh family were shown to facilitate neutral  $\text{NH}_3$  transport as opposed to Amt proteins which seem to generally transport  $\text{NH}_4^+$ . The mechanism by which Rh proteins transport  $\text{NH}_3$  remains poorly understood. While transport mechanisms propose on the basis of the AmtB structure involved recruitment of  $\text{NH}_4^+$  followed by its deprotonation, Rh protein are often assumed to simply facilitate  $\text{NH}_3$  diffusion (41). Given the low concentration of  $\text{NH}_3$  molecules, such mechanism seems unlikely to have a significant contribution to the overall transport of ammonium (39). Our simulations rather showed that RhCG can efficiently recruit  $\text{NH}_4^+$  at a site near His185 where electronic density was observed in X-ray crystallography experiments. Using QM/MM simulations we further showed that a proton can easily transfer from  $\text{NH}_4^+$  to His185, with an activation free energy barrier of 3 kcal/mol and a reaction free energy of 2 kcal/mol. The deprotonated substrate,  $\text{NH}_3$ , can spontaneously reach the hydrophobic pore, through which it diffuses facing free energy barriers of up to 3 kcal/mol.

The excess proton transferred from  $\text{NH}_4^+$  to His185 has to be removed for the protein to accept the next ammonium substrate. Like seen for AmtB (13), the release of this proton constitute a kinetics trap. In AmtB the only way out is through a water chain that transiently form in the hydrophobic pore, resulting in the net transport of  $\text{NH}_4^+$ . In RhCG, no such water chain is seen in the hydrophobic pore but a hydrogen bond network is formed between His185 and Asp177, allowing the proton to diffuse back toward the extracellular side. The transfer of a proton from His185 to Asp177 involves a free energy barrier of about 16 kcal/mol, in line with experimental transport rate. Asp177 is highly conserved among Amt/Rh proteins and mutation of this residue abolishes the transport activity in Rh proteins (14, 15).

Our calculations suggest that despite highly similar tridimensional structures, Amt and Rh proteins exert different functions, transport of  $\text{NH}_4^+$  for Amts and transport of  $\text{NH}_3$  for the Rh sub-family. In both transport mechanisms, the signature histidine dyad plays a central role as proton acceptor. The functional difference arise from the release of the proton, which happens through a water chain in the pore of Amts, or a hydrogen bond network involving a conserved aspartic acid on the extracellular side of Rh proteins.

## 4.5 Methods

### 4.5.1 Simulation systems

The RhCG simulation systems were prepared using the crystal structure from PDB entry 3HD6 (16). RhCG loops that were not resolved (residue 35-52 and 362-383) were modelled using the loop modelling function of the Rosetta program (17). Membrane systems of RhCG were built using the Charmm-GUI web server (18). The molecular systems were prepared by assembling a bilayer composed of 323 dimyristoylphosphatidylcholine (DMPC) lipid molecules around the RhCG trimer. The systems were solvated with 31,609 TIP3P water molecules, to which 95 K<sup>+</sup> and 80 Cl<sup>-</sup> ions were added to obtain a salt concentration of about 0.15 M. The tetragonal box of the trimeric systems contained 153,930 atoms, with dimensions of 120 × 120 × 104 Å<sup>3</sup>. The trimeric system was used to simulate three different conditions. In the first, a NH<sub>4</sub><sup>+</sup> molecule was added in each monomer at the position of the experimental electronic density peak found near His185, with a neutral histidine dyad His185/His344 in which His185 Nε is unprotonated. In the second system, NH<sub>4</sub><sup>+</sup> is replaced by NH<sub>3</sub> and a proton is added to His185. In the third system, there is no substrate in the pore, a proton is transferred from His185 Nδ to His344 Nδ and a proton is removed from His344 Nε. To maintain the electroneutrality of the system, three Cl<sup>-</sup> were also removed. In preparation for the classical and QM/MM free energy simulations, three monomeric systems were prepared, corresponding to the first two trimeric systems and a third one in which Asp177 is protonated (see below). A RhCG monomer was assembled with 204 DMPC lipids, 15,813 TIP3P water molecules, and 45 K<sup>+</sup> and 40 Cl<sup>-</sup> ions. The simulation box with dimensions of 88 × 88 × 100 Å<sup>3</sup> contained 78,538 atoms.

All simulation systems were equilibrated using CHARMM (version 36b1) and production runs were performed using NAMD (version 2.8b3) (19,20). Classical MD simulations were carried out with the CHARMM 27 force field (21). Electrostatic interactions were calculated using Particle-Mesh Ewald method with a grid spacing of 1 Å (22). Simulations were performed with a time step of 1 fs, with all interactions calculated at every time step. The temperature and pressure of the simulations were maintained at 315 K and 1 atm respectively.

### 4.5.2 Classical free energy calculations

We performed free energy perturbation (FEP) simulations to evaluate the relative binding free energy of  $\text{NH}_4^+$  to the pore. The calculation involved the alchemical transformation of  $\text{NH}_4^+$  into a water molecule at the putative binding site in the protein and in bulk water. The perturbation simulations were performed with a hybrid residue that contains both  $\text{NH}_4^+$  and a water molecule. Interaction of the hybrid residue with the surrounding environment was controlled using a parameter  $\lambda$  (ranging from 0 to 1). The reaction coordinate for each perturbation simulation was discretized into windows of width 0.1 for  $\lambda$  ranging from 0.1 to 0.9 and these windows were simulated for 400 ps (first 40 ps for equilibration). At the end points,  $\lambda$  was progressively increased with windows at 0, 0.001, 0.01, 0.05, and 0.95, 0.99, 0.999, 1 that were simulated for 200 ps (first 20 ps for equilibration). For each perturbation calculation, the combined forward and backward simulations amounted to a total simulation time of 9.6 ns. Free energy differences and statistical errors were calculated by combining the forward and backward configurational ensembles using the Bennett acceptance ratio (BAR) method as implemented in the ParseFEP toolkit (42) of the VMD visualization platform (43).

We also performed FEP calculations to study the deprotonation of Asp177. The perturbation consisted in the deprotonation of the aspartic acid in the protein combined with the simultaneous protonation of an aspartic acid dipeptide in bulk water. The monomeric system was equilibrated with Asp177 in its protonated state, the histidine dyad in its neutral state with His185 N $\epsilon$  unprotonated, and the addition of a dipeptide in solution away from the protein. This FEP calculation was carried out using 11 windows, varying lambda ( $\lambda$ ) between 0 and 1 by step of 0.1.  $\lambda = 0$  corresponds to the state where the aspartic acid in the protein is protonated and  $\lambda = 1$  corresponds to the state where the aspartic acid in the solvated dipeptide is protonated. Each window was simulated for 1 ns, with the first 200 ps considered as equilibration. This FEP calculation was performed using the PERT module of CHARMM (19) and the free energy difference was calculated from the combined sampling of forward and backward perturbations using the WHAM module of CHARMM (24).

Potentials of mean force (PMF) for  $\text{NH}_3$  diffusing through the hydrophobic pore was calculated using the Adaptive Biasing Force method of the NAMD

program (30-32). The reaction coordinate was defined as the distance along the Z-axis between the nitrogen of NH<sub>3</sub> and the center of mass of the C $\alpha$  atoms of Phe130 and Phe235. The reaction coordinate covering 20 Å was divided into four equidistant windows. Each window was simulated for 25 ns.

### 4.5.3 Quantum mechanics/molecular mechanics simulations

PMFs of proton transfer reactions were obtained from constrained quantum mechanics/molecular mechanics (QM/MM) simulations. The QM/MM simulations were performed using the CP2K program (23) with the settings described in Wang et al. (13). The reaction coordinate for a proton transfer is defined as the difference of the distances from the proton to the proton-acceptor and proton-donor atoms:

$$RC = d_{\text{Acceptor-H}} - d_{\text{Donor-H}}$$

1-D PMFs were calculated using 10 windows with RC = [-1, -0.75, -0.5, -0.25, 0, 0.25, 0.5, 0.75, 1.0, 1.25] and a simulation time of 10 ps per window. The 2-D PMF was obtained from simulations of 100 windows (combination of two reaction coordinations having 10 windows each) and each window was simulated for 10 ps. The proton was constrained according to the RC value and constraint forces acting on the proton were collected. PMFs were calculated by the integration of these forces. Force data for the first 2 ps of the simulations were considered as equilibration and were not used in the calculation of the PMFs.

In the PMF simulations for the proton transfer from NH<sub>4</sub><sup>+</sup> to His185, the atoms of the side-chains of His185, His344, Trp232, Phe235 and Asn236 residues, and the peptide bond between Gly179 and Gly180 amino acids are included in QM region. In the PMF simulations for the proton transfers from H344 to either ammonia or water, the QM region contains the side-chain atoms of H185 and H344, and water molecules around these atoms. The QM region of the 2-D PMF simulations contains the atoms of side-chains of His185, His344, Asn236, Asp177, Ala178, Gly179, Gly180, Ser181 and the peptide bond between Val291 and Ala292. Initial structures of the QM regions for the PMF simulations are given in Figure 4.7.

#### 4. 6 References

1. Ninnemann O, Jauniaux JC, Frommer WB. Identification of a high affinity NH<sub>4</sub><sup>+</sup> transporter from plants. *EMBO J* 1994, Aug 1;13(15):3464-71.
2. Marini AM, Soussi-Boudekou S, Vissers S, Andre B. A family of ammonium transporters in *saccharomyces cerevisiae*. *Mol Cell Biol* 1997, Aug;17(8):4282-93.
3. Ludwig U, von Wirén N, Frommer WB. Uniport of NH<sub>4</sub><sup>+</sup> by the root hair plasma membrane ammonium transporter *leamt1*;1. *J Biol Chem* 2002, Apr 19;277(16):13548-55.
4. Siewe RM, Weil B, Burkovski A, Eikmanns BJ, Eikmanns M, Krämer R. Functional and genetic characterization of the (methyl)ammonium uptake carrier of *corynebacterium glutamicum*. *J Biol Chem* 1996, Mar 8;271(10):5398-403.
5. Ripoche P, Bertrand O, Gane P, Birkenmeier C, Colin Y, Cartron JP. Human rhesus-associated glycoprotein mediates facilitated transport of NH(3) into red blood cells. *Proc Natl Acad Sci U S A* 2004, Dec 7;101(49):17222-7.
6. Mouro-Chanteloup I, Cochet S, Chami M, Genetet S, Zidi-Yahiaoui N, Engel A, et al. Functional reconstitution into liposomes of purified human rhcg ammonia channel. *PLoS ONE* 2010;5(1):e8921.
7. Khademi S, O'Connell J, Remis J, Robles-Colmenares Y, Miercke LJ, Stroud RM. Mechanism of ammonia transport by *amt*/MEP/rh: Structure of *amtB* at 1.35 Å. *Science* 2004, Sep 10;305(5690):1587-94.
8. Zheng L, Kostrewa D, Bernèche S, Winkler FK, Li XD. The mechanism of ammonia transport based on the crystal structure of *amtB* of *escherichia coli*. *Proc Natl Acad Sci U S A* 2004, Dec 7;101(49):17090-5.
9. Lin Y, Cao Z, Mo Y. Molecular dynamics simulations on the *escherichia coli* ammonia channel protein *amtB*: Mechanism of ammonia/ammonium transport. *J Am Chem Soc* 2006, Aug 23;128(33):10876-84.
10. Luzhkov VB, Almlöf M, Nervall M, Aqvist J. Computational study of the binding affinity and selectivity of the bacterial ammonium transporter *amtB*. *Biochemistry* 2006, Sep 12;45(36):10807-14.
11. Bostick DL, Brooks CL. Deprotonation by dehydration: The origin of ammonium sensing in the *amtB* channel. *PLoS Comput Biol* 2007, Feb 9;3(2):e22.



12. Nygaard TP, Rovira C, Peters GH, Jensen MØ. Ammonium recruitment and ammonia transport by E. Coli ammonia channel amtB. *Biophys J* 2006, Dec 15;91(12):4401-12.
13. Wang S, Orabi EA, Baday S, Bernèche S, Lamoureux G. Ammonium transporters achieve charge transfer by fragmenting their substrate. *J Am Chem Soc* 2012, Jun 27;134(25):10419-27.
14. Zidi-Yahiaoui N, Callebaut I, Genetet S, Le Van Kim C, Cartron JP, Colin Y, et al. Functional analysis of human rhcg: Comparison with E. Coli ammonium transporter reveals similarities in the pore and differences in the vestibule. *American Journal of Physiology-Cell Physiology* 2009;297(3):C537-47.
15. Marini AM, Boeckstaens M, Benjelloun F, Chérif-Zahar B, André B. Structural involvement in substrate recognition of an essential aspartate residue conserved in mep/amt and rh-type ammonium transporters. *Curr Genet* 2006, Jun;49(6):364-74.
16. Gruswitz F, Chaudhary S, Ho JD, Schlessinger A, Pezeshki B, Ho CM, et al. Function of human rh based on structure of rhcg at 2.1 Å. *Proc Natl Acad Sci U S A* 2010, May 10;107(21):9638-43.
17. Wang C, Bradley P, Baker D. Protein-protein docking with backbone flexibility. *J Mol Biol* 2007, Oct 19;373(2):503-19.
18. Jo S, Kim T, Iyer VG, Im W. CHARMM-GUI: A web-based graphical user interface for CHARMM. *J Comput Chem* 2008, Aug;29(11):1859-65.
19. Brooks BR, Brooks CL, Mackerell AD, Nilsson L, Petrella RJ, Roux B, et al. CHARMM: The biomolecular simulation program. *J Comput Chem* 2009, Jul 30;30(10):1545-614.
20. Phillips JC, Braun R, Wang W, Gumbart J, Tajkhorshid E, Villa E, et al. Scalable molecular dynamics with NAMD. *J Comput Chem* 2005, Dec;26(16):1781-802.
21. MacKerell Jr AD, Bashford D, Bellott M, Dunbrack Jr RL, Evanseck JD, Field MJ, et al. All-atom empirical potential for molecular modeling and dynamics studies of proteins. *The Journal of Physical Chemistry B* 1998;102(18):3586-616.
22. Essmann U, Perera L, Berkowitz ML, Darden T, Lee H, Pedersen LG. A smooth particle mesh ewald method. *J Chem Phys* 1995;103:8577.

23. Laino T, Mohamed F, Laio A, Parrinello M. An efficient real space multigrid QM/MM electrostatic coupling. *J Chem Theory Comput* 2005;1(6):1176-84.
24. Souaille M, Roux B. Extension to the weighted histogram analysis method: Combining umbrella sampling with free energy calculations. *Computer Physics Communications* 2001;135(1):40-57.
25. Kollman P. Free energy calculations: Applications to chemical and biochemical phenomena. *Chem Rev* 1993;93(7):2395-417.
26. Lamoureux G, Harder E, Vorobyov IV, Roux B, MacKerell AD. A polarizable model of water for molecular dynamics simulations of biomolecules. *Chem Phys Lett* 2006;418(1):245-9.
27. Lamoureux G, MacKerell Jr AD, Roux B. A simple polarizable model of water based on classical drude oscillators. *J Chem Phys* 2003;119:5185.
28. Lopes PE, Roux B, Mackerell AD. Molecular modeling and dynamics studies with explicit inclusion of electronic polarizability. Theory and applications. *Theor Chem Acc* 2009, Sep;124(1-2):11-28.
29. Orabi EA, Lamoureux G. Cation-  $\pi$  and  $\pi$ - $\pi$  interactions in aqueous solution studied using polarizable potential models. *J Chem Theory Comput* 2011;8(1):182-93.
30. Darve E, Pohorille A. Calculating free energies using average force. *J Chem Phys* 2001;115:9169.
31. Darve E, Rodríguez-Gómez D, Pohorille A. Adaptive biasing force method for scalar and vector free energy calculations. *J Chem Phys* 2008, Apr 14;128(14):144120.
32. Hénin J, Chipot C. Overcoming free energy barriers using unconstrained molecular dynamics simulations. *J Chem Phys* 2004, Aug 15;121(7):2904-14.
33. Hénin J, Fiorin G, Chipot C, Klein ML. Exploring multidimensional free energy landscapes using time-dependent biases on collective variables. *J Chem Theory Comput* 2009;6(1):35-47.
34. Alhambra C, Corchado JC, Sánchez ML, Gao J, Truhlar DG. Quantum dynamics of hydride transfer in enzyme catalysis. *J Am Chem Soc* 2000;122(34):8197-203.

35. Alhambra C, Luz Sánchez M, Corchado J, Gao J, Truhlar DG. Quantum mechanical tunneling in methylamine dehydrogenase. *Chem Phys Lett* 2001;347(4):512-8.
36. Cui Q, Karplus M. Is a “proton wire” concerted or stepwise? A model study of proton transfer in carbonic anhydrase. *The Journal of Physical Chemistry B* 2003;107(4):1071-8.
37. Javelle A, Severi E, Thornton J, Merrick M. Ammonium sensing in *Escherichia coli*. Role of the ammonium transporter *amtB* and *amtB-glnK* complex formation. *J Biol Chem* 2004, Mar 5;279(10):8530-8.
38. Andrade SL, Dickmanns A, Ficner R, Einsle O. Crystal structure of the archaeal ammonium transporter *amt-1* from *Archaeoglobus fulgidus*. *Proc Natl Acad Sci U S A* 2005, Oct 18;102(42):14994-9.
39. Lupo D, Li XD, Durand A, Tomizaki T, Cherif-Zahar B, Matassi G, et al. The 1.3-Å resolution structure of *Nitrosomonas europaea* rh50 and mechanistic implications for NH<sub>3</sub> transport by rhesus family proteins. *Proc Natl Acad Sci U S A* 2007, Dec 4;104(49):19303-8.
40. Baday S, Wang S, Lamoureux G, Bernèche S. Different hydration patterns in the pores of *amtB* and *rhcg* could determine their transport mechanisms. *Biochemistry* 2013, 52(40):7091-8.
41. Hub JS, Winkler FK, Merrick M, de Groot BL. Potentials of mean force and permeabilities for carbon dioxide, ammonia, and water flux across a rhesus protein channel and lipid membranes. *J Am Chem Soc* 2010, 132(38):13251-63.
42. Liu P, Dehez F, Cai W, Chipot CJ. A toolkit for the analysis of free-energy perturbation calculations. *J Chem Theory Comput* 2012, Jul 18;8:2606–2616.
43. Humphrey W, Dalke A, Schulten K. VMD: Visual molecular dynamics. *J Mol Graph* 1996, Feb;14(1):33-8, 27-8.

## 4.7 Appendix

### 4.7.1 Tables

**Table 4.1** Free energy balance of the complete transport mechanism considering symmetric conditions at pH 7

Steps	$\Delta G$ (kcal/mol)
Recruitment of $\text{NH}_4^+$	-5.5
Deprotonation of $\text{NH}_4^+$ , protonation of His185	+2
Diffusion of $\text{NH}_3$ out of the pore	+2
Proton transfer from His185 to Asp177	+9
deprotonation of Asp177	-3.5
Production of $\text{NH}_4^+$ from $\text{NH}_3$ and $\text{H}_3\text{O}^+$	-3.1
Overall	+0.9

## 4.7.2 Figures

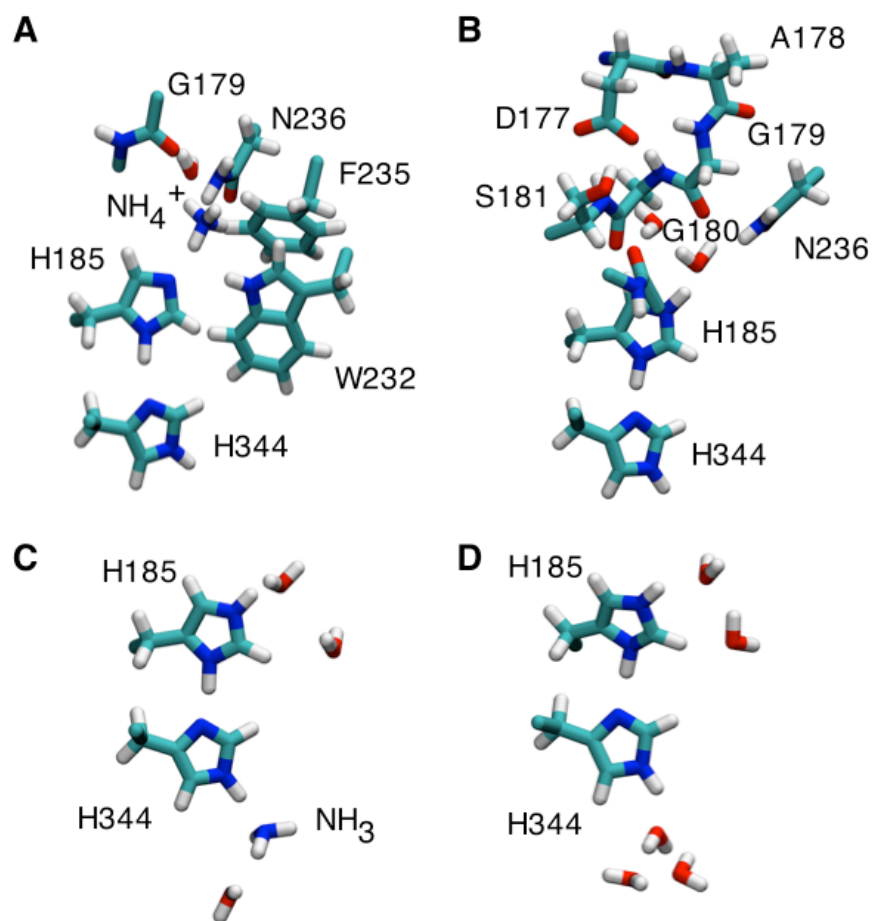


**Figure 4.7** Initial structures of the QM regions in the different QM/MM simulations. Molecular representations are shown for the systems used for the following calculations: a) proton transfer from ammonium to His185, b) proton transfers from H185 to a water molecule and from Ser181 to Asp177, c) proton transfer from His344 to an ammonia molecule, d) proton transfer from His344 to a water molecule.

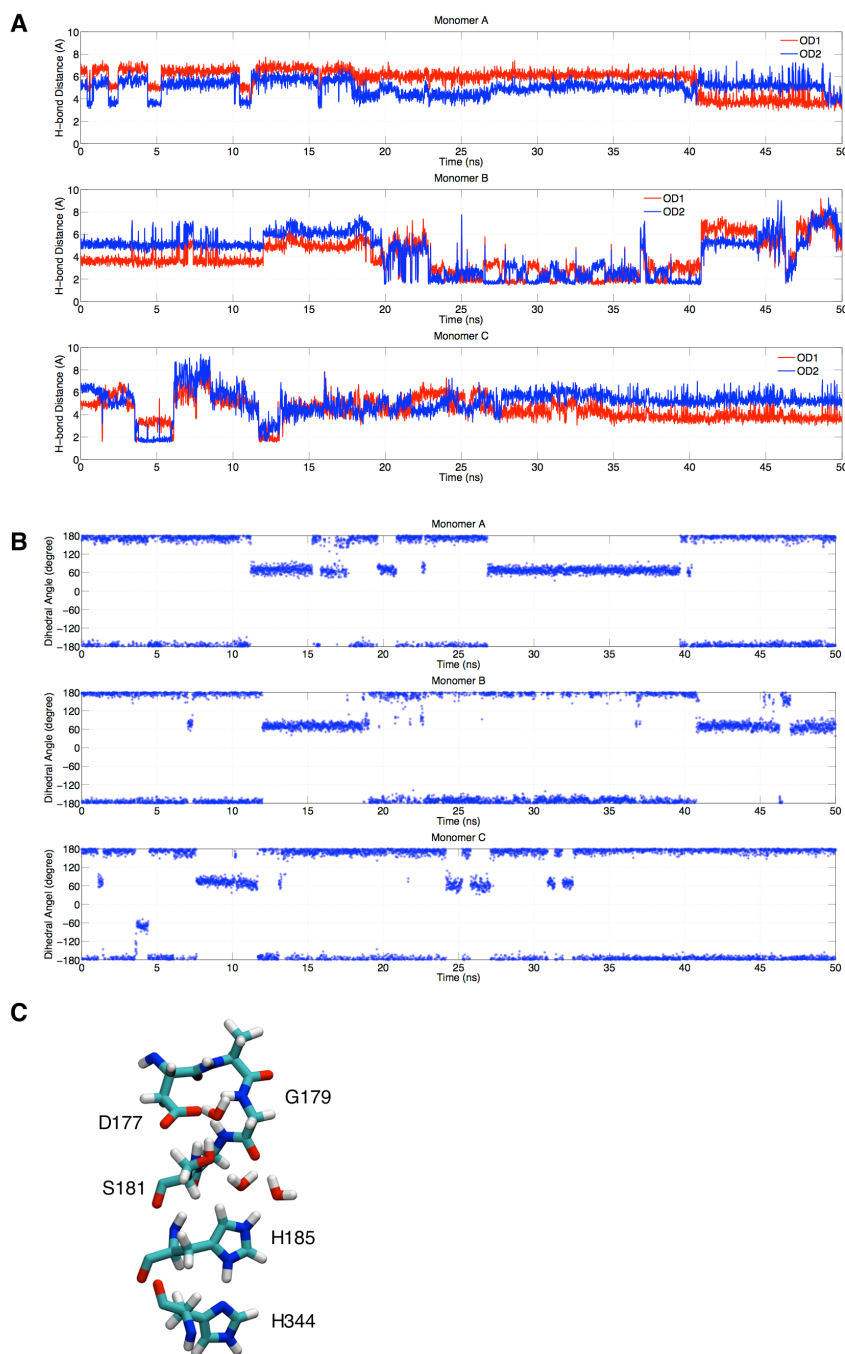


**Figure 4.8** Simulation of RhCG trimer with His185 protonated. a) The H-bond distance between Ser181 and Asp177 in each monomer. b) The  $\chi_1$  dihedral angle of residue Ser181 in each monomer. c) Representative snapshot of the H-bond network with a water molecule intercalated between residues Ser181 and Asp177, taken from monomer B at  $t = 10$  ns.

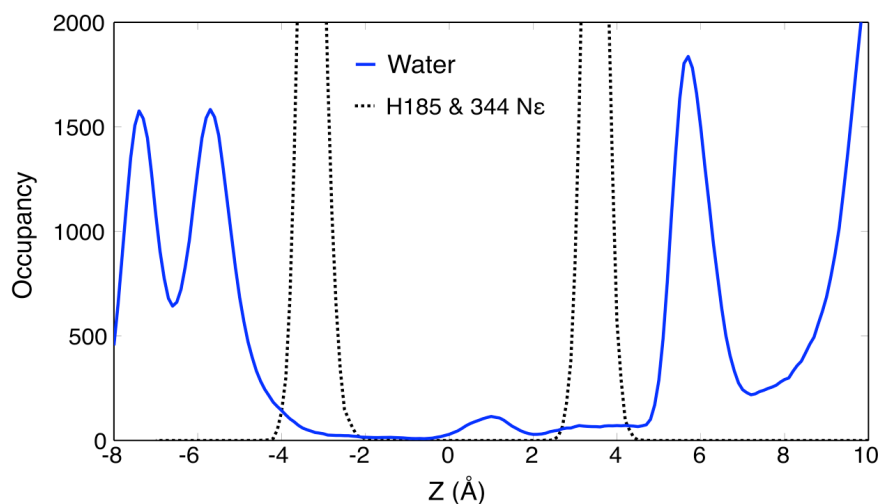


**Figure 4.9** Water density in the pore of RhCG when His185 is protonated. Practically no water molecules are observed at the level of the two histidine residues.

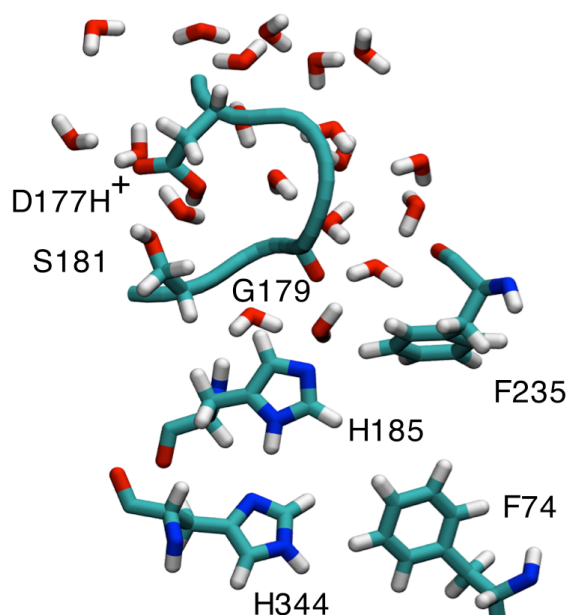


**Figure 4.10** Initial structure of the pore used for the Asp177 deprotonation free energy perturbation (FEP) calculation. Key residues of the pore, including the protonated Asp177, are shown with nearby water molecules.

**Chapter 5**

**THE EFFECT OF HYDROPHOBICITY OF THE SECY TRANSLOCON  
PORE IN MEMBRANE PROTEIN INSERTION**

A part of the section 5.3 was published in PNAS(2013, 110 (47): 18856-6) with the following authors: Erhan Demirci, Tina Junne, Sefer Baday, Simon Berneche and Martin Spiess.



## 5.1 Introduction

### 5.1.1 An Overview of Membrane protein insertion

Integral membrane proteins constitute 20-30% percent of proteins and play important roles in various biological functions. Proteins from Sec family, Sec61 in eukaryotes and SecY in prokaryotes, facilitate integration of most membrane proteins into the endoplasmic reticulum (ER) membrane and the plasma membrane respectively. Insertion of proteins into the membrane can happen both cotranslationally and post-translationally, but mostly cotranslationally. Sec translocons also facilitate translocation of secretory proteins across the lipid bilayer (1).

Cotranslational translocation and insertion utilizes the same molecular machinery to acquire a nascent protein chain from the ribosome. Figure 5.2 summarizes important elements of this machinery. As N-terminal signal sequence or a transmembrane sequence emerges from the exit tunnel of the ribosome, it is recognized by signal recognition particle (SRP). The ribosome-SRP complex binds to the SRP receptor (SR) on the membrane. Then this interaction guides the ribosome to interact with the translocon in such a way that the ribosomal exit tunnel aligns with the interior of the translocon. Finally elongating sequence moves through the translocon as translation proceeds. After insertion of the nascent protein chain inside the pore of the translocon, destiny of the protein (translocation or insertion) is determined by the hydrophobicity of the sequence of the protein (2-8).

Signal sequences are important not only for targeting but also the topology of membrane proteins. The orientation of a signal sequence determines the topology of membrane proteins. Depending on the orientation of the signal sequence either N-terminal or C-terminal stays in the cytosol (Figure 5.1). Among a number of factors affecting the orientation of a signal sequence the most prominent is the distribution of positively charged residues on the signal sequence (2). It has been discovered that the cytoplasmic side of membrane proteins has more positively charged amino acids than the other sides has. This situation is known as “positive-inside rule” (9-11). In bacteria, “positive-inside rule” could result from two important factors: the membrane potential and having more negatively charged lipid head groups in cytosolic site (12,13). However, in eukaryotes these two

factors cannot cause “positive-inside rule” due to the fact that there is no lipid asymmetry and membrane potential across the ER membrane. Goder et al. showed that sec61 contributes to the “positive-inside rule” by electrostatic interactions between flanking charges of the signal sequence and specific charged residues in Sec61 (14).

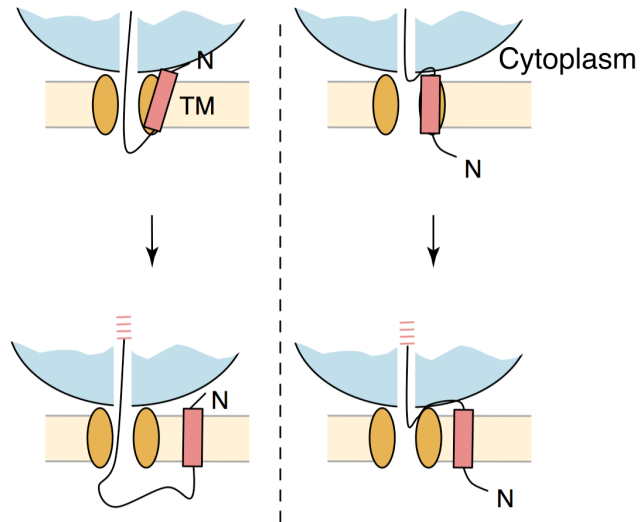


**Figure 5.1** Schematic representation of orientation of a TM helix with N-terminal staying in cytosol (left-side) or in ER lumen (right-side). Adapted from (15).

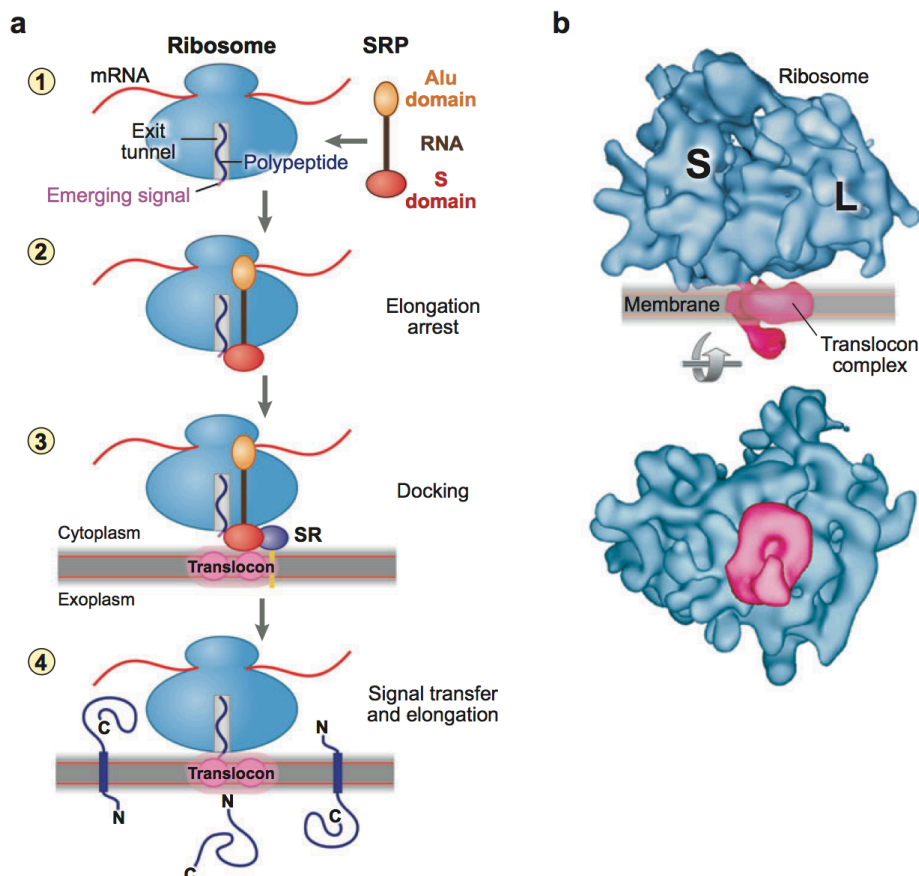


**Figure 5.2** Cotranslational membrane protein insertion. A) Steps of nascent protein insertion, step1: translation of mRNA; step2: binding of signal recognition particle (SRP) to ribosome; step3: binding of Ribosome-SRP complex to the membrane-bound SRP receptor (SR); step4: insertion or translocation of a newly synthesized protein. B) Cryo-EM image of the canine ribosome-translocon (Sec61) complex. Taken from (6).

### 5.1.2 Structure of the translocon

To date several structures of translocons at various stages of insertion process have been determined. These structures provided important information on the insertion of proteins in membrane. Van den berg et al. obtained the crystal structure of SecY from *Methanococcus jannaschii* at a resolution of 3.2 Å (Van den Berg et al 2004). This structure shows how the three subunits ( $\alpha$ ,  $\beta$ , and  $\gamma$ ) of SecY interact. The  $\alpha$  subunit forms the main body of the channel (Figure 5.3). It is divided into two domains formed by transmembrane helices (TM) 1-5 and 6-10. These two domains are hinged by a loop between TM5 and TM6. The  $\alpha$  subunit is

clamped by the  $\gamma$  subunit. The  $\gamma$  subunit has two helices; one lies along the membrane-water interface and the other one extends diagonally across the membrane. The  $\beta$  subunit consists of a disordered and a loop segment, and stays perpendicular to the membrane. The  $\alpha$  and  $\gamma$  subunits have high sequence conservation and are vital for cell viability (16).

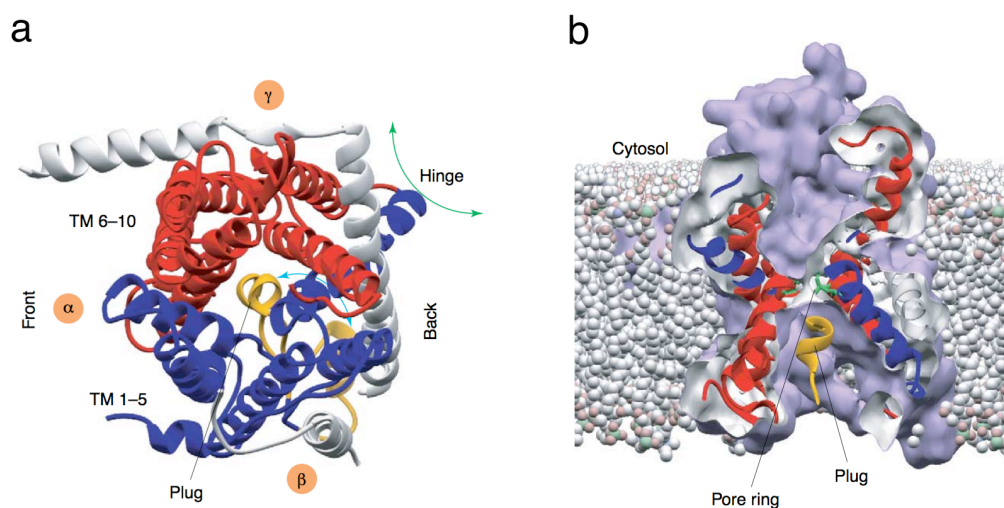


**Figure 5.3** The crystal structure of SecY from *M. jannaschii*. a) top view, b) front view. Adapted from (15).

According to the X-ray structure, the  $\alpha$  subunit forms a pore with an hourglass shape. At the narrowest point of this pore six hydrophobic residues form a ring-like structure, which is known as the “pore-ring”. The constriction of the channel is sealed from the periplasmic side by a short helix called the “plug” (Figure 5.3). It has been shown that the plug stabilizes the closed state of the translocon (17). However, deletion of the plug domain in SecY does not affect viability of the cells, but hamper protein translocation efficiency (17-19). In addition, it has been shown that the plug domain is required to seal the pore for preventing the leakage of small molecules and ions (20,21). This function of the plug is highly crucial for the viability of bacteria, since they have to maintain the membrane potential. Interestingly, when the plug domain is removed, neighboring loops form a plug-like structure to seal the pore (17).

The X-ray structure reveals a putative lateral gate that opens to provide a room for a polypeptide chain for insertion into the membrane or translocation across the membrane. This lateral gate is formed by the transmembrane helices TM2 and

TM7. The mechanism for lateral gate opening is not known exactly. Binding of SecY partner (ribosome or SecA) and intercalation of signal sequence are suspected to cause the opening of the lateral gate (22,23). Structures of Sec proteins bound to several binding partners showed various degree of opening (ranging from 10 Å to 24 Å) of the lateral gate at several conditions. Moreover, cross-link experiments showed that cross-links shorter than 5 Å abolished protein translocation (24).

Here, we briefly present other structural data obtained for Sec proteins. Zimmer et al. obtained the crystal structure of SecY (from *Thermotoga maritima*) bound to cytoplasmic SecA ATPase, which is involved in post-translational translocation of secretory proteins (25). Tsukazaki et al. solved the crystal structure of *Thermus thermophilus* SecY bound to the Fab fragment of a monoclonal antibody, which binds to SecY at the same site SecA does (26). Gumbart et al. modeled atomistic structure of the ribosome-SecY complex by applying molecular dynamics flexible fitting (MDFF) method using cryo-electron microscopy (cryo-EM) data (27). Becker et al. reported cryo-EM structures of yeast and mammalian Sec61 with the ribosome (28). Frauenfeld et al. achieved to acquire cryo-EM structures of translating ribosome bound to SecY in the lipid bilayer using Nanodiscs (29). In addition, two structures of SecY with surrogate polypeptides for nascent protein; X-ray structure of SecY from *Pyrococcus furiosus* and cryo-EM structure of *E. coli* SecY (30,31).

### **5.1.3 Hydrophobicity scales for membrane partitioning of amino acids**

To understand how proteins insert into the membrane, thermodynamics of membrane integration of different amino acids has been studied by several groups. These studies led to determine the membrane partitioning tendencies, which are known as hydrophobicity scales, of amino acids or amino acid side-chain like molecules (Figure 5.4) (32). First, Radzicka and Wolfenden obtained partition coefficient of amino acid side-chain analogs between water and cyclohexane environment (33). They added side-chain analog molecules in the biphasic medium and measured the concentrations in each phase. Free energy of transfer for side-chain analogs was obtained from the ratio of concentrations. Later, MacCallum et al. performed molecular dynamics simulations to obtain the free energy of insertion of the side-chain analogs, which Radzicka et al. used in their

experiments, from water solution to a lipid bilayer composed of dioleoylphosphatidylcholine (DOPC) lipids (34). They obtained distribution of these side-chain analogs as a function of the distance from the center of the lipid bilayer. Free energies of the molecules when they are at the center of the bilayer match well with the experimentally estimated free energies. White and coworkers investigated the partitioning of pentapeptides, which contain a test amino acid in the middle, from water to bilayer and octanol environment (35,36). They developed a hydrophobicity scale based on these experiments. However, these scales show partitioning to lipid-water interface rather than lipid environment. Hessa et al. performed insertion experiments of peptides using a method that involves sec61 translocon (37). They added a test sequence of 19 amino acid to the leader peptidase protein, which is known to insert into the membrane. They engineered this construct in such a way that it has two glycosylation sites, one before and one after this test sequence. If the test sequence inserts into the membrane, one site is glycosylated; if the test sequence is rather translocated, then two sites are glycosylated. Using this method they tested insertion of peptides of various hydrophobicities and created a hydrophobicity scale based on these experiments. Recently, Moon and Fleming (38) obtained water to bilayer free energy scale for amino acids by performing insertion experiments of the outer membrane phospholipase A (OmpLA) protein. To obtain the hydrophobicity scale, they performed the experiments with mutants of an alanine residue located at position 210. The position 210 in this protein is exposed to the membrane, which provides a reliable environment for water to bilayer insertion study. Overall, the hydrophobicity scales mentioned here are in agreement with each other not in the exact values but in the trends (39). It should be noticed that all of these hydrophobicity scales were derived for one amino acid at a time. Moreover, the cooperativity and additivity of these scales remains unclear.

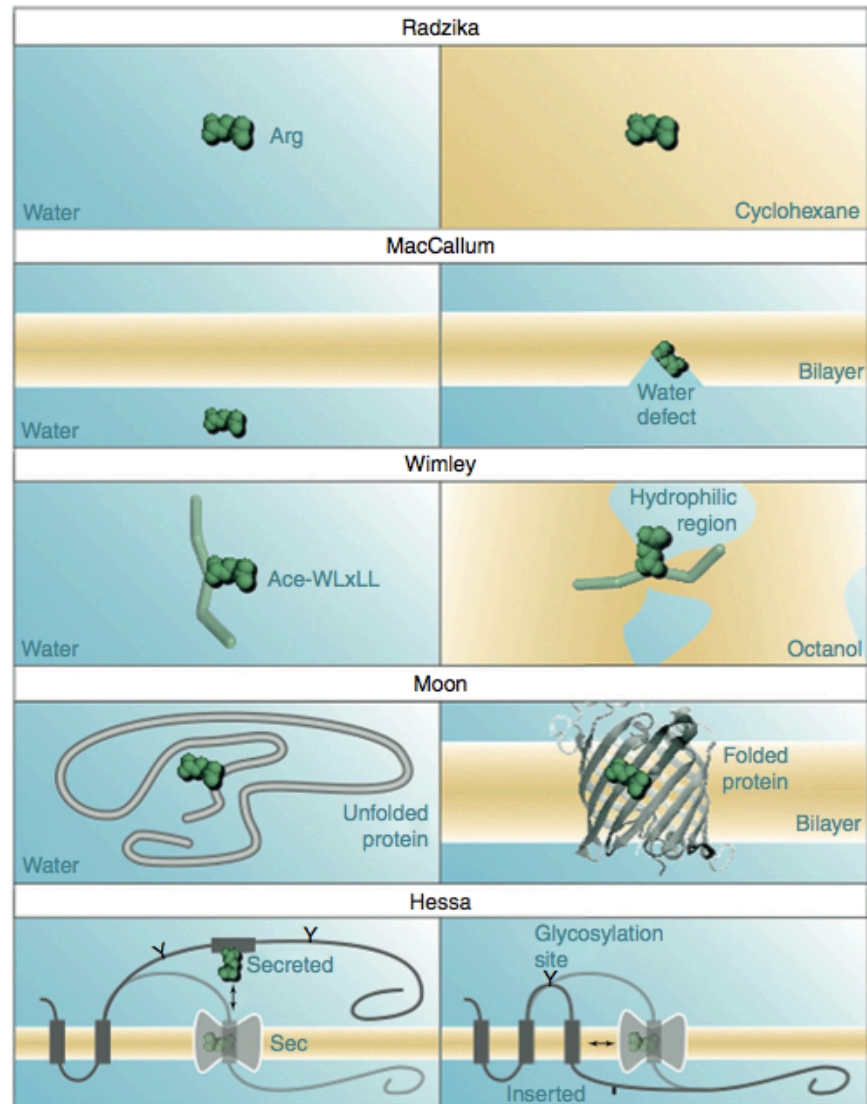


**Figure 5.4** Summary of different systems and environments for different hydrophobicity scales. Taken from (39)

#### 5.1.4 Are translocons just catalyzers in membrane protein insertion or not?

It has been disputed whether the translocon acts as a catalyzer by simply providing a suitable environment to proteins for membrane insertion or dynamics of translocon affect membrane integration of proteins. The catalyzer view suggests that an elongating nascent polypeptide is thermodynamically in equilibrium with the membrane and the destiny of the polypeptide is determined mainly by the protein-lipid interactions. This two-state partitioning hypothesis has been strengthened by two important observations. First, predictions for membrane integration based on the hydrophobicity scale developed by Hessa et al. yielded

high accuracy (40). Second, translocon based hydrophobicity scale from Hessa et al. correlates well with the direct water to octanol scale from Wimley et al (37).

However, several experimental and computational studies suggested that non-equilibrium kinetics effects also play an important role in the membrane protein insertion process. Goder et al. showed that the rate of translocation is affected by the rate of translation (41). In another study, the authors also showed that the translation rate affects the insertion topology (41). Experiments performed by Hessa et al. indicated that the length of the carboxy-terminal tail of marginally hydrophobic sequences influence the stop-transfer efficiency (42). Experimental studies of Gilmore and coworkers suggested that the fluctuation rate of the lateral gate opening affects the fidelity of membrane protein integration (43,44). Atomistic and coarse-grained (CG) simulations performed by Zhang et al. claimed that the lateral gate opening is regulated by the hydrophobicity of the elongating peptide (23). Using CG simulations Warshel and Rychkova claimed that competition between the free energy barriers in translocation and membrane insertion kinetics determines the destiny of a peptide (45).

On the other hand, recently, it has been proposed that both insertion kinetics and thermodynamics are important and the balance between these two governs the membrane integration (46,47).

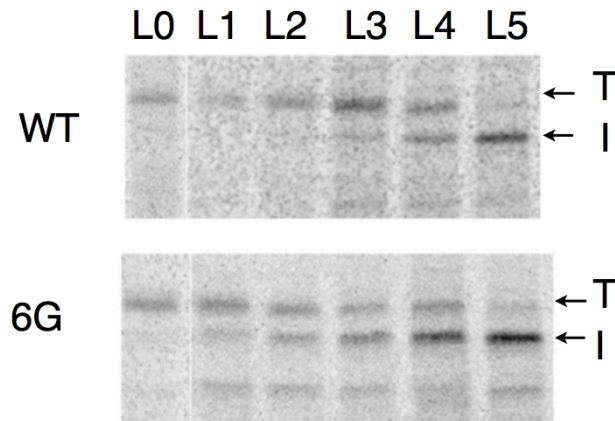
### **5.1.5 Outline for the sections 5.2 and 5.3**

In the rest of chapter 5, we study how the structure of the SecY pore impacts on the membrane integration process. To achieve this we investigated the stability of membrane-inserting and non-inserting peptides in SecY WT and pore-ring mutants studied by Spiess and coworkers (48). In addition, we focused on the asymmetry in membrane integration observed by the Spiess lab (64). We propose that the hydrophobicity profile of the translocon pore contributes to this asymmetry in insertion.



## **5.2 Investigating the stability of membrane-inserting and non-inserting peptides inside the pore of SecY and its pore-ring mutants**

We investigated how the stability of a membrane-inserting peptide inside the pore of the translocon affects its membrane insertion rate. Junne et al. performed experiments on the insertion of peptides of variable hydrophobicity in wild-type Sec61p and its pore-ring mutants (48). To understand the effect of pore-ring mutations in membrane insertion we studied the stability of L1 peptide (having 1 Leu and 18 Ala) in SecY WT and SecY 6G mutant (glycine mutants of the pore ring residues). While L1 peptide doesn't insert into the membrane via Sec61 WT, it inserts into membrane via Sec61 6G mutant (Figure 5.5). We performed free energy perturbation (FEP) calculations to obtain the absolute solvation free energy of L1 peptide in four different media: bulk water, DMPC membrane, SecY WT and SecY 6G mutant. We performed each FEP simulation over 170 ns, as growing a whole helix converges slowly. Gumbart et al. performed similar FEP simulations on the SecY system, achieving convergence with 120 ns per simulation (49). In the FEP simulations we performed, peptides were restrained to maintain a helical structure. Several studies showed that helical structures could be stabilized in the ribosome exit tunnel and inside the pore of translocon (50-53). Results of our FEP simulations are given in Table 5.1. It seems that L1 peptide is the most stable in membrane and the least stable in water. SecY WT and SecY 6G offer to the peptide an environment of the hydrophobicity in between membrane and water. However, L1 peptides feel more "water-like" environment in SecY 6G and "membrane-like" environment in SecY WT. The difference of water density around L1 in SecY WT and SecY 6G indicates that the pore of 6G mutants is hydrated better at the level of pore-ring residues than the pore of WT at the same level (Figure 5.6). Our results suggest that, for mildly hydrophobic sequences, as the stability inside the pore of the translocon increases the retention time in the pore increases. This gives rise to an increase of translocation and decrease of membrane insertion.



T.Junne et al. Mol.Biol.Cell 2010

**Figure 5.5** Membrane insertion of H-segments of various hydrophobicities in Sec61 WT and Sec61 6G mutant (48)

**Table 5.1** Absolute free energy of solvation of L1 peptide in various media

Medium	Forward (kcal/mol)	Backward (kcal/mol)	Bar Estimate (kcal/mol)
SecY WT	-103.93	93.46	-98.38±0.24
SecY 6G	-90.86	82.94	-86.92±0.22
Water	-84.85	83.43	-84.19±0.15
Membrane	-112.64	103.34	-108.08±0.23

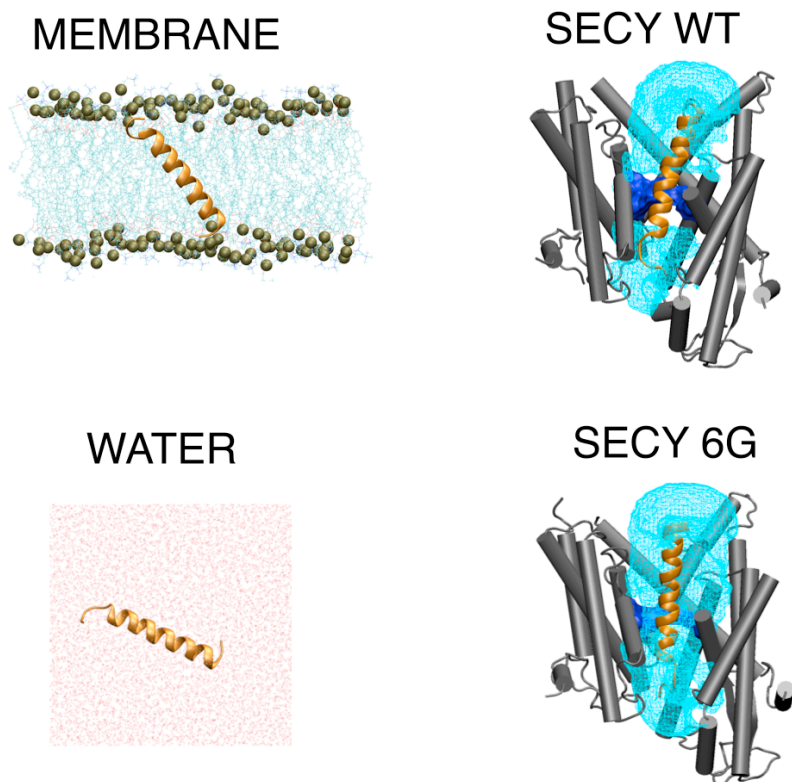


**Figure 5.6** Snapshots of L1 in membrane, water, SecY WT and SecY 6G. Regions shown as light blue in SecY WT and SecY 6G represent the water density (iso-surface of 0.3) 5 Å around the L1 peptide.

We also studied the stabilities of membrane-inserting L7 peptide (7 Leu and 11 Ala) in comparison with the non-inserting L1 (1 Leu and 18 Ala) peptide in water, membrane, SecY WT and SecY 6G. We calculated the free energy difference between the L7 and L1 peptides in the aforementioned media using FEP simulations. Each perturbation simulation was carried out for 50 ns. Results of these FEP simulations are given in Table 5.2. They illustrate that there is a big free energy difference (9 kcal/mol) between L7 and L1 peptides in water while they have almost the same free energy in the membrane. Growing a leucine side chain in water solution causes high free energy cost due to the loss of entropy of water molecules. However, lipid molecules in the membrane are not disturbed as much by the creation of a leucine side chains. This is because the membrane does not lose as much entropy upon the replacement of alanine to leucine. We could

conclude that the interaction of a peptide with lipid molecules is not the sole determinant of membrane insertion, because membrane-inserting and non-inserting peptides have similar stability in the membrane.

Moreover, we performed FEP simulations for perturbing one leucine to one alanine (from L7 to L6) and perturbing six leucine to six alanine (from L7 to L1) in water solution. We found that the free energy of perturbing one leucine to alanine in water is -0.93 kcal/mol, while the free energy of perturbing six leucine to six alanine in water is -9.1 kcal/mol. This shows that effective free energy gain per Leu-Ala perturbation for the L7-L1 perturbation (-1.5 kcal/mol) is higher than that for the L7-L6 perturbation (-0.93 kcal/mol). This result can be explained from the fact that a leucine together with other leucines disturbs more water molecule than one leucine itself alone does. We also carried out the same perturbations (L7-L1 and L7-L6) in the lipid environment. In contrast to water molecules, lipid molecules are not significantly affected by the number of Leu-Ala perturbation. Our results suggest that solvation free energies of amino acids are not additive and highly depend on molecular interactions with the surrounding environment.

**Table 5.2** Free energy of the perturbation of L7 to L1 and L6 in various media

Perturbation	Forward (kcal/mol)	Backward (kcal/mol)	Bar Estimate (kcal/mol)
L7 to L6 in water	-0.94	0.94	-0.93±0.04
L7 to L6 in Membrane	0.64	-0.48	0.56±0.05
L7 to L1 in water	-9.6	8.6	-9.1±0.1
L7 to L1 in membrane	0.34	0.6	-0.08±0.14
L7 to L1 in SecY 6G	-3.2	3.71	-3.35±0.11
L7 to L1 in SecY WT	0.53	1.28	-0.39±0.11

### 5.3 Asymmetry in membrane insertion caused by Sec translocon

Our collaborators from the Spiess group performed experiments on the insertion of peptides composed of alanine and leucine residues to investigate the effect of position of leucines on the membrane integration rate. The peptides used for these experiments were characterized by a leucine triplet (or quadruplet) occupying different positions along a stretch of 15 amino acids. Figure 5.7 illustrates the results of these experiments.

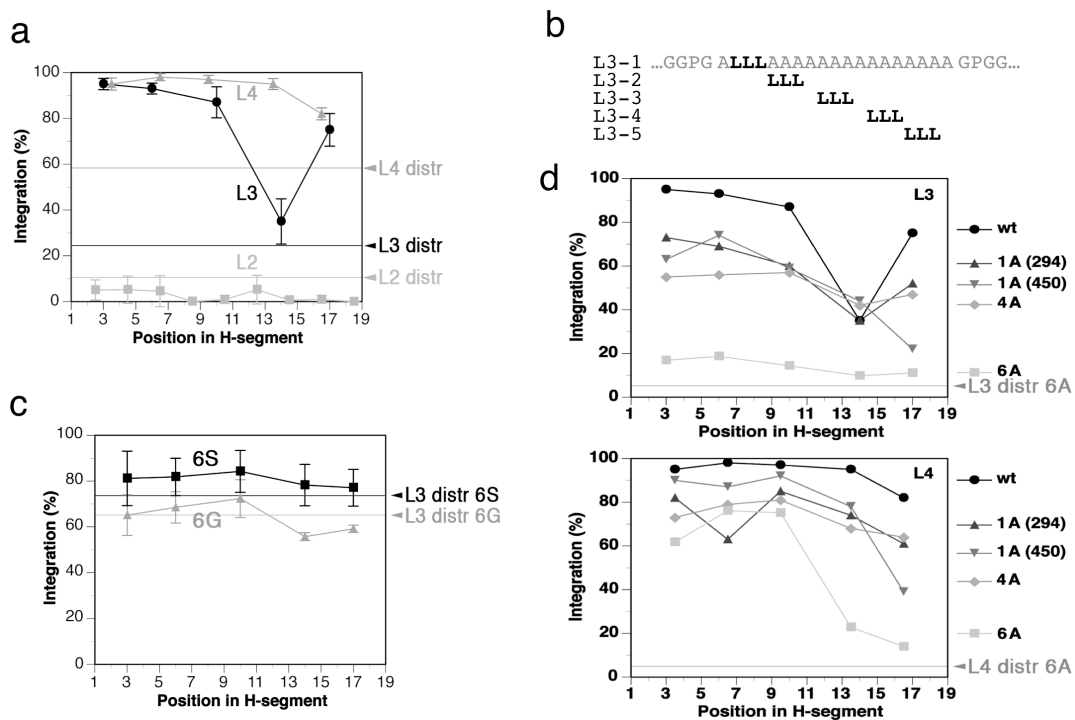


**Figure 5.7** Integration rates of various peptides by SecY wild-type and its mutants. a) Integration of L3 (with three leucine residues) and L4 (with four leucine residues) peptides by Sec61 WT b) Sequences of L3 peptides c) Integration of L3 peptides by Sec61 6S and 6G mutants d) Integration of L3 and L4 peptides by various Sec61 mutants (alanine mutants of the pore-ring residues) (64)

There is a significant reduction in membrane integration of the peptide in Sec61p wild-type when three leucines are located at the position aligned with the pore ring residues (L3-4 in Figure 5.7b). However this situation is not observed in 6G and 6S pore mutants. The drop in the membrane integration in Sec61p wild-type possibly arises from the fact that the local environment at the level of the

pore ring residues is more hydrophobic than the rest of the pore. The peptide that contains leucine amino acids at the level of the pore-ring would be more stable in the pore compared to the peptide having leucine amino acids at other positions. This could result in less membrane integration for L3-4 peptide according to thermodynamic integration model. To investigate the hydrophobicity of the pore of the Sec translocon we performed different molecular dynamics simulations with the L3-4 peptide located inside the pores of SecY (from *M. jannaschii*) and its 6A, 6G and 6S mutants. The atoms of pore-ring residues span from 0 to 10 Å in z-coordinate (see Figure 5.8). This level corresponds to the significant decrease of water density profiles, as also seen on Figure 5.9. The hydration of the pore appears to be in the following order: SecY WT <6A<6G~6S. While the pores of 6S and 6G mutants are well solvated at level of the pore-ring, those of WT and 6A mutant lack water molecules (Figure 5.9). These results explain the asymmetry observed in the experimental integration rates in WT and 6A mutant of SecY.

We also simulated 3-Leu cluster at various positions in the peptide in the pores of SecY WT, SecY 6G and SecY 6S for 5ns. From the simulations we calculated radial distribution functions (RDF) for water molecules around the last two carbon atoms (CD1 and CD2) in the side-chains of leucine residues. These RDFs provide information on the density of water molecules around the reference atoms. The comparative RDF plots for the peptides in SecY 6S and SecY 6G are given in Figure 5.10 and Figure 5.11 respectively. According to these RDFs, hydration of peptides can be categorized into two groups: well hydrated peptides (L3-1 and L3-2) and poorly hydrated peptides (L3-3, L3-4 and L3-5). The increase in hydration of L3-3, L3-4 and L3-5 in 6S and 6G mutants suggests that the mutations enhance the hydration inside the pore.

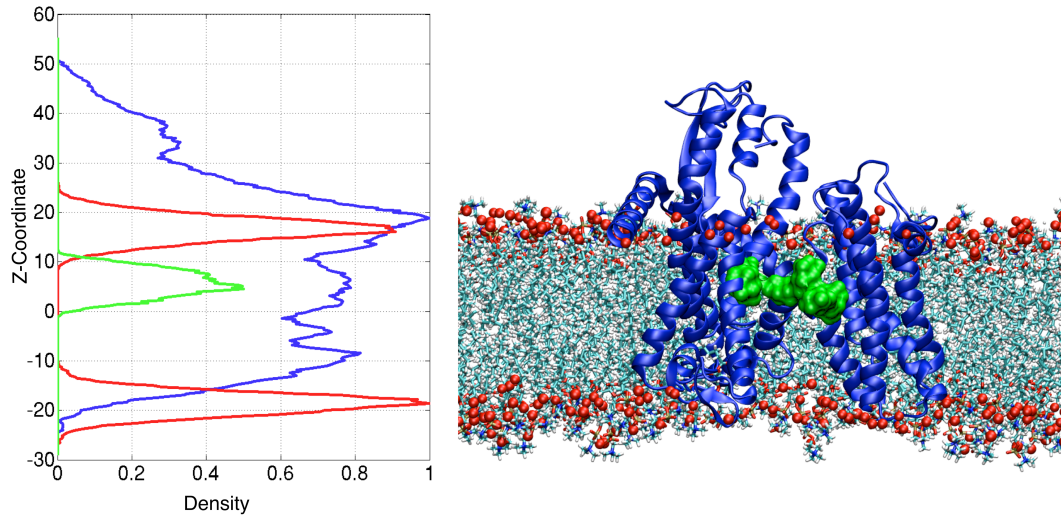


**Figure 5.8** Density profiles of lipid head groups (red), pore ring residues (green) and protein (blue)

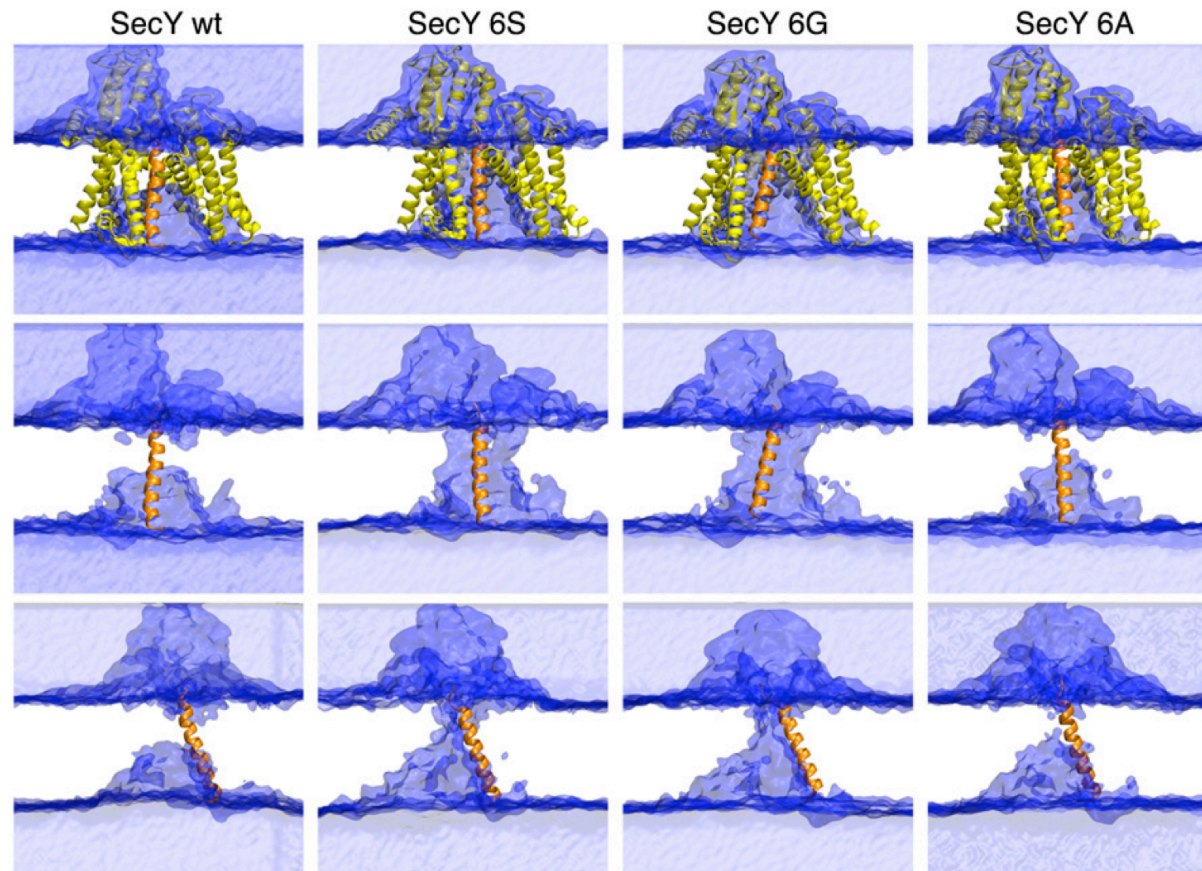


**Figure 5.9** Water density (isocontour for %30 of the simulation time) for the simulation of L3-4 peptide in SecY WT and its mutants. First row: Front view Second row: Side-view (the lateral gate is on the right-hand side of each picture).



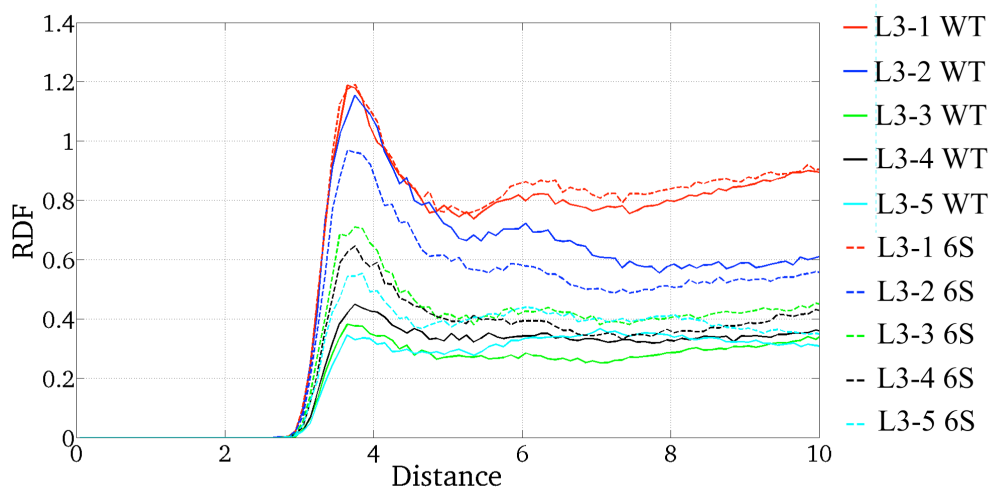


**Figure 5.10** RDF for water molecules around the last two atoms (CD1 and CD2) in the tail of leucine side-chain for 3-leu containing peptides, which are placed inside the pores of SecY WT and 6S mutant.

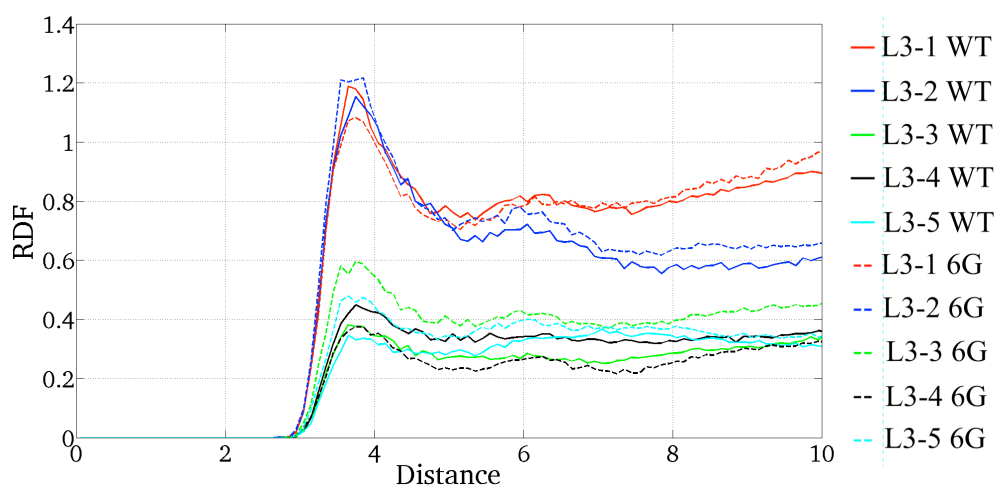


**Figure 5.11** RDF for water molecules around the last two atoms (CD1 and CD2) in the tail of leucine side-chain for 3-leu containing peptides, which are placed inside the pores of SecY WT and 6G mutant.

#### 5.4 Methods

The crystal structure of the closed state of SecY translocon from *M. jannaschii* (PDB Code: 1RHZ) was used in molecular dynamics simulations (16). Since plug deleted mutants are viable we simulated the plug deleted mutant of SecY. The placement of a peptide into the pore of the plug-deleted mutant is safer in terms of modeling than the placement of a peptide into wild-type SecY. The residues forming the plug domain (46 to 67) were replaced by a single Glycine. The protein was inserted into a bilayer composed of 389 dimyristoylphosphatidylcholine (DMPC) lipids. The protein-lipid system was solvated with 29,000 water molecules and ionized with 0.15M KCl. The system containing 142,352 atoms was placed in an orthogonal box of 116 x 125 x 96 Å<sup>3</sup> using CHARMM-GUI web server (55). The lateral gate was opened to 16 Å, enough to fit a peptide inside the pore of SecY using COLVARS module in NAMD simulation package (56). The systems for the pore-ring mutants of SecY were simply done by mutating the residues in the equilibrated system described here. Peptides were placed inside the pore after 5ns equilibration of the lateral gate opened structure. The centers of the peptides were aligned with the center of the bilayer.

All simulations were performed using NAMD simulation with the CHARMM 27 force field (57). The cut-off for van der Waals interactions was set at 12 Å with a switching function used after 10 Å. The calculation of electrostatic interactions was done using Particle-Mesh Ewald method (58). Time step for the integration is 1 fs. Short-range non-bonded interactions were calculated every 2 steps and long-range interactions every 4 steps. Simulations were performed in an isothermal-isobaric ensemble with a pressure of 1 atm and a temperature of 315K.

Free energy perturbation calculations (FEP) provide the free energy difference between the initial and final states of a system (59). FEP calculations were done by perturbing the initial state to the final step gradually with a control parameter  $\lambda$ . The parameter  $\lambda$  scales the interaction energy between the perturbed atoms and surrounding atoms. The choice of a  $\lambda$  set can vary depending on the simulation system and perturbation (60). FEP simulations were performed in forward ( $\lambda$  change from 0 to 1) and backward direction ( $\lambda$  changes from 1 to 0). The energies obtained from the forward and backward simulations were combined using the ParseFEP plugin of VMD program (61,62).

FEP calculations for perturbing L7 to L6 and L7 to L1 peptide were carried out over 25 ns with a uniformly discretized  $\lambda$  scheme with  $\Delta\lambda = 0.02$ . Each window was simulated for 0.5 ns and data for the first 0.1 ns were discarded for equilibration purpose. Perturbation calculations for growing 3-Leu cluster at various positions in peptides were also performed using the same  $\lambda$ -discretization scheme.

FEP simulations for deletion of L1 peptide in the membrane, water, SecY WT and SecY 6G were performed over 85 ns with an advanced  $\lambda$  scheme: windows for  $\lambda$  between 0 and 0.5 were simulated for 0.5 ns (0.25 ns for equilibration) with  $\Delta\lambda = 0.01$ , windows for  $\lambda$  between 0.5 and 0.9 were simulated for 0.75 ns (0.37 ns for equilibration) with  $\Delta\lambda = 0.01$ , windows for  $\lambda$  between 0.9 and 0.95 were simulated for 0.5 ns (0.25 ns for equilibration) with  $\Delta\lambda = 0.005$ , windows for  $\lambda$  between 0.95 and 0.99 were simulated for 0.75 ns (0.37 ns for equilibration) with  $\Delta\lambda = 0.002$ , and windows for  $\lambda$  between 0.99 and 1 were simulated for 1 ns (0.5 ns for equilibration) with  $\Delta\lambda = 0.001$ . FEP simulations of L1 growing were carried out using the same  $\lambda$  scheme.

In addition, radial distribution functions (RDF) were calculated using VMD program (61).

## 5.5 Conclusion

SecY/Sec61 translocon facilitates both the insertion of proteins into cell membrane or translocation of secreted proteins (1). It was initially thought that the insertion of a peptide from the translocon to the membrane was purely according to thermodynamic equilibration (37,40,42). Later this hypothesis was challenged by studies suggesting the involvement of kinetics effects in the membrane integration process (23,41,43-45,63). Additional to these views, the third one that combines both thermodynamics and non-thermodynamics effects has been proposed (46,47). Even though the exact role of the translocon in the membrane insertion process is poorly understood, it has been shown that alteration of the structure of the translocon changed the membrane integration rates (48). In this work we studied how hydrophobicity of the pore of translocon affects the membrane insertion of proteins on the basis of published and unpublished experimental results.

First, we investigated the effect of mutation of the pore-ring residues on the membrane integration process. For this purpose we chose a peptide (L1) that contains one leucine and 18 alanine residues. In the experiments performed by Junne et al., L1 peptide has been shown to insert into the membrane with Sec61 WT, but not with glycine the 6G mutant of the pore-ring residues (Sec61 6G). To understand how this mutation affects the membrane insertion we calculated absolute free energy of solvation of L1 peptide in SecY WT, SecY 6G, water and membrane. We found that L1 peptide is the most stable in membrane and the least stable in water. SecY WT and SecY 6G provide an environment of hydrophobicity in between water and membrane. L1 feels a “water-like” environment in the pore of SecY 6G and a “membrane-like” environment in the pore of SecY WT. Water densities in the pore of SecY WT and SecY 6G clearly show the difference in the hydration of the pores, which results in different hydrophobicities. Our results suggest that higher stability of L1 in the pore of SecY WT than in the pore of SecY 6G leads to higher retention time in the pore of SecY WT. This gives rise to increase in translocation rate and decrease in insertion rate. It should be noted that our results illustrate qualitative description of the distinct insertion tendency of L1 peptide mediated by SecY WT and SecY 6G. It is difficult to assess the exact insertion free energy of L1 peptide because of various reasons. The first reason is that interaction of L1 with the other helices in

the polypeptide chain was not studied here (experiments were performed with polypeptide chains composed of three helices). The second reason is the ambiguity of the influence of kinetics effect in the insertion process. According to the work of Gumbart et al. insertion kinetics can have a considerable effect in the membrane integration of marginally hydrophobic sequences (47). Despite the scarce information on the effects of kinetic factors, our calculations explain how the hydrophobicity of the pore influences the rate of membrane integration.

We also investigated on the free energy differences of membrane inserting L7 (7 Leu and 12 Ala) and non-inserting L1 peptides in various media by perturbing six leucine residues to six alanine residues. Our calculations showed that L7 and L1 peptides have almost the same stabilities in the membrane while there is a big free energy difference (9.1 kcal/mol) in water solution. This result leads to the conclusion that the interaction of a polypeptide chain with lipid molecules is not the sole determinant of the insertion. Furthermore, our calculations for the perturbations of L7 to L1 and L7 to L6 in water and membrane indicated that the solvation free energy differences of amino acids are not additive.

An interesting property of the translocon has been revealed by our collaborators from the Spiess lab. Their experiments with oligo-alanine peptides, which contain three leucine residues located at various positions, showed asymmetry in membrane integration (64). They observed that the integration rate dramatically drops when 3-leu cluster are at the level of the pore-ring residues. However experiments performed with 6S and 6G mutants of the pore rings did not show aforementioned membrane integration profile. Using computational methods we investigated why the observed asymmetry occurs. We simulated SecY WT and its pore-ring mutants with a peptide (L3-4), which contains 3-leu near the pore-ring peptide. Analysis of water densities along the pores showed that mutation of the pore-ring residues to serine and glycine residues allows stabilization of more water molecules in the pore-ring region. Furthermore, simulations of the peptides, which contain 3-leu at various positions, in SecY WT and its pore-ring mutants illustrated the difference of hydration around the pore-ring region. Our results suggest that the 3-leu cluster feels a more hydrophobic environment when they are located near the pore-ring. This situation leads to an increase in retention time for the peptides and causes less membrane integration. Consequently, experimental and computational findings indicate that the

hydrophobicity of the translocon pore has an important influence in the insertion of membrane proteins.

## 5. 6 References

1. Park E, Rapoport TA. Mechanisms of sec61/secy-mediated protein translocation across membranes. *Annu Rev Biophys* 2012;41:21-40.”
2. Higgy M, Junne T, Spiess M. Topogenesis of membrane proteins at the endoplasmic reticulum. *Biochemistry* 2004, Oct 12;43(40):12716-22.
3. Shao S, Hegde RS. Membrane protein insertion at the endoplasmic reticulum. *Annu Rev Cell Dev Biol* 2011;27:25-56.
4. Driessen AJM, Nouwen N. Protein translocation across the bacterial cytoplasmic membrane. *Annu. Rev. Biochem* 2008;77:643-67.
5. Rapoport TA. DProtein translocation across the eukaryotic endoplasmic reticulum and bacterial plasma membranes. *Nature* 2007, Nov 29;450(7170):663-9.
6. White SH, von Heijne G. How translocons select transmembrane helices. *Annu Rev Biophys* 2008;37:23-42.
7. Keenan RJ, Freymann DM, Stroud RM, Walter P. The signal recognition particle. *Annu Rev Biochem* 2001;70:755-75.
8. Grudnik P, Bange G, Sinning I. Protein targeting by the signal recognition particle. *Biol Chem* 2009, Aug;390(8):775-82.
9. Beltzer JP, Fiedler K, Fuhrer C, Geffen I, Handschin C, Wessels HP, Spiess M. Charged residues are major determinants of the transmembrane orientation of a signal-anchor sequence. *Journal of Biological Chemistry* 1991;266(2):973-8.
10. Hartmann E, Rapoport TA, Lodish HF. Predicting the orientation of eukaryotic membrane-spanning proteins. *Proc Natl Acad Sci U S A* 1989, Aug;86(15):5786-90.
11. Heijne G. The distribution of positively charged residues in bacterial inner membrane proteins correlates with the trans-membrane topology. *EMBO J* 1986, Nov;5(11):3021-7.
12. van Klompenburg W, Nilsson I, von Heijne G, de Kruijff B. Anionic phospholipids are determinants of membrane protein topology. *EMBO J* 1997, Jul 16;16(14):4261-6.
13. Cao G, Kuhn A, Dalbey RE. The translocation of negatively charged residues across the membrane is driven by the electrochemical potential: Evidence for an electrophoresis-like membrane transfer mechanism. *EMBO J* 1995, Mar 1;14(5):866-75.

14. Goder V, Junne T, Spiess M. Sec61p contributes to signal sequence orientation according to the positive-inside rule. *Mol Biol Cell* 2004;15(3):1470-8.
15. Rapoport TA, Goder V, Heinrich SU, Matlack KES. Membrane-protein integration and the role of the translocation channel. *Trends Cell Biol* 2004;14(10):568-75.
16. Van den Berg B, Clemons WM, Collinson I, Modis Y, Hartmann E, Harrison SC, Rapoport TA. X-ray structure of a protein-conducting channel. *Nature* 2004, Jan 1;427(6969):36-44.
17. Li W, Schulman S, Boyd D, Erlandson K, Beckwith J, Rapoport TA. The plug domain of the secy protein stabilizes the closed state of the translocation channel and maintains a membrane seal. *Mol Cell* 2007, May 25;26(4):511-21.
18. Junne T, Schwede T, Goder V, Spiess M. The plug domain of yeast sec61p is important for efficient protein translocation, but is not essential for cell viability. *Mol Biol Cell* 2006;17(9):4063-8.
19. Maillard AP, Lalani S, Silva F, Belin D, Duong F. Deregulation of the secyeg translocation channel upon removal of the plug domain. *J Biol Chem* 2007, Jan 12;282(2):1281-7.
20. Saparov SM, Erlandson K, Cannon K, Schaletzky J, Schulman S, Rapoport TA, Pohl P. Determining the conductance of the secy protein translocation channel for small molecules. *Mol Cell* 2007, May 25;26(4):501-9.
21. Gumbart J, Schulten K. The roles of pore ring and plug in the secy protein-conducting channel. *J Gen Physiol* 2008, Dec;132(6):709-19.
22. van der Wolk JP, Fekkes P, Boorsma A, Huie JL, Silhavy TJ, Driessen AJ. PrlA4 prevents the rejection of signal sequence defective preproteins by stabilizing the secA-secy interaction during the initiation of translocation. *EMBO J* 1998, Jul 1;17(13):3631-9.
23. Zhang B, Miller TF. Hydrophobically stabilized open state for the lateral gate of the sec translocon. *Proc Natl Acad Sci U S A* 2010, Mar 23;107(12):5399-404.
24. du Plessis DJ, Berrelkamp G, Nouwen N, Driessen AJ. The lateral gate of secyeg opens during protein translocation. *J Biol Chem* 2009, Jun 5;284(23):15805-14.
25. Zimmer J, Nam Y, Rapoport TA. Structure of a complex of the atpase secA and the protein-translocation channel. *Nature* 2008;455(7215):936-43.



26. Tsukazaki T, Mori H, Fukai S, Ishitani R, Mori T, Dohmae N, et al. Conformational transition of sec machinery inferred from bacterial secYE structures. *Nature* 2008, Oct 16;455(7215):988-91.
27. Gumbart J, Trabuco LG, Schreiner E, Villa E, Schulten K. Regulation of the protein-conducting channel by a bound ribosome. *Structure* 2009, Nov 11;17(11):1453-64.
28. Becker T, Bhushan S, Jarasch A, Armache JP, Funes S, Jossinet F, et al. Structure of monomeric yeast and mammalian sec61 complexes interacting with the translating ribosome. *Science* 2009, Dec 4;326(5958):1369-73.
29. Frauenfeld J, Gumbart J, Sluis EO, Funes S, Gartmann M, Beatrix B, et al. Cryo-EM structure of the ribosome-secYE complex in the membrane environment. *Nat Struct Mol Biol* 2011, May;18(5):614-21.
30. Egea PF, Stroud RM. Lateral opening of a translocon upon entry of protein suggests the mechanism of insertion into membranes. *Proc Natl Acad Sci U S A* 2010, Oct 5;107(40):17182-7.
31. Hizlan D, Robson A, Whitehouse S, Gold VA, Vonck J, Mills D, et al. Structure of the secYE complex unlocked by a preprotein mimic. *Cell Rep* 2012, Jan 26;1(1):21-8.
32. MacCallum JL, Tieleman DP. Hydrophobicity scales: A thermodynamic looking glass into lipid-protein interactions. *Trends Biochem Sci* 2011, Dec;36(12):653-62.
33. Radzicka A, Wolfenden R. Comparing the polarities of the amino acids: Side-chain distribution coefficients between the vapor phase, cyclohexane, 1-octanol, and neutral aqueous solution. *Biochemistry* 1988;27(5):1664-70.
34. MacCallum JL, Bennett WF, Tieleman DP. Distribution of amino acids in a lipid bilayer from computer simulations. *Biophys J* 2008, May 1;94(9):3393-404.
35. Wimley WC, Creamer TP, White SH. Solvation energies of amino acid side chains and backbone in a family of host-guest pentapeptides. *Biochemistry* 1996;35(16):5109-24.
36. Wimley WC, White SH. Experimentally determined hydrophobicity scale for proteins at membrane interfaces. *Nat Struct Biol* 1996;3(10):842-8.
37. Hessa T, Kim H, Bihlmaier K, Lundin C, Boekel J, Andersson H, et al. Recognition of transmembrane helices by the endoplasmic reticulum translocon. *Nature* 2005, Jan 27;433(7024):377-81.

38. Moon CP, Fleming KG. Side-chain hydrophobicity scale derived from transmembrane protein folding into lipid bilayers. *Proc Natl Acad Sci U S A* 2011, Jun 21;108(25):10174-7.
39. MacCallum JL, Tieleman DP. Hydrophobicity scales: A thermodynamic looking glass into lipid-protein interactions. *Trends Biochem Sci* 2011, Dec;36(12):653-62.
40. Hessa T, Meindl-Beinker NM, Bernsel A, Kim H, Sato Y, Lerch-Bader M, et al. Molecular code for transmembrane-helix recognition by the sec61 translocon. *Nature* 2007, Dec 13;450(7172):1026-30.
41. Goder V, Crottet P, Spiess M. In vivo kinetics of protein targeting to the endoplasmic reticulum determined by site-specific phosphorylation. *EMBO J* 2000, Dec 15;19(24):6704-12.
42. Hessa T, Monné M, von Heijne G. Stop-transfer efficiency of marginally hydrophobic segments depends on the length of the carboxy-terminal tail. *EMBO Rep* 2003, Feb;4(2):178-83.
43. Cheng Z, Gilmore R. Slow translocon gating causes cytosolic exposure of transmembrane and luminal domains during membrane protein integration. *Nat Struct Mol Biol* 2006, Oct;13(10):930-6.
44. Trueman SF, Mandon EC, Gilmore R. Translocation channel gating kinetics balances protein translocation efficiency with signal sequence recognition fidelity. *Mol Biol Cell* 2011, Sep;22(17):2983-93.
45. Rychkova A, Warshel A. Exploring the nature of the translocon-assisted protein insertion. *Proc Natl Acad Sci U S A* 2013, Jan 8;110(2):495-500.
46. Zhang B, Miller TF. Long-timescale dynamics and regulation of sec-facilitated protein translocation. *Cell Rep* 2012, Oct 25;2(4):927-37.
47. Gumbart J, Teo I, Roux B, Schulten K. Reconciling the roles of kinetic and thermodynamic factors in membrane-protein insertion. *J Am Chem Soc* 2013, Jan 8.
48. Junne T, Kocik L, Spiess M. The hydrophobic core of the sec61 translocon defines the hydrophobicity threshold for membrane integration. *Mol Biol Cell* 2010, May 15;21(10):1662-70.
49. Gumbart J, Chipot C, Schulten K. Free-energy cost for translocon-assisted insertion of membrane proteins. *Proc Natl Acad Sci U S A* 2011, Mar 1;108(9):3596-601.

50. Lu J, Deutsch C. Folding zones inside the ribosomal exit tunnel. *Nat Struct Mol Biol* 2005, Dec;12(12):1123-9.
51. Bhushan S, Meyer H, Starosta AL, Becker T, Mielke T, Berninghausen O, et al. Structural basis for translational stalling by human cytomegalovirus and fungal arginine attenuator peptide. *Mol Cell* 2010, Oct 8;40(1):138-46.
52. Bhushan S, Gartmann M, Halic M, Armache JP, Jarasch A, Mielke T, et al. Alpha-Helical nascent polypeptide chains visualized within distinct regions of the ribosomal exit tunnel. *Nat Struct Mol Biol* 2010, Mar;17(3):313-7.
53. Gumbart J, Chipot C, Schulten K. Free energy of nascent-chain folding in the translocon. *J Am Chem Soc* 2011, May 18;133(19):7602-7.
54. Wolfenden R, Andersson L, Cullis PM, Southgate CC. Affinities of amino acid side chains for solvent water. *Biochemistry* 1981, Feb 17;20(4):849-55.
55. Jo S, Kim T, Iyer VG, Im W. CHARMM-GUI: A web-based graphical user interface for CHARMM. *J Comput Chem* 2008, Aug;29(11):1859-65.
56. Phillips JC, Braun R, Wang W, Gumbart J, Tajkhorshid E, Villa E, et al. Scalable molecular dynamics with NAMD. *J Comput Chem* 2005, Dec;26(16):1781-802.
57. MacKerell Jr AD, Bashford D, Bellott M, Dunbrack Jr RL, Evanseck JD, Field MJ, et al. All-atom empirical potential for molecular modeling and dynamics studies of proteins. *The Journal of Physical Chemistry B* 1998;102(18):3586-616.
58. Essmann U, Perera L, Berkowitz ML, Darden T, Lee H, Pedersen LG. A smooth particle mesh ewald method. *J Chem Phys* 1995;103:8577.
59. Zwanzig RW. High-Temperature equation of state by a perturbation method. I. Nonpolar gases. *J Chem Phys* 1954;22:1420.
60. Pohorille A, Jarzynski C, Chipot C. Good practices in free-energy calculations. *The Journal of Physical Chemistry B* 2010;114(32):10235-53.
61. Phillips JC, Braun R, Wang W, Gumbart J, Tajkhorshid E, Villa E, Chipot C. *Chemistry*, 26: 1781-1802, 2005. Humphrey, W., Dalke, A. And schulten, K., "VMD-Visual molecular dynamics", *J. Molec. Graphics*, 1996, vol. 14, pp. 33-38. &Stephan frickenhaus, AWI, 2007, som\\_pak-3.1 modified for dihedral periodicity, vmd-scripts trajsort/mkpic in tcl. *Chemistry* 2005;26:1781-802.
62. Liu P, Dehez F, Cai W, Chipot CJ. A toolkit for the analysis of free-energy perturbation calculations. *J Chem Theory Comput* 2012, Jul 18;8:2606–2616.

63. Goder V, Spiess M. Molecular mechanism of signal sequence orientation in the endoplasmic reticulum. *EMBO J* 2003, Jul 15;22(14):3645-53.

64. Demirci E, Junne T, Baday S, Bernèche S, Spiess M. Functional asymmetry within the sec61p translocon. *Proc Natl Acad Sci U S A* 2013, Nov 19;110(47):18856-6

*Personal Information*

---

Nationality	Turkish
Date of Birth	02.02.1984
Gender	Male
Mobile Phone	+41789066256
E-Mail	badaysefer@yahoo.com

*Education*

---

01/2009-03/2013 **PhD, Biophysics**

Biozentrum, University of Basel, Switzerland

Thesis title: Computational investigation of function of membrane proteins: Amt/Rh Ammonium transporters and SecY Translocon

09/2006-11/2008 **MS, Computational Science and Engineering**

Koç University, Istanbul, Turkey

Thesis title: Determination of Pair Potentials for Protein Folding

09/2001-06/2006 **BS, Chemical Engineering**

Bogazici University, Istanbul, Turkey

## *Work Experience*

---

04/2013-03/2014	Postdoctoral Researcher, University of Basel, Switzerland
01/2009-03/2013	Research Assistant, University of Basel, Switzerland
09/2006-11/2008	Research Assistant, Koc University, Istanbul, Turkey
07/2004-09/2004	Internship at the R&D Department of Print Kimya (Textile Printing Inks), Istanbul, Turkey

## *PUBLICATIONS*

---

1. Functional asymmetry within the Sec61p Translocon  
E. Demirci, T. Junne, **S. Baday**, S. Bernèche, M. Spiess, PNAS (2013), 110, 18856-18861
2. Different hydration schemes of the pore of AmtB and RhCG determine their transport mechanisms  
**S. Baday**, S. Wang, G. Lamoureux, S. Bernèche, Biochemistry (2013), 52, 7091–7098
3. Ammonium Transporters achieve charge transfer by fragmenting their substrate  
S. Wang, E.A. Orabi, **S. Baday**, S. Bernèche, G. Lamoureux, JACS (2012), 134, 10419-10427
4. Transport Mechanisms in the Ammonium Transporter Family  
G. Lamoureux, A. Javelle, **S. Baday**, S. Wang, S. Bernèche  
Transfusion clinique et biologique 17 (2010) 168–175
5. Determination of pair-wise inter-residue interaction forces from folding pathways and their implementation in coarse-grained folding prediction  
**S. Baday**, B. Erman, Y. Arkun Phys. Chem. Chem. Phys., (2009), 11, 1949 – 1961
6. Optimum folding pathways for growing protein chains  
S. Senturk, **S. Baday**, Y. Arkun, B. Erman, Physical Biology 4 (2007) 305–316